CONFERENCE PROCEEDINGS NSSY 2023

Here we present the Proceedings of fourth edition international edition of Nanoscience Summer School Yachay, (NSSY2023), held from the 23rd of April until the 29th of April 2023 at Puerto Ayora, Galapagos Islands, Ecuador.

The NSSY 2023 had plenary sessions from the most eminent scientist, invited talks from leading researchers in the field, and contributed talks chosen from the best-submitted abstracts.

We will also feature a two-day poster session

In this international edition of NSSY2023, there was the participation of 90 delegates between speakers, keynotes, professor, researches and students. Talks from latest work in different topics of nanoscience and nanotechnology, theoretical and experimental works and their applications.

Dr Gema Gonzalez
Dean School Physical Sciences
and Nanotechnology, Yachay Tech University

NSSY2023
Conference Chair

Editor In Chief
Acta Microsocopica

Nanoscience Summer School 2023 @Yachay Tech International Fourth edition

April 23rd to 29th, 2023

SCHOOL OF PHYSICAL SCIENCES AND NANOTECHNOLOGY

San Miguel de Urcuquí,
Hacienda San José s/n y Proyecto Yachay
Telephone: +593 62999500

Organizing Committee

Gema González
Sarah Briceño
Julio Chacón
Melany Aguilar Ramirez
Charlotte Berrezueta Palacios
Alexis Garzón

Support Committee

Evelyn Cifuentes
Daniela Serrano
Daniela Arellano
Angie Dávila

Scientific Committee

Duncan John Mowbray
Carlos Reinoso
Henry Pinto
Antonio Díaz
Johnny Chimborazo
David Andrade

Advisory Committee

Norman Wray
Lucia Norris

MONDAY

Characterization of Nanostructures

TUESDAY

Molecular Modelling of Nanostructures

WEDNESDAY

2D Nanomaterials and Heterostructures

THURSDAY

Synthesis of Nanostructures

FRIDAY

Theory and Simulations in Nanoscience

TUESDAY

Poster Session 1

THURSDAY

Poster Session 2

Acta Microscopica Vol. 32, Supp. 1, 2023
Abstract Book NSSY 2023- Galapagos 23 -29 April, 2023

Conference

Acta Microscopica Vol. 32, Supp. 1, 2023
Abstract Book NSSY 2023- Galapagos 23 -29 April, 2023

MONDAY

Characterization of Nanostructures

Acta Microscopica Vol. 32, Supp. 1, 2023
Abstract Book NSSY 2023- Galapagos 23 -29 April, 2023

RAMAN SPECTROSCOPY: A TUTORIAL

Vincent Meunier (1)

(1) Engineering Science and Mechanics Department, The University of Pennsylvania, State College, PA, USA
vincent.meunier@psu.edu

Raman spectroscopy is a spectroscopic technique used to measure the vibrational modes of materials. Raman spectroscopy is a popular technique used in chemistry and material science and has proven one of the key techniques in the development of nanoscience and nanotechnology. This technique relies on inelastic scattering of photons. The photons (e.g., monochromatic light from a laser) interact with the electronic properties of a material and, during the process, can excite phonon (i.e., vibrational) modes. Due to energy conservation requirements, the scattered light's energy is shifted by an energy that corresponds to the existing phonon mode, and which can then be determined. For this reason, Raman spectroscopy can be used to examine the intrinsic fingerprints of materials and molecules. As a non-destructive and fast technique, Raman has repeatedly proven effective for the quantitative determination of their properties. The interpretation of many experimental features requires a dedicated modeling effort based on first-principles methodologies. Fortunately, at the same time as experimental characterization and sample preparation techniques have evolved to new heights, theoretical schemes are now combined with unprecedented computational resources to provide tools akin to a *virtual microscope* to enable the translation of experimental data into a fundamental understanding of intrinsic properties of the investigated samples.

Here, I will summarize the fundamental features of Raman spectroscopy, focusing on nanomaterials as test subjects. Using a semi-classical framework, I will provide a pedagogical step-by-step introduction to Raman spectroscopy with the objective of teaching students how to read Raman spectra and find ways to interpret them. I will introduce concepts such as Rayleigh, Stokes, and anti-Stokes mechanism and show the importance of light polarization in the determination of the Raman spectrum. I will explain what Raman practitioners mean about the concept of "Raman active modes". Finally, if time permits, I will also introduce the outline of a full quantum mechanical treatment of resonant Raman spectroscopy. In the second part of my talk, I will describe how Raman can be used to obtain a determination of the structural details of defective [1] and finite-size nanoribbons [2]. Furthermore, I will discuss the importance of low-frequency modes in the study of layer-layer interactions in TMDs and phosphorene, how relative twisting angles can be determined by monitoring relative shifts in Raman active mode in $MoSe_2$, and how Raman can be employed to understand in-plane anisotropy in phosphorene. Finally, I will show how defect concentration (notably, S vacancy density) can be determined by the sole knowledge of the shift in major vibration modes of MoS_2 subjected to electron irradiation [3].

REFERENCES

[1] O Gröning, et al, *Engineering of robust topological quantum phases in graphene nanoribbons,* Nature 560 (7717), 209-213 (2018)
[2] J Overbeck et al, *A universal length-dependent vibrational mode in graphene nanoribbons,* ACS nano 13 (11), 13083-13091 (2019)
[3] W. Parkin et al. *Raman shifts and in situ TEM electrical degradation of electron-irradiated monolayer MoS_2,* submitted (2016)

ACKNOWLEDGMENTS

Vincent Meunier thanks support from the Focus Center at Rensselaer Polytechnic Institute, a NYS Department of Economic Development award (No. A21-0125-002 and RPI designation A50634.2326) and from the Pennsylvania State University.

FIGURES

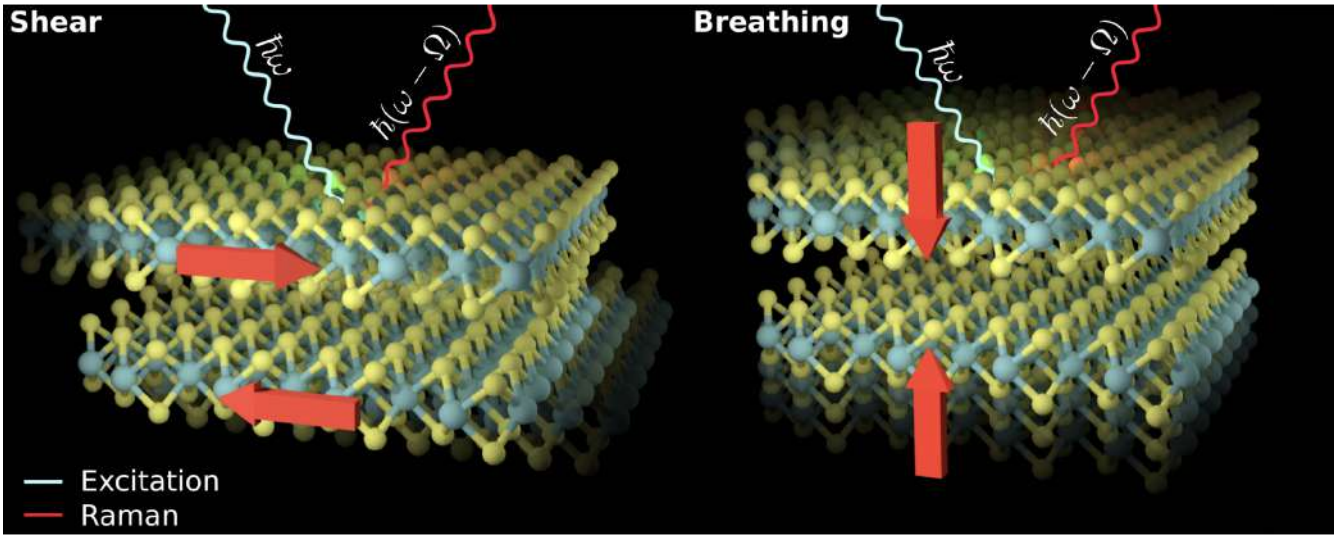

Figure 1. Schematic representation of the interlayer Raman processes taking place in bilayered MoS_2 material.

Acta Microscopica Vol. 32, Supp. 1, 2023
Abstract Book NSSY 2023- Galapagos 23 -29 April, 2023

TiO_2-MODIFIED BORON-DOPED DIAMOND PHOTOANODES FOR EFFICIENT PHARMACEUTICAL, PESTICIDE AND MICROPLASTICS PHOTOELECTROCATALYTIC DEGRADATION

Patricio J. Espinoza-Montero[1], Paulina Alulema-Pullupaxi[1,2], Carol Sigcha-Pallo[1,2], Wendy Quilumbaquin[1], G. Xavier Castillo-Cabrera[1]

Pontificia Universidad Católica del Ecuador, Escuela de Ciencias Químicas, Quito 170525, Ecuador. pespinoza646@puce.edu.ec. (2) Escuela Politécnica Nacional, Departamento de Ingeniería Civil y Ambiental, Quito-Ecuador
pespinoza646@puce.edu.ec

Pollution of natural effluents caused by population growth, industrial development and the expansion of the agricultural frontier is a serious problem that has received scarce attention. Recalcitrant and contaminants of emerging concern (CECs) (i.e. pharmaceuticals, agrochemicals, microplastics, detergents, dyes, phenolic derivatives, etc.) are both an environmental and a health problem, mainly due to its toxicity and possible hazardous effects on living organisms, including humans. Conventional wastewater treatments have not been able to efficiently remove contaminants from water; nevertheless, electrochemical advanced oxidation processes (EAOPs) can address this environmental issue. One of the most popular EAOPs technologies today is photoelectrocatalysis (PEC). The PEC consists of: i) light absorption on the photocatalyst-semiconductor thin film supported on a conductive substrate (photoelectrode) (light energy > photocatalyst band-gap), generating electron-hole (e^-–h^+) charge carriers; ii) extraction of the electrons from the conduction band (CB) of the photoanode to the external circuit, applying an external bias potential; iii) the occurrence of the surface redox reactions (h^+ generate $^{\bullet}OH$), Figure 1. The hydroxyl radical ($^{\bullet}OH$) is the second strongest oxidant in nature after fluorine, responsible for the degradation/mineralization of organic pollutants in aqueous media. [1]. In this regard, the construction of boron-doped diamond photoanodes modified with titanium dioxide (BDD/TiO_2) is presented by two methods for the fabrication of thin-film photoelectrodes, one by in situ synthesis of the photocatalyst (sol-gel spin coating) and the other by surface modification of the commercial photocatalyst (electrophoresis). Their surface, electrochemical and photoelectrochemical characterisation is presented. In addition, the results of the application of BDD/TiO_2 photoanodes in the efficient photoelectrocatalytic degradation of glyphosate [2] and diclofenac [3], as well as the deterioration/fragmentation of microparticulated high-density polyethylene (HDPE) in synthetic water samples are shown. An increase in the degradation rate of both paracetamol and diclofenac by FEC is highlighted as a result, compared to the results obtained by electrochemical advanced oxidation (EAO). In the case of the treatment of microplastics by FEC, a greater effectiveness is achieved in the deterioration of HDPE microspheres compared to AEO. In this way, it is evidenced that the modification of the BDD electrode with TiO_2 favors the injection of charge carriers, and in this fashion the transfer at the photoelectrode-solution interface is improved. In addition, it is demonstrated that the electrodes obtained by both techniques of thin film deposition present a high stability during the degradation cycles to which they were subjected.

REFERENCES

[1] G. X. Castillo-Cabrera, P. J. Espinoza-Montero, and P. Alulema-Pullupaxi, “Bismuth Oxyhalide-Based Materials (BiOX : X = Cl , Br , I) and Their Application in Photoelectrocatalytic Degradation of Organic Pollutants in Water : A Review,” *Front. Chem.*, vol. 10, pp. 1–19, 2022.
[2] P. Alulema-Pullupaxi *et al.*, “Photoelectrocatalytic degradation of glyphosate on titanium dioxide synthesized by sol-gel/spin-coating on boron doped diamond (TiO_2/BDD) as a photoanode,” *Chemosphere*, vol. 278, 2021.
[3] C. Sigcha-Pallo *et al.*, “Photoelectrocatalytic degradation of diclofenac with a boron-doped diamond electrode modified with titanium dioxide as a photoanode,” *Environ. Res.*, vol. 212, p. 113362, Sep. 2022.

ACKNOWLEDGMENTS

The authors are grateful to the Pontifical Catholic University of Ecuador for financial support for the project "Preparation of boron-doped diamond (BDD) photoelectrodes modified with bismuth semiconductors and their application in photoelectrocatalysis". Code: 030-UIO-2023.

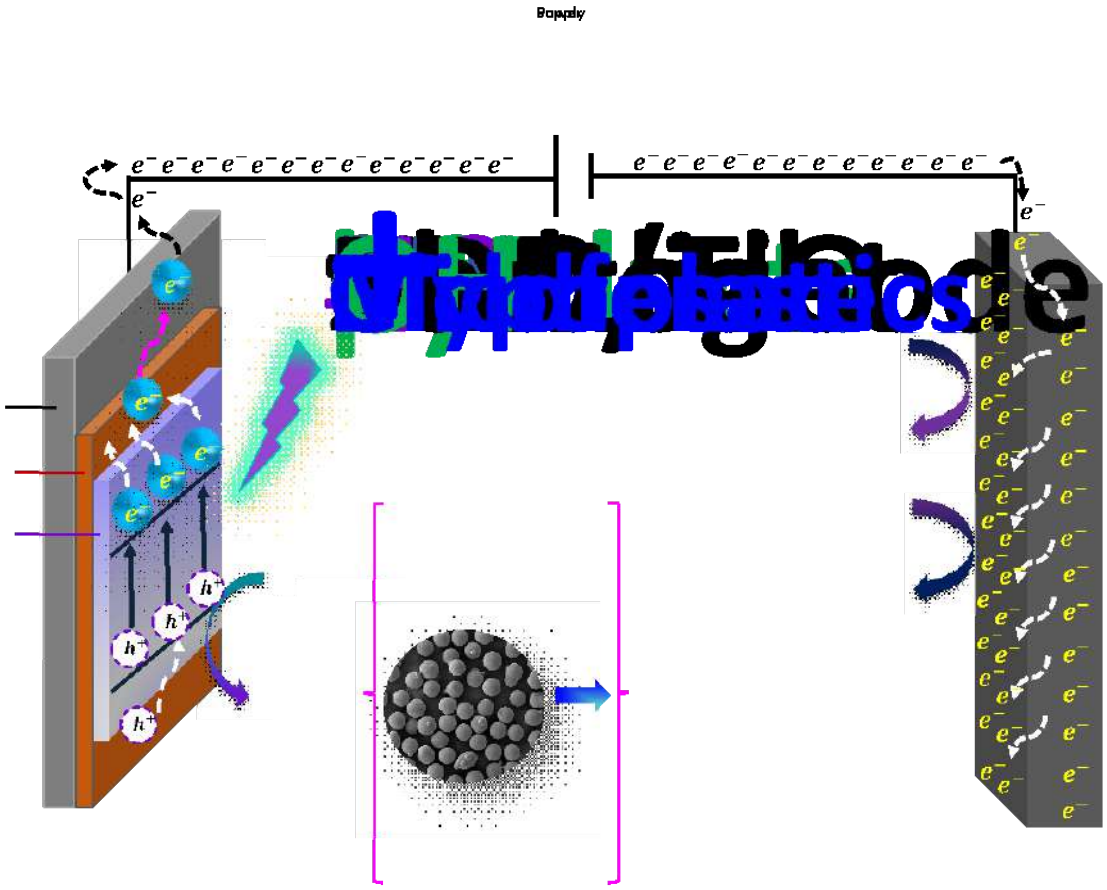

Figure 1. Photoelectrocatalytic mechanism based on a boron-doped diamond photoanode modified with titanium dioxide (BDD/TiO_2).

NEAR-ATMOSPHERIC PRESSURE X-RAY PHOTOELECTRON SPECTROSCOPY APPLIED TO STUDY THE SENSING DETECTION MECHANISM OF TRANSITION METAL DICHALCOGENIDES

Aanchal Alagh (1), Fatima Ezahra Annanouch (1), Eduard Llobet (1) and Carla Bittencourt (2).

(1) Department of Electrical Electronic Engineering and Automation, Universitat Rovira i Virgili, Tarragona, Spain.
(2)Plasma-Surface Interaction Chemistry, Chemistry Department, University of Mons, Mons, Belgium.
carla.bittencourt@umons.ac.be

The interface between gasses and solids governs many processes, such as energy generation and heterogeneous catalysis, that are key for the development of new technologies. Many surface-sensitive spectroscopies and microscopies can be used to study vapor/solid interfaces; among them, X-ray photoelectron spectroscopy (XPS) is one of the most versatile. It is highly surface sensitive due to the photoelectrons' short mean free path, providing quantitative information about the surface's elemental composition and chemical specificity (e.g., oxidation state).

Despite the usefulness of XPS measurements in ultra-high vacuum (UHV) for determining the chemical composition of active layers, UHV studies may not capture changes in surface chemical composition in the presence of an analyte gas. Such information is, however, vital for understanding how a device based on gas-surface interaction works. Since photoelectrons are strongly scattered by gas molecules, the use of XPS at elevated pressures was ruled out until very recently. For instance, the inelastic mean free path of an electron with 100 eV kinetic energy with 1mbar water vapor is about 1mm, much shorter than the typical working distance between the sample surface and the entrance to the electrostatic lens of an electron analyzer, which is a few centimeters.

However, advances in vacuum technology have led to the development of a variety of photoelectron spectrometers using differential vacuum pumping that can now operate at up to approximately 130 mbar [1,2]. This technique is known as near ambient pressure (NAP) or high pressure (HP) XPS to distinguish it from traditional vacuum-based XPS [3]. The unique combination of surface sensitivity, element specificity, and elevated pressure operation makes NAP-XPS ideal for an ‘in-situ/in-operando’ investigation of the chemical composition and mechanisms of surface processes central to the operation of gas sensing.

Research on graphene has been based on its use as a replacement for silicon in electronics. However, it is now unlikely to happen. Instead, novel applications have emerged. Bearing in mind the history of the development of graphene research, for nanostructured transition metal dichalcogenides to have an impact, new technologies must be based on their unique properties and not on the possibility of replacing materials used in present technologies.

Continuous and reliable detection of different gasses is essential in industrial process monitoring, vehicle emission control, indoor and outdoor air quality safety, and environmental protection. Traditionally, metal oxide semiconductors have been commonly utilized in these applications as sensing materials. While these sensors and their arrays offer fair discrimination and even quantification of analytes, their operation is only possible at high temperatures, which requires considerable power sourcing. Nowadays, with the spread of internet-of-things and wireless networks that involve complex sensing systems with a small but large number of devices, power consumption becomes a significant factor. Novel materials that would allow for the low-temperature operation could alleviate power-related challenges and contribute to better and more robust

sensor networks. In this context, 2D layered transition metal dichalcogenides (TMDs) have recently been found very attractive for chemo-resistive sensors. Recent studies of WS2 and MoS2 as gas sensor active layers indicate substantial response at low operating temperatures with particular selectivity to certain gasses such as NO2, H2S, and NH3. The lowered operation temperature of transition metal chalcogenide-based sensors, in reference to metal oxides, is due to their typically lower bandgap and better conductivity. Furthermore, similarly to semiconducting metal oxide sensors, the gas selectivity of TMDs is often associated with their surface's affinity for adsorbing different analytes and related surface charging/polarization effects. In addition, it has been identified that apart from surface charging/polarization, reversible doping of the chalcogenide lattice with heteroatoms can significantly contribute to sensing. Although very valuable, most of the reports are based on extra-situ measurements. Although many works discuss sensing mechanisms of TMDs materials under dry conditions or in the presence of ambient moisture, these are speculative since few operando spectroscopic studies are available for elucidating these.

We will report on the use of NAP-XPS to study the sensing of WS2 and Cu2O-WS2 nanostructured films. The films were prepared by CVD. The survey and high-resolution XPS spectra of W, O, and C, and S were measured before and during exposure at different (gas pressure conditions) at the two operating temperatures (RT and 150oC). The samples were heated from underneath using an IR-laser. The sample´s resistance was measured when collecting the XPS data (in operando analysis). These experiments allow correlating the changes at the sample surface with the sensing properties of WS2 and Cu-WS2 nanomaterials: which factors (oxygen species, tungsten oxidation state, adsorbed intermediate species) most influence the sensing properties. In-situ analysis of the interaction of CO with the WS2:Cu2O surface: the spectrum recorded during interaction suggests a change in the surface potential supported by the observation of a simultaneous change in the conductivity of the sample (in operando). The relative intensity of the two components in the O 1s peak changed due to the CO interaction indicating the participation of the tungsten oxide in the WS2:Cu2O sensing at low temperatures.

To better understand the effect of materials morphology and metal oxide loading on the gas sensing mechanism as well as improve sensing properties, we characterize the surface composition and electronic structure of the nanomaterials under real conditions. That is at the sensor operating temperature, during the exposure to oxygen, and then during the exposure to CO and H2. The role of having or lacking adsorbed water at the surface by exposing WS2 to moisture was evaluated. By identifying the intermediate species adsorbed together with the measurement of electrical conductance, we expect to unveil the morphology-performance correlation in the detection of CO and H2. NAP-XPS is a unique technology capable of conducting this type of analysis under realistic operating conditions.

REFERENCES

[1] Ueda K. et al. ACS Catal. (2018) (8) (12) (11663).
[2] Starr D.E. et al. Chem. Soc. Rev. (2013) (42) (5833).
[3] Junker B. et al. J. Phys. D: Appl. Phys. (2022) (55) (064002).

ACKNOWLEDGMENTS

C. B. is a Research Associate of the National Funds for Scientific Research (FRS-FNRS, Belgium; E. L. is supported by the Catalan Institute for advanced studies (ICREA)) via the 2018 Edition of the ICREA.

CONTROLLING DOPING PROFILES OF SILICON NANOWIRES FOR QUANTUM COMPUTING AND PHOTOVOLTAICS USING MICRO-RAMAN SPECTROSCOPY

Jorge Serrano (1), Vanessa Giselle Hinojosa Chasiquiza (1), Irene Mediavilla Martínez (1), Juan Jiménez (1), David Bricio (2), Francesc Pérez-Murano (2), Jordi Llobet (2), Jordi Antonja (3), Joan Bausells (2), Franck Bassani (4), Bassem Salem (4), Thierry Baron (4).

(1) Grupo OPTRONLAB, Dep. de Física de Materia Condensada, Cristalografía y Mineralogía, Universidad de Valladolid, Edificio LUCIA, Paseo de Belén 19, 47011 Valladolid, Spain. (2) Instituto de Microelectrónica de Barcelona IMB-CNM, CSIC, 08193 Bellaterra, Barcelona, Spain. (3) CELLS-ALBA Synchrotron, Carrer de la Llum 2-26, Cerdanyola del Vallès 08290, Spain. (4) LTM-CNRS, CEA-LETI, 17 rue des Martyrs, 38054 Grenoble Cedex, France.
jorge.serrano@uva.es

Silicon technology has been the cornerstone for the advance of the current age of information since the inception of the first transistor, due to an exponential development of microelectronics and chip miniaturization. Based on this success, some of the emerging technologies in photovoltaics and quantum computing are being developed using silicon nanowires as a fundamental building block. In the case of photovoltaics, p-n axial and core-shell junctions in Si nanowires allow the integration of silicon technology with other materials and thus a potential larger solar cell efficiency [1]. In quantum computing, silicon nanowires serve as one of the semiconducting platforms for qubit development by controlling the electron spin levels using a tailored selected doping and voltage in gates that split the nanowire into different quantum dots [2]. In both scenarios it is of paramount importance to control several key parameters, among them the dopant concentration in the nanowire, the stress, and the concentration of defects. They can all affect the operation of the corresponding device and result in critical failure or lack of reliability. Accessing these parameters with nanoscale resolution has been a challenge for spectroscopic techniques due to the diffraction limit of currently widespread optical spectroscopy. We present here a characterization using micro-Raman imaging and tip-enhanced Raman spectroscopy (TERS) that shows the potential of these techniques to determine the doping profile of silicon nanowires in both p-n junctions and silicon nanostructures for qubits, and to distinguish doping effects from others such as the presence of strain, crystal grains, and defects. High dopant concentrations lead to Fano asymmetric line shape of the Raman spectrum of silicon with an asymmetry parameter proportional to the dopant concentration and character – p- or n-type doping [3]. Confinement of the electric field due to the nanoscale diameter of the nanowires results in an enhancement of the Raman signal that yields higher resolution than that expected without this antenna effect. This enhancement allows us to employ micro-Raman spectroscopy successfully to distinguish several of the above mentioned effects in nanostructures. In the case of p-n axial junctions in silicon nanowires, we observe an asymmetry with higher spectral weight in the low and high energy side for p-type and n-type doping, respectively, being the effect more pronounced in the case of p-type doping. This effect is more significant for doping concentrations above 10^{17} cm^{-3}. In the case of nanostructured silicon for qubits we observe residual strain and crystallite grain boundaries close to the nanowire, tentatively attributed to the presence of We analyze the Raman spectra employing several asymmetric functions and compare the results obtained in nanowires with those reported in the literature and achieved in bulk silicon as a function of doping. Finally, we employ TERS to reach nanoscale spatial resolution and compare the accuracy and limitations of micro-Raman in the determination of the doping profile.

REFERENCES

[1] Li, G., Kwok, HS. (2018). *Silicon Nanowire Solar Cells*. In: Ikhmayies, S. (eds) Advances in Silicon Solar Cells. Springer, Cham, pp. 269.
[2] Maurand R. et al. *Nat. Commun.* (2016) (7) (13575).
[3] U. Fano, *Physical Review* (1961) (124) (1866).

ACKNOWLEDGMENTS

J. Serrano, V.G. Hinojosa Chasiquiza, I. Mediavilla-Martínez, and J. Jiménez acknowledge financial support by AEI grants PID2021-126046OB-C22 and TED2021-130786B-I00 (Spain). D. Bricio, J. Llobet, J. Antonja, F. Pérez-Murano, and J. Bausells acknowledge financial support by AEI grant PID2021-126046OB-C21 (Spain).

FIGURES

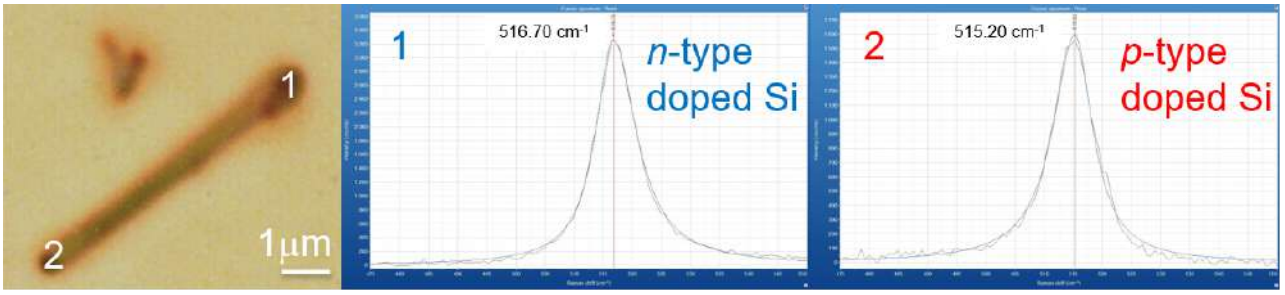

Figure 1. (left) Optical microscopy image of a *p-n* axial junction silicon nanowire (NW). The numbers 1 and 2 denote the *n-* and *p*-type sides of the junction. (center) Typical micro-Raman spectrum of the *n*-type side of the *p-n* axial junction Si NW fitted with a Fano lineshape. Note the asymmetric broadening towards the high energy side. (right) Typical micro-Raman spectrum of the *p*-type side of the *p-n* axial junction Si NW fitted with a Fano lineshape. Note the asymmetric broadening towards the low energy side.

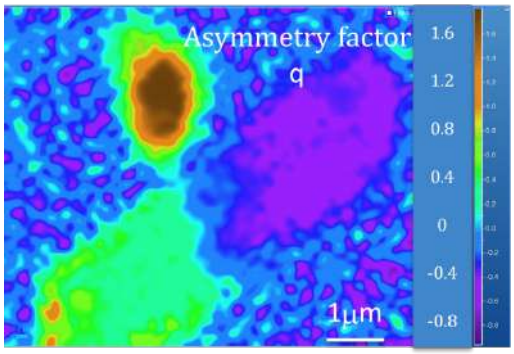

Figure 2. Color map of asymmetry factor *q* from a modified Fano function [3] fit of the micro-Raman spectra at the *p-n* axial junction Si NW shown in Fig. 1. Taken with an excitation laser of 532 nm wavelength, 4.5 mw power and 0.2 s acquisition time. Note the positive and negative values for the asymmetry factor corresponding to *p-* and *n*-type doping edges, respectively.

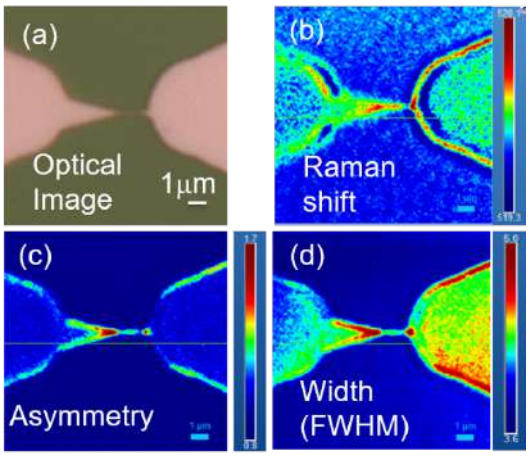

Figure 3. (a) Optical microscopy image of the contacts and Si NW region of a Silicon-on-insulator bottom-up structure for development of Si qubits. Color maps of (b) Raman shift, (c) asymmetry parameter, and (d) full width at half maximum (FWHM) of asymmetric Lorentzian fit to the micro-Raman map of spectra taken with constant step of 0.1 microns and similar wavelength and power than that of Figs. 1 and 2. The small but significant changes in the Raman shift indicate strain induced at the contacts and NW region due to the lithography and etching processing, whereas those of the asymmetric parameter display a combination of the growth of the grain boundaries at the Si NW and the increased doping at that region.

FABRICATION OF ELECTRODES WITH MWCNTS-FUNCTIONALIZED PVDF POLYMERIC MEMBRANES TO BE APPLIED ON MICROBIAL FUEL CELLS.

León Ocaña (1), Orlando Salguero (1), Jonathan Escorza (1), Yolanda Angulo (2), Carlos Reinoso (1).

(1) School of Physical Sciences and Nanotechnology, Universidad de Investigación de Tecnología Experimental Yachay, Urcuquí-Ecuador.
(2) Center for Nanoscience and Nanotechnology, Universidad de las Fuerzas Armadas, Sangolquí-Ecuador.
creinoso@yachaytech.edu.ec

Energy consumption has been growing significantly over the past few decades, with an increasing demand for power to fuel a range of activities, including industrial processes, transportation, and household electricity use. This trend is expected to continue in the future, highlighting the importance of finding alternative, sustainable energy sources. One potential solution is the use of microbial fuel cells (MFCs), which can generate electricity through the decomposition of biomass with the help of functionalized electrodes. These MFCs have several advantages over traditional power generation methods, including a lower environmental impact and the ability to utilize waste materials as fuel. However, one of the challenges in using MFCs is developing efficient and cost-effective electrodes [1]. To address this issue, our research aimed to design a drop angle analysis system to produce conductive coatings using polyvinylidene fluoride (PVDF) membranes dissolved in dimethylacetamide (DMA) and multiwalled carbon nanotubes (MWCNTs) dispersed in varying concentrations. Metal meshes were then used to support these coatings and create the electrodes. To assess the performance of the resulting electrodes, we employed several characterization techniques, including electrochemical impedance spectroscopy (EIS) and cyclic voltammetry (CV) and the SEM images make evident a porosity surface as is seen in Figure 1. These measurements enabled us to optimize the number of layers and the concentration of MWCNTs to achieve the best results in terms of voltage generation. Our results showed that our optimized electrodes were able to generate approximately 100 millivolts of voltage, demonstrating their potential for use in MFCs. Moreover, our approach offers a low-cost alternative that could be particularly valuable for developing countries that lack the resources to invest in more expensive technologies. In addition to the development of MFC electrodes, our research highlights the importance of nanotechnology in advancing sustainable energy solutions. Nanomaterials, such as MWCNTs, have unique properties that make them suitable for a range of energy applications [2]. For example, their high surface area to volume ratio and excellent electrical conductivity makes them ideal for use in energy storage devices and solar cells, also related with the porosity. Nanotechnology has also enabled the development of new materials with improved properties for use in energy conversion and storage. For instance, researchers have designed new catalysts that can improve the efficiency of hydrogen fuel cells, which convert hydrogen into electrical energy. Nanomaterials have also been used to improve the performance of lithium-ion batteries, which are widely used in portable electronics and electric vehicles. In conclusion, the need for sustainable energy solutions is becoming increasingly urgent in the face of rising energy demands and the ongoing climate crisis. Our research demonstrates the potential of MFCs as a renewable energy source, and the importance of developing cost-effective electrodes for this technology. Moreover, our work highlights the significant role that nanotechnology plays in developing sustainable energy solutions, and the potential for further advances in this field to help address the world's energy needs. Cyclic Voltammetry (CV) and Potentiostatic Electrochemical Impedance Spectroscopy (PEIS) are analytical techniques used to investigate the conductive behavior of materials. In this study, the conductive properties of two membranes with varying concentrations of Multiwalled Carbon Nanotubes (MWCNTs) were analyzed using these techniques [3]. The results of the CV analysis revealed the conductivity of the membranes as is seen in Figure 2. The slope of the lines on the graph indicated the conductivity of each membrane, with steeper slopes representing higher conductivities. On the other hand, the PEIS analysis showed the impedance of the membranes. A higher concentration of MWCNTs resulted in lower impedance and, therefore, higher conductivity. These findings have important implications for the design and

optimization of Microbial Fuel Cells (MFCs), which rely on the conductive properties of electrodes to harvest electrons from the decomposition of biomass. By using membranes with high conductivity, MFCs can generate higher voltages and be more effective in converting organic matter into electrical energy.

REFERENCES

[1] Kaur R, Marwaha A, Chhabra VA, Kim KH, Tripathi SK. Recent developments on functional nanomaterial-based electrodes for microbial fuel cells. Renewable and Sustainable Energy Reviews. 2020 Mar 1;119:109551.

[2] Hinds, B. J. (2004). Aligned Multiwalled Carbon Nanotube Membranes. Science, 303(5654), 62–65. doi:10.1126/science.1092048

[3] Streeter I, Wildgoose GG, Shao L, Compton RG. Cyclic voltammetry on electrode surfaces covered with porous layers: an analysis of electron transfer kinetics at single-walled carbon nanotube modified electrodes. Sensors and Actuators B: Chemical. 2008 Aug 12;133(2):462-6.

ACKNOWLEDGMENTS

YA acknowledge to the grant PIC001 2020 from ESPE. OS, LO, CA acknowledge the School of Physical Sciences and its laboratories for the use of the equipment.

FIGURES

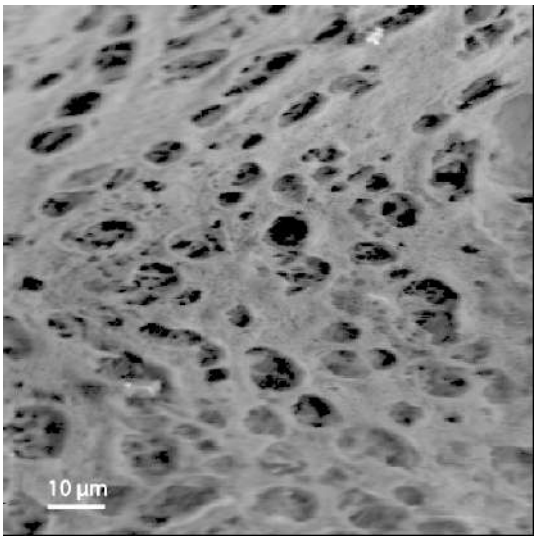

Figure 1. SEM of Electrode surface, the porosity facilitates the interaction between microbials, and the functionalized electrode.

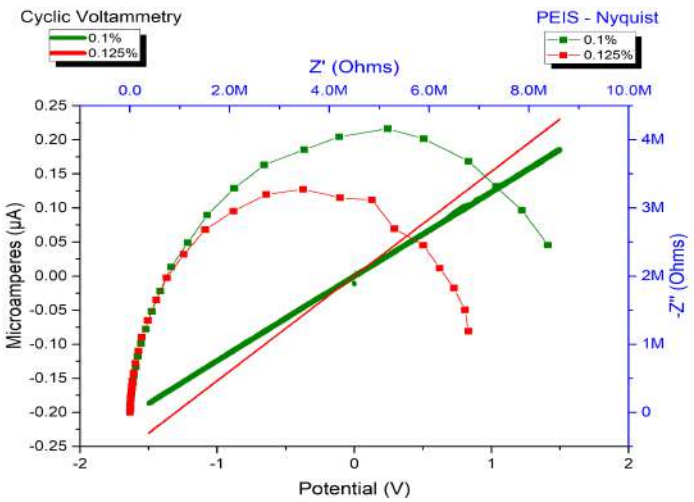

Figure 2. The slope of the lines on the Cyclic Voltammetry (CV) indicated the conductivity. Higher concentration of MWCNTs resulted in lower impedance and, therefore, higher conductivity in the (PEIS) measurement.

Acta Microscopica Vol. 32, Supp. 1, 2023
Abstract Book NSSY 2023- Galapagos 23 -29 April, 2023

$NaGdF_4:Eu^{3+}$ NANOMATERIALS AS MAGNETIC AND OPTICAL PROBES OF BIOLOGICAL SYSTEMS

Andrey S. Mereshchenko (1), Anna A. Betina (1), Tatyana S. Bulatova (1), Bulat S. Akhmadeev (2)

(1) Institute of Chemistry, Saint-Petersburg State University, 7/9 Universitetskaya emb., 199034 St. Petersburg, Russia
(2) A. E. Arbuzov Institute of Organic and Physical Chemistry, Kazan Scientific Center, Russian Academy of Sciences, Arbuzov str., 8, 420088, Kazan, Russia.
a.mereshchenko@spbu.ru

Inorganic nanomaterials containing lanthanide ions are widely studied due to their optical and magnetic properties and broad application within such areas as the design of luminescent thermometers, photocatalysts, solid-state lasers, and solar cells, the development of sensors of biologically important substances, drugs for thermal therapy of tumors and MRI contrast agents, and so on. Such compounds allow making multifunctional materials through a combination of optical, magnetic, radioactive, and other properties, which make them attractive and promising materials for theranostics [1]. These properties make it possible to design multimodal materials for molecular imaging and non-invasive optical diagnostics of tissues of living organisms in vivo using magnetic resonance imaging (MRI), as well as materials for the detection and targeted treatment of cancer cells at early stages of the disease. In this work, we present the results of a study of $NaGdF_4$: Eu^{3+} nanocrystalline materials, which combine luminescent and paramagnetic properties. $NaGd_{1-x}Eu_xF_4$ compounds with different contents of europium and gadolinium (x = 0 - 1) were obtained by hydrothermal synthesis using citric acid as a stabilizing agent [2,3]. Rare earth chlorides taken in stoichiometric amounts (total amount of rare earth chlorides was 0.75 mmol) with 3 mmol of citric acid were dissolved in distilled water to obtain 5 mL solution in total. Then, 2.5 mL of an aqueous solution containing 9 mmol of NaOH was added to the flask of the previous solution. After vigorous stirring for 30 min, 8 mL of aqueous solution containing 11 mmol of NaOH and 11 mmol of NH_4F was added into the above solution. The solution was maintained after vigorous stirring for 30 min at room temperature before being transferred to a Teflon-lined autoclave with an internal volume of 20 mL and heated for 17h at the temperature of 180 °C. After that, the precipitate was separated from the reaction mixture by centrifugation, washed with ethanol and deionized water, and either stabilized by the surfactant or dried at 60 °C for 24 h. We found that all synthesized compounds are solid solutions and have hexagonal β- $NaYF_4$ crystalline phase. Analysis of powder diffraction patterns showed that the substitution of gadolinium ions for larger europium ions leads to an increase in the unit cell parameters and its volume. The linear dependence of the unit cell volume on the concentration of europium ions shows that Vegard's law is obeyed for this series of solid solutions. Scanning electron microscopy showed that the samples consist of particles that have a shape of hexagonal prisms, the average particle size lies in the range of 35–45 nm, and the particle size is practically independent of the composition. The luminescence spectra of the synthesized materials were measured upon excitation at the wavelength of 393 nm into the $^5L_6$ electronic state. The emission spectra consist of narrow lines corresponding to f-f transitions from excited $^5D_0$ to lower energy levels: $^5D_0$–$7F_0$ (582 nm), $^5D_0$–$^7F_1$ (589 nm), $^5D_0$–$^7F_2$ (614 nm), $^5D_0$–$^7F_3$ (649 nm) and $^5D_0$–$^7F_4$ (688 and 694 nm). The radiative transitions $^5D_0$–$^7F_1$ and $^5D_0$–$^7F_2$ are characterized by the highest intensities. The spectra also contain low-intensity transitions from the $^5D_1$ and $^5D_2$ levels to different ^7F_J levels: $^5D_2$–$^7F_2$ (486 nm), $^5D_2$–$^7F_3$ (508 nm), $^5D_1$–$^7F_1$ (524 and 534 nm), nm). The highest luminescence intensity was observed for the $NaGd_{0.7}Eu_{0.3}F_4$ compound; concentration quenching occurs at the higher content of europium ions. $NaGd_{0.7}Eu_{0.3}F_4$ nanoparticles are paramagnetic, the magnetic susceptibility is $7.2 \cdot 10^{-5}$ emu g^{-1} Oe^{-1}, which corresponds to the expected for $NaGdF_4$: Eu^{3+} solid solutions. In order to further use the obtained materials as polymodal bioimaging agents, $NaGd_{0.7}Eu_{0.3}F_4$ particles of about 40 nm in size were stabilized in an aqueous solution using various surfactants: polyvinylpyrrolidone (PVP), sodium dodecyl sulfate (SDS) and cetrimonium bromide (CTAB). It has been shown that CTAB-modified particles are stable in an aqueous solution for at least 48 hours, whereas unmodified particles and particles covered by SDS and PVP aggregate. According to luminescent confocal microscopy, $NaGd_{0.7}Eu_{0.3}F_4$@CTAB and $NaGd_{0.7}Eu_{0.3}F_4$@SDS samples are able to penetrate into HeLa cells showing notable red emission upon 390-nm excitation. The transverse magnetic relaxivity r_2 of the $NaGd_{0.7}Eu_{0.3}F_4$@CTAB sample is 161±7 $s^{-1}mM^{-1}$, which is comparable to commercial contrast agents for

magnetic resonance imaging. The evaluation of the cytotoxicity of colloidal solutions of $NaGd_{0.7}Eu_{0.3}F_4$, $NaGd_{0.7}Eu_{0.3}F_4$@CTAB, and $NaGd_{0.7}Eu_{0.3}F_4$@SDS particles was carried out on HeLa, HEP2-G, and HEK-293 cell lines. The obtained IC50 cell survival values are 15 mg/l for HeLa and more than 25 mg/l for HEP2-G and HEK-293, indicating a low cytotoxicity of these materials. Also, all colloidal solutions demonstrate good hemocompatibility. The data obtained indicate the possible application of surfactant-stabilized $NaGd_{0.7}Eu_{0.3}F_4$ nanoparticles as contrasts for MRI and dyes for luminescence microscopy in living organisms.

REFERENCES

[1] Dong H. et al. *Chem. Rev.* (2015) (115) (10725)
[2] Kolesnikov, I.E. et al. *New J. Chem.* (2021) (45) (10599)
[3] Bogachev N.A. et al. *Nanomaterials* (2022) (12) (2972)

ACKNOWLEDGMENTS

This research was funded by Fellowship of President of Russia MD-1191.2022.1.3. The measurements were performed at the Research Park of Saint-Petersburg State University (“Magnetic Resonance Research Centre”, “SPbU Computing Centre”, “Cryogenic Department”, “Interdisciplinary Resource Centre for Nanotechnology”, “Centre for X-ray Diffraction Studies”, “Chemical Analysis and Materials Research Centre”, and “Centre for Optical and Laser Materials Research”).

FIGURES

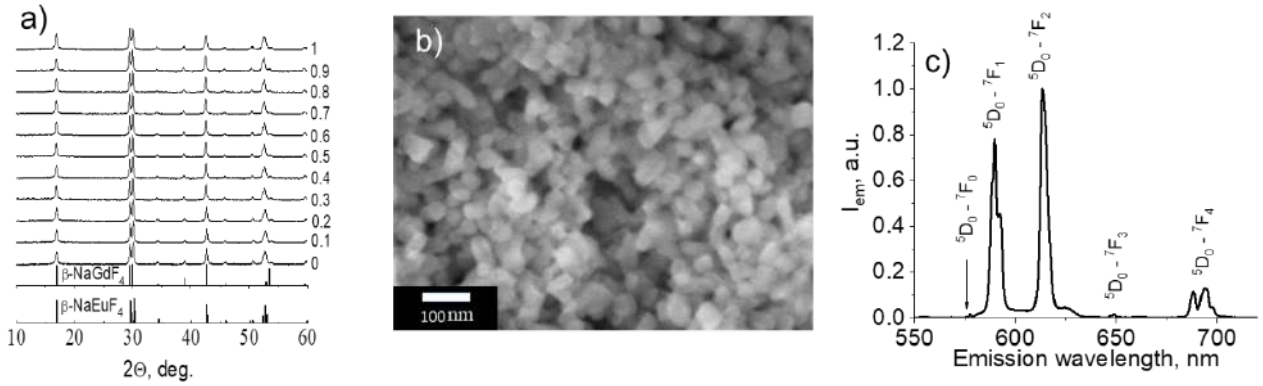

Figure 1. Properties of solid $NaGdF_4$: Eu^{3+} phosphors (a) PXRD patterns (b) SEM image of $NaGd_{0.7}Eu_{0.3}F_4$, (c) emission spectrum of $NaGd_{0.7}Eu_{0.3}F_4$ upon 393-nm excitation

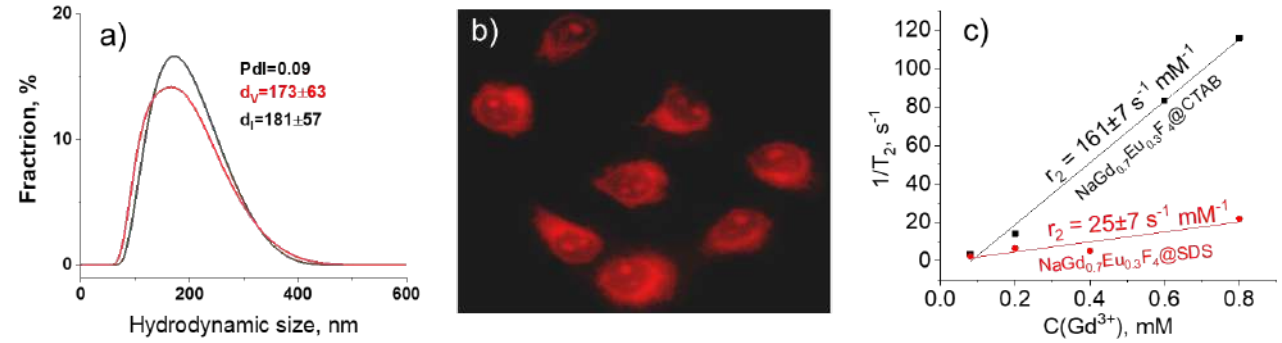

Figure 2. Properties of aqueous solution of surfactant-stabilized $NaGd_{0.7}Eu_{0.3}F_4$ nanoparticles (a) Hydrodynamic size profile and of the CTAB-stabilized $NaGd_{0.7}Eu_{0.3}F_4$ nanoparticles, (b) fluorescence microscopy images M-HeLa cells activated by $NaGd_{0.7}Eu_{0.3}F_4$@CTAB nanoparticles (390 nm excitation, red channel probe, x 400), (c) concentration dependence of $1/T_2$ relaxivity of aqueous solutions of CTAB- and SDS-stabilized $NaGd_{0.7}Eu_{0.3}F_4$ nanoparticles.

SYNTHESIS OF SILVER NANOPARTICLES USING EXTRACT OF GERANIUM (PELARGONIUM DOMESTICUM) AND CARRASQUILLA (BERBERIS HALLII), AND ITS USE FOR IMPROVEMENT IN THE GENERATION OF ELECTRICAL ENERGY IN MICROBIAL FUEL CELLS.

Jonathan Escorza (1), Yolanda Angulo (2), Marbel Torres (3)

(1) School of Physical Sciences and Nanotechnology, Yachay Experimental Technology Research University, Urcuquí Ecuador. (2) Center for Nanoscience and Nanotechnology, Universidad de las Fuerzas Armadas ESPE, Sangolquí-Ecuador. (3) Center for Nanoscience and Nanotechnology, Universidad de las Fuerzas Armadas ESPE, Sangolquí-Ecuador

jescorza@yachaytech.edu.ec

In this project, hybrid biological organism was electrically studied using a microbial fuel cell (MFC) prototype of two chambers separated by a salt bridge. The hybrid organism was developed by adhering silver nanoparticles to cyanobacterium Fischerella musicola.

Previous investigations have qualitatively studied the phenolic content in different plants [1], these compounds, also called polyphenols, are substances that contain an aromatic ring with several hydroxyl substituents and due to their polarity they are soluble in water, which gives them different colorations that are altered by their pH[2]. These organic extracts have been used as reducing agents capable of synthesizing precious metal NPs by controlling their size and shape and without having any environmental impact, in what is known as green NP synthesis. The methods by which metallic NPs are manufactured using green sources include phytological (plants and algae), mycological (fungi) and bacteriological synthesis [3].

Previously to the development of the hybrid organism, the growth of the *Fischerella musicola* cyanobacteria was analyzed with different characterization techniques, for this, the photoperiod and gas exchange parameters were controlled, and the temperature and pH of the medium were monitored. Silver nanoparticles (AgNPs) were synthesized by green chemistry using natural extract such as the geranium flower (*Pelargonium domesticum*) and the carrasquilla fruit (*Rhamnus myrtifolius)* to reduce silver nitrate. In the synthesis process, the pH, temperature and time were controlled to obtain nanoparticle sizes of 17.6313 ± 12.6812nm for geranium AgNPs and 24.1294 ± 7.5146nm for carrasquilla ones. These studies showed that, depending on the reducing agent and the synthesis conditions, the shape and size of the nanoparticle differs. Finally, the hybrid organism was developed through the electrostatic adherence of different concentrations of nanoparticles, the AgNPs and the hybrid organisms were characterized by different techniques.

All the studies showed that for a concentration of 2.6mL of AgNPs from Pelargonium domesticum in 20mL of biomass and 40mL of BG11 medium, the best electrical energy generation efficiency was of 0.8043 ± 0.009V and 19.42uA / cm^2, using a two-chamber microbial fuel cell and salt bridge.

REFERENCES

[1] Reyes, N. M. (2018). Análisis de características diferenciales entre antocianinas y betacianinas en extractos de plantas mediante pruebas de color. *Ambiociencias*(16), 38-48.

[2] CreȚU, G., Morlok, G., & Nechifor, G. DEVELOPMENT OF A QUANTITATIVE HIGH PERFORMANCE THIN LAYER CROMATOGRAPHIC METHOD FOR ANALYSIS OF DELPHINIDIN 3-GLUCOSIDE IN BERRY EXTRACTS. Bhattacharya, R., & Mukherjee, P. J. A. d. d. r. (2008). Biological properties of “naked” metal nanoparticles. *60*(11), 1289-1306.

[3] Ramzan, H., & Yousaf, Z. (2018). Chapter 4 - Green fabrication of metallic nanoparticles. In A. M. Grumezescu (Ed.), *Inorganic Frameworks as Smart Nanomedicines* (pp. 137-183): William Andrew Publishing.

FIGURES

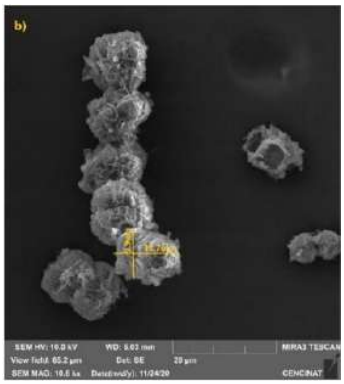

Figure 1. SEM image of Fischerella muscicola

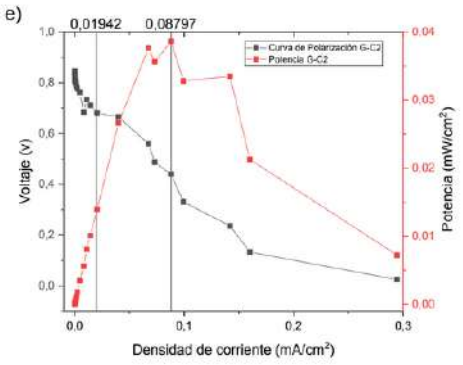

Figure 2. Electrical characterization with MFC of hybrid organisms

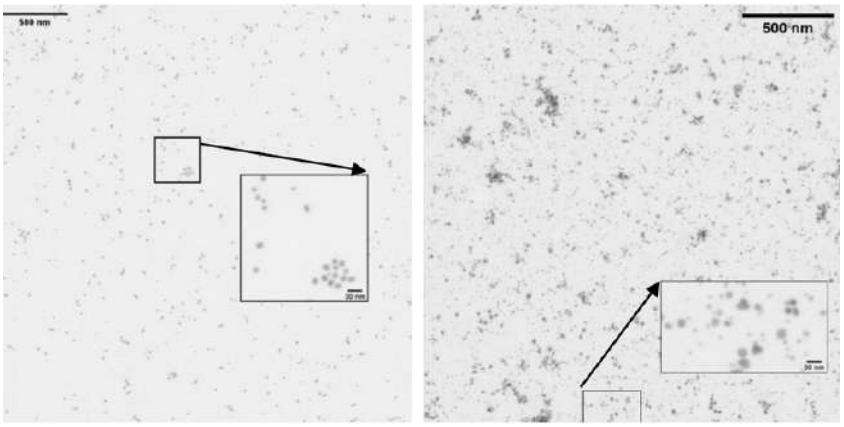

Figure 3. STEM images of AgNPs with Geranium (Right) and Carrasquilla (Left)

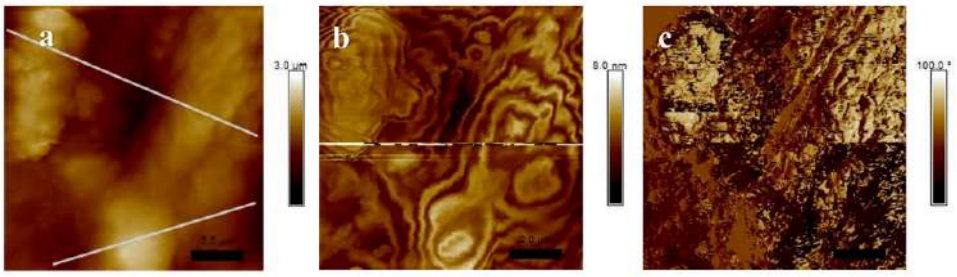

Figure 4. AFM images of electric properties of hybrid organisms

Acta Microscopica Vol. 32, Supp. 1, 2023
Abstract Book NSSY 2023- Galapagos 23 -29 April, 2023

DESIGN OF IMPEDANCE COUPLERS FOR GRAPHENE NANOANTENNA IN THE THZ BAND

Manuel Tipán G[a]*, Daniel González T. [b], Johnny Chimborazo [b], Berenice Arguero T[a]* and Germán V.Arévalo [a].

[a] Grupo de Investigación GIETEC, Carrera de Telecomunicaciones, Universidad Politécnica Salesiana, Quito, Ecuador.
[b]School of Physical Sciences and Nanotechnology, Yachay Tech University, Urcuquí, Ecuador.
jchimborazo@yachaytech.edu.ec

The wireless communications of future generations will require nanoantennas capable of working in the band of Terahertz, however, the miniaturization causes difficulties in conductivity, high propagation losses, and degradation in radiation efficiency. In addition, to obtain the maximum power transfer in a nanoscale wireless communication system, impedance couplers are required. Therefore, a graphene-based patch-type nanoantenna was modeled on two dielectric substrates, silicon, and silicon dioxide, in which a BIAS voltage between 0.83 and 29.9 V was applied. For the coupling of the patch with the power port, direct contact methods were used, such as a 50 Ω microstrip line, inserts in the patch, and the quarter-wave transformer.
The best results obtained from the performance comparison were with the quarter wave transformer with a return loss of -33.54 dB, gain 5.6 dBi, directivity 6.05 dBi, VSWR of 1.15, a bandwidth of 350 GHz, efficiency of 92%, HPBW 99.2°, F/B 12.8 dB for a resonance frequency of 2.6 THz and in the case of 4.2 THz a return loss of -35.24 dB, gain 4.9 dBi, directivity 5.6 dBi, VSWR of 1.13, bandwidth 187 GHz with 90% efficiency, HPBW 106.5°, F/B 12.2 dB. So, the quarter wave transformer is optimal for matching impedances, achieving low propagation losses, and complying with the optimal operating parameters.

REFERENCES

1 J. N. George, M. G. Madhan, Physica E: Low-dimensional Systems and Nanostructures, vol. 94, pp. 126–131, 2017.

2 J. M. Shalini, M. G. Madhan, Optik (Stuttg), vol. 194, p. 163050, 2019.

3 I. Llatser, C. Kremers, A. Aparicio, J. M. Jornet, E. Alarcón, D. N. Chigrin, *Photonics and Nanostructures - Fundamentals and Applications*, vol. 10, no. 4, pp. 353–358, 2012.

4 S. Abadal, S. E. Hosseininejad, A. Aparicio, E. Alarcon, *2017 40th International Conference on Telecommunications and Signal Processing (TSP)*, Jul. 2017, pp. 817–820.

FIGURES

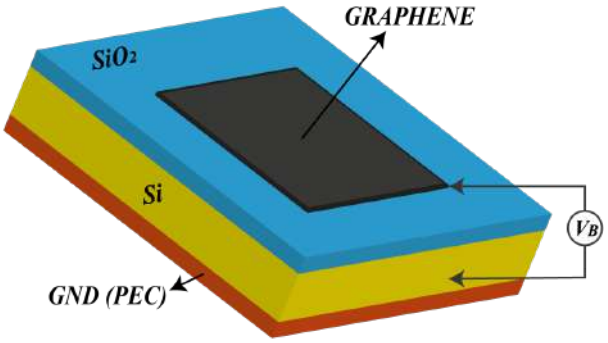

Figure 1. Nanoantenna Components

Table 1: Characteristics of the dielectrics and ground plane of the nanoantenna.

Parameter	Substrate 1	Substrate 2	GND
Material	Silicon	SiO_2	
Er	11,9	4	
Loss Tan∂	0,009	0,005	PEC
Thickness	1.5/1.57 [um]	0.025 [um]	

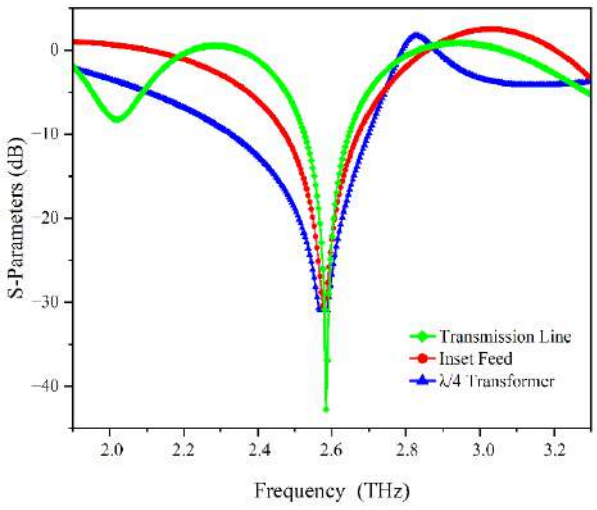

Figure 2. S-Parameters at 2.6 THz.

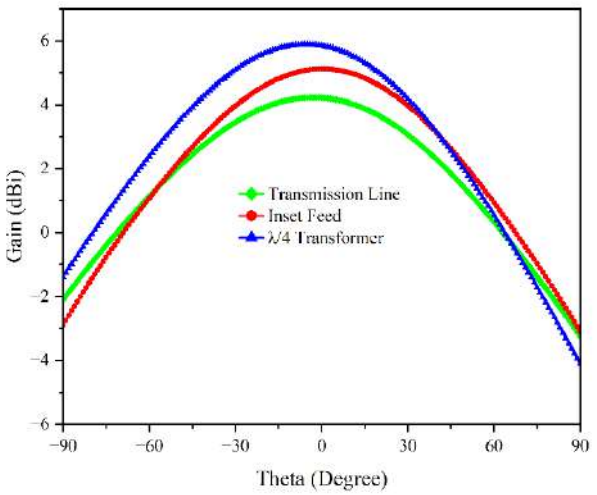

Figure 3. Gain at 2.6 THz.

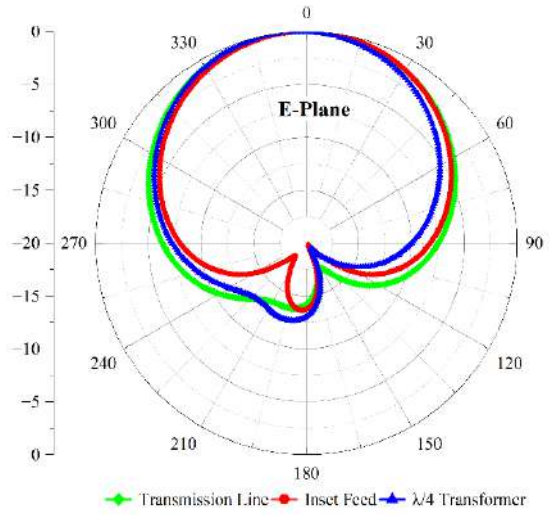

Figure. 4. Radiation pattern at a frequency of 2.6 THz.

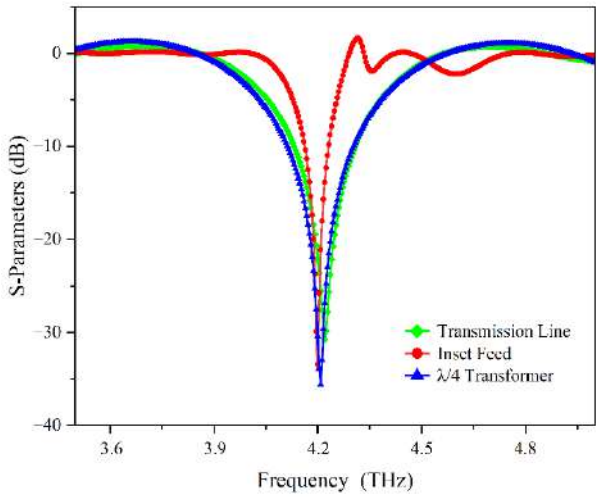

Fig. 5. S-Parameters at 4.2 THz.

Acta Microscopica Vol. 32, Supp. 1, 2023
Abstract Book NSSY 2023- Galapagos 23 -29 April, 2023

TUESDAY

Molecular Modelling of Nanostructures

Acta Microscopica Vol. 32, Supp. 1, 2023
Abstract Book NSSY 2023- Galapagos 23 -29 April, 2023

SCANNING THE ELECTROMAGNETIC EIGEN-MODES IN LAYERED VAN DER WAALS HETEROSTRUCTURES

Vito Despoja(1,2) and Neven Golenić(3,4)

(1)Institute of Physics, Bijenička 46, 10000 Zagreb, Croatia
(2) Donostia International Physics Center (DIPC), P. Manuel de Lardizabal, 4, 20018 San Sebastián, Spain
(3)Department of Physics, Faculty of Science, University of Zagreb, Bijenička 32, 10000Zagreb, Croatia
(4)Scuola Internazionale Superiore di Studi Avanzati (SISSA), Via Bonomea 265, 34136 Trieste, Italy
vito@phy.hr

Recently, the electromagnetic modes in atomically thin van der Waals (vdW) layered heterostructures have shown great potential for their practical applications in plasmonics, photonics and optoelectronics. For example, by vertical stacking of various transition metal dichalcogenides (TMDs), hexagonal boron nitride (hBN) and graphene (Gr) the heterostructure of varous optical properties can be achieved which can act as a photo-sensor, photovoltaic or photo-emitter [1,2,3]. Here we present the results of our recently proposed theoretical approach [4], which is applied to study the electromagnetic eigen-modes in layered conducting and semiconducting van der Waals (vdW) heterostructures. Obtained results for diverse and tunable *Dirac plasmon - polaritons* ((DPP) in Gr/hBN and Gr/$FeCl_3$ multilayers will be presented and compared with recent Scanning Near-Field Microscopy (SNOM) measurements. The occurrence of exotic, transversal polarisation mode (called *trapped photon*) in semiconducting vdW heterostructures will be demonstrated [5,6]. The *trapped photon* (T-ph), built from inter-band electron-hole excitations (not necessarily from excitons) and the transversal photons, is the transversal counterpart to DPP in conductive 2D materials, built from intra-band electron-hole excitations and the longitudinal photons. **Figures 1(a-d)** show the results for T-ph normalised oscillatory strengths f_x/N in WS_2/hBN multilayers and compare with normalised oscillatory strengths $f_{x,y}/N$ of T-ph and DPP in Gr/hBN multilayers. We obtained that T-ph in WS_2/hBN bilayer (N=2) is 29 times stronger then T-ph and even 7 times stronger than DPP in heavily doped ($n=10^{14}cm^{-2}$) Gr/hBN bilayer **Fig.1(c)**. We present the results for T-ph intensity in WS_2/hBN multilayers, in (**Q**,ω) and spatial **ρ**=(x,y) space simulating the SNOM measurements. **Figures 1 (e)** and **(f)** show the SNOM simulations of T-ph and DPP in WS_2/hBN and in doped Gr/hBN trilayers, respectively.

REFERENCES

[1] F. Bonaccorso, Z. Sun, T. Hasan and A. C. Ferrari, Nature Photon 4, 611 (2010)
[2] L. Britnell, et al, Science 340, 1311 (2013)
[3] J. Wang, X. Mu, M. Sun b, T. Mu, Applied Materials Today 16, 1-20 (2019)
[4] D. Novko, K. Lyon, D. J. Mowbray, and V. Despoja, Phys. Rev. B 104, 115421 (2021)
[5] S. A. Mikhailov and K. Ziegler Phys. Rev. Lett. 99, 016803 (2007)
[6] V. Despoja and L. Marušić, Int. J. Mol. Sci. 23, 6943 (2022)

ACKNOWLEDGMENTS

The authors acknowledge financial support from Croatian Science Foundation (Grant no. IP-2020-02-5556) as well as from European Regional Development Fund for the "QuantiXLie Centre of Excellence" (Grant KK.01.1.1.01.0004).

FIGURES

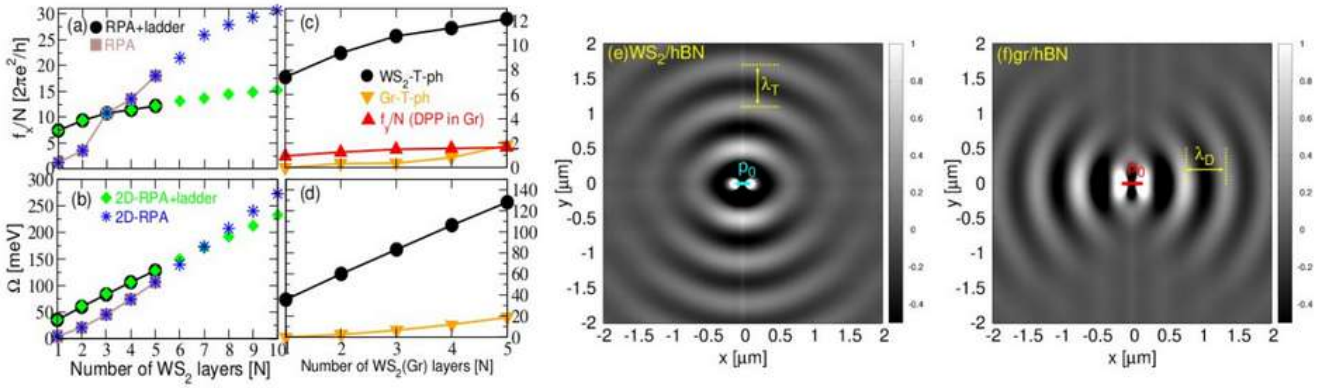

Fig.1 (a) The T-ph normalised oscillatory strength f_x/N and (b) bending Ω as a function of the number of WS_2 single-layers (N) in WS_2/hBN heterostructure obtained using (●) RPA+ladder, (■) RPA, (◆) 2D-RPA+ladder and (★) 2D-RPA models. (c) The T-ph oscillatory strength f_x/N in (●) WS_2/hBN, in (▼) Gr/hBN and (▲) DPP oscillatory strength f_y/N in Gr/hBN multilayers. (d) The T-ph bending Ω in (●) WS_2/hBN and in (▼) Gr/hBN multilayers. (e) The induced current $j^{ind}_x(\boldsymbol{\rho})$ in WS_2/hBN and in (f) graphene/hBN trilayers driven by point dipole $\mathbf{p}$=(1,0) ocillating at frequencies ω_T=1.957eV and ω_D=0.29eV, respectively. The graphene electron doping is n=10^{14}cm^{-2} per Gr layer corresponding the Fermi level shift of E_F=1eV.

Acta Microscopica Vol. 32, Supp. 1, 2023
Abstract Book NSSY 2023- Galapagos 23 -29 April, 2023

SAFE AND SUSTAINABILITY-BY-DESIGN: CHALLENGES AND ADVANCED IN COMPUTATIONAL DESIGN OF ADVANCED MATERIALS

Alicja Mikolajczyk (1, 2)

(1) [a] Laboratory of Environmental Chemoinformatics, Faculty of Chemistry, University of Gdansk, Wita Stwosza 63, 80-308 Gdańsk, Poland, (2) QSAR Lab Sp. Z o. o., Trzy Lipy 3, 80-172, Poland
fourth author. Times New Roman 10 pt, centered. All Affiliations must include Department/Institution, City and Country.
alicja.mikolajczyk@ug.edu.pl

Engineered nanomaterials (ENMs) enable new and enhanced products and devices in which matter can be controlled at a near-atomic scale (in the range of 1 to 100 nm). However, the unique nanoscale properties that make ENMs attractive may result in as yet poorly known risks to human health and the environment. Thus, new ENMs should be designed in line with the idea of safe-and-sustainable-by-design (SSbD). The biological activity of ENMs is closely related to their physicochemical characteristics, changes in these characteristics may therefore cause changes in the ENMs activity. In this sense, a set of physicochemical characteristics (for example, chemical composition, crystal structure, size, shape, surface structure) creates a unique 'representation' of a given ENM. The usability of these characteristics or nanomaterial descriptors (nanodescriptors) in nanoinformatics methods such as quantitative structure–activity/property relationship (QSAR/QSPR) models, provides exciting opportunities to optimize ENMs at the design stage by improving their functionality and minimizing unforeseen health/environmental hazards. A computational screening of possible versions of novel ENMs would return optimal nanostructures and manage ('design out') hazardous features at the earliest possible manufacturing step. Safe adoption of ENMs on a vast scale will depend on the successful integration of the entire bulk of nanodescriptors extracted experimentally with data from theoretical and computational models. This Review discusses directions for developing appropriate nanomaterial representations and related nanodescriptors to enhance the reliability of computational modelling utilized in designing safer and more sustainable ENMs.

REFERENCES

[1] Wyrzykowska E., Mikolajczyk A., et al. *Nature Nanotechnology*, **17**, pages924–932 (2022)

ACKNOWLEDGMENTS

This work has received funding from the European Union's Horizon 2020 research and innovation program under grant agreement No 814426 (NanoInformaTIX project), No 953152 (DIAGONAL project) and No 101058784 (NOVUEAU project).

PHOTOINDUCED QUANTUM TRANSPORT

Duncan J. Mowbray (1), Jeyson P. Alomoto-Catota (1), Daniel E. Gonzalez Tamayo (1), Vito Despoja (2)

(1) School of Physical Sciences and Nanotechnology, Yachay Tech University, Urcuqui 100119, Ecuador. (2) Institute of Physics, 10000 Zagreb, Croatia.
duncan.mowbray@gmail.com

A commonly used metric for rating solar cells is their external quantum efficiency (EQE), which is the fraction of incident photons of a particular energy that generate charge carriers. Although this ignores both the power produced by those charge carriers and the availability of photons of that energy in the solar spectrum, it provides a balanced, simple, and general method for comparing photovoltaic materials on a common footing. For this reason, efficient ab initio methods that can semi-quantitatively describe a material's EQE are needed. To do so, the material's optical absorption, charge carrier generation, and the resulting charge transport at a quantum level are needed to describe the EQE of a photovoltaic device. Here, we extend the non-equilibrium Green's function formalism to describe the entire photoinduced quantum transport process within a device, as depicted schematically in Figure 1. This method provides an efficient means for estimating the EQE of photovoltaic devices, allowing their design in silico.

FIGURES

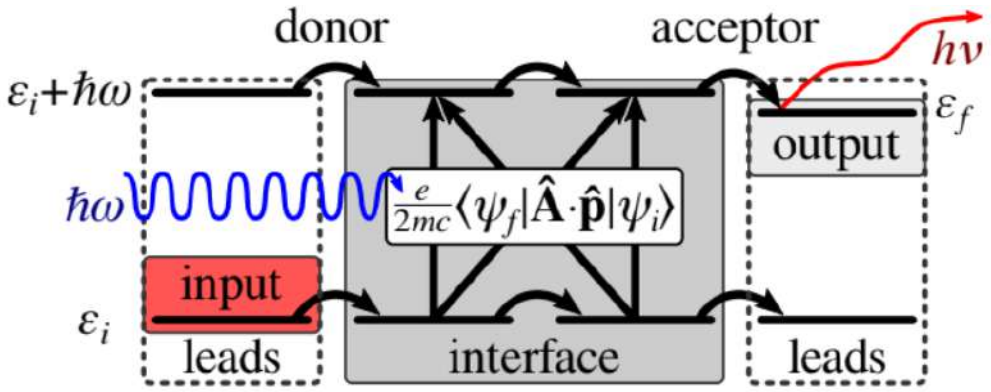

Figure 1. Schematic of an excitation process across a donor–acceptor interface from an occupied initial state in the input lead to an unoccupied intermediate state via the interaction between an external electromagnetic field with vector potential Â and momenta p and via coupling to a phonon mode to an unoccupied final state in the output lead.

Acta Microscopica Vol. 32, Supp. 1, 2023
Abstract Book NSSY 2023- Galapagos 23 -29 April, 2023

ELECTRONIC AND SPIN TRANSPORT IN MOLECULAR JUNCTIONS

Carlos Sabater

Departamento de Física Aplicada and Instituto Universitario de Materiales de Alicante (IUMA), Universidad de Alicante,Campus de San Vicente del Raspeig, E-03690 Alicante, Spain.
carlos.sabater@ua.es

Atomic or molecular contacts have always been an excellent testing bench for the study of electronic and spin transport. Additionally, when the contact is formed by a single atom or molecule, it becomes more interesting since we can obtain mechanical, electrical, and magnetic properties for this unique element. The electronic transport approach is usually studied through Break-Junctions (BJ) experiments, with the most common techniques being Scanning Tunneling Microscopes (STM-BJ) and Mechanically Controllable Break Junctions. On the other side, it is common in theoretical studies to use molecular dynamics (MD) simulations to obtain the trajectories of all atoms or molecules when emulating an experiment, or ab initio calculations based on Density Functional Theory (DFT) when calculating electronic transport.
Our research focuses on studying quantum transport in atomic and molecular conductors. We employ a variety of techniques to investigate this phenomenon, including STM-BJ and MCBJ experiments, MD simulations, and electronic transport calculations based on DFT. Depending on the requirements of each experiment, we can perform measurements at either cryogenic or room temperature conditions. Recently, we have incorporated spin-lattice simulations [1] into our MD models, and our DFT calculations count with the implantation of the spin-orbit coupling effect [2].
Here we present our experimental and theoretical results on electronic and spin transport in atomic contacts.
Thanks to our theoretical-experimental findings in bilayers of bismuth (111), we detected the Quantum Spin Hall insulator behavior at room conditions [3]. Furthermore, our experimental and theoretical results on nickel nanocontacts explain how the electronic transport is affected by the presence of magnetic domains [1].
Regarding molecular electronics-spintronics, we have two important messages to share. First and foremost, our theoretical-experimental results show that organic solvents play a role in molecular electronics. Our findings demonstrate that some solvents never fully evaporate, and their electronic transport must be considered [4,5]. Secondly, we present our experimental and theoretical results in molecular electronic-spintronics based on the Chiral Induced Spin-Selectivity (CISS) effect. Our results on dithiahelicene molecules (see figure 1) demonstrate an interesting behavior in electronic transport experiments [6,7]. We also have used DFT to calculate electronic and spin transport for the previously mentioned molecules, and our theoretical results lead to new questions and insights on the CISS effect. Moreover, our computational results have revealed that non-magnetic metallic nanocontacts can exhibit spin polarization when a rotation is introduced in the electrodes (see figure 2), in other words, the CISS effect can be produced without chiral molecules and can be explained by a matter of symmetry [2].
In summary, based on our findings, we present here an improvement in the understanding of electronic and spin transport in single atomic and molecular junctions.

REFERENCES

[1] Dednam W. et al. Phys. Rev. B. (2020) (102) (245415).
[2] Dednam W. et al. ArXiv.(2022) (arXiv:2211.04830v2).
[3] Sabater C. et al Phys. Rev. Lett. (2013) (110) (176802).
[4] de Ara T. et al. Mat. Chem. Phy. (2022) (291) (126645).
[5] Martinez-Garcia A. et al. ArXiv. (2023) (arXiv:2302.08389v1).
[6] Baciu B. et al. Nanoscale Adv. (2020) (2) (1921).
[7] Baciu B. et al. J. Mater. Chem. C. (2022) (10) (14306).

ACKNOWLEDGMENTS

This work was supported by the Generalitat Valenciana through CIDEXG/2022/45, CIGRIS/2021/159, CDEIGENT/2018/028, and PROMETEO/2021/017.

FIGURES

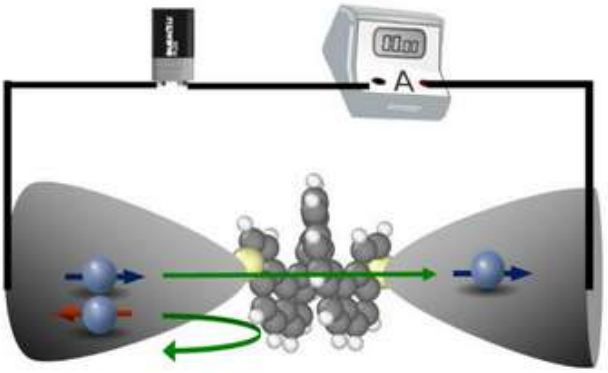

Figure 1. Illustration of a dithiahelicene molecular junction acting as a spin filter.

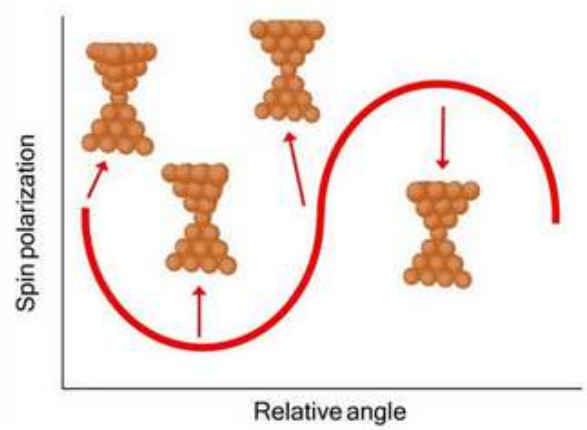

Figure 2. Illustration of spin polarization varies the relative angle between electrodes in atomic-sized contact.

Acta Microscopica Vol. 32, Supp. 1, 2023
Abstract Book NSSY 2023- Galapagos 23 -29 April, 2023

CVD GROWTH AND GAS SENSING PROPERTIES OF METAL OXIDE AND TRANSITION METAL DICHALCOGENIDE MATERIALS

Fatima Ezahra Annanouch (1) Èric Navarrete Gatell (1), Carla Bittencourt (2) and Eduard Llobet (1)

(1) Universitat Rovira i Virgili, Electronic Engineering, Avda. Països Catalans, 26, 43007 Tarragona, Catalonia, Spain.
(2) Plasma-Surface Interaction Chemistry, Chemistry Department, University of Mons, Mons, Belgium.
eduard.llobet@urv.cat

Year by year, gas sensors have known tremendous developments in terms of sensing materials, size, power consumption and fabrication costs. They are becoming indispensable items in the monitoring of indoor and outdoor toxic gasses, and thus play an increasing role in environmental monitoring, air quality control or in safety and security applications. Exposure to high concentrations of toxic gasses is a serious health threat [1]. Hence, developing a new generation of gas sensors that can monitor such pollutant gasses in real time and can detect concentrations from as low as a few parts per billion to several hundred parts per million in the air is of a strong industry demand. In this context, chemiresistive sensors based on nanostructured metal oxide semiconductors, such as WO3, ZnO, SnO2 and In2O3, only to cite a few have been extensively used for detecting pollutant gasses, owing to their advantages of sensitivity, low cost, simple fabrication process and reliability. They were launched as building block materials for gas sensors, owing to their high surface-to-volume ratio, low number of defects, electron confinement effect, etc. In the first part of my lecture, I will describe how pristine and metal nanoparticle loaded metal oxide nanowires (see Figure 1, top row) can be grown via the aerosol-assisted chemical vapor deposition and I will discuss their gas sensing properties and will also introduce their gas sensing mechanisms [2,3]. Lack of selectivity and humidity cross-sensitivity remain the major drawbacks to overcome in metal oxides. Additionally, these nanomaterials are normally operated at 100–400 °C, leading to high power consumption and reduced sensor stability and lifetime, owing to thermally induced changes in morphology and poisoning effects.
These drawbacks are limiting the adoption of metal oxide nanomaterial chemiresistors in the wider real-time applications. In a quest for overcoming such drawbacks, researchers have recently drawn towards atomically layered two- dimensional (2D) transition metal dichalcogenide (TMDs) nanomaterials. TMDs possess unique properties such as semiconducting properties, direct band gap, high specific surface areas due to their sheet-like structures with large basal planes and highly-reactive edges. TMDs consist of a metal atomic layer (such as Mo, W, Hf, Ti, Zr, V, Nb, Ta, Re, etc) collocated between two chalcogen atomic layers (S, Se or Te) and then, these 2D trilayers may appear stacked in multilayer structures due to van der Waals interactions. In the second part of my lecture I will report the bottom-up synthesis of pure and metal oxide loaded transition metal di-chalcogenides (TMDs) such as WS2, WSe2, MoS2 employing different chemical vapor deposition (CVD) methods. These materials comprise ultra-thin films and 3D assemblies of vertically-aligned TMD (see Figure 1, bottom row) nano-flakes and nano-triangles (pristine or loaded with metal/ metal oxide nanoparticles). These materials are grown directly onto application substrates with interdigitated electrodes for achieving chemo-resistive devices [4-6]. The morphological, structural and chemical characteristics will be discussed by using FESEM, TEM, EDX and XPS analysis. Full gas sensing studies towards toxic gases and vapors such as nitrogen dioxide, hydrogen sulfide and ammonia will be shown and discussed as well. These will comprise sensitivity, selectivity, limits of detection, moisture cross-sensitivity effects and long term stability. The effects of the operating temperature on sensitivity and baseline recovery will be addressed. Finally, gas sensing mechanisms will be presented and discussed in detail.

REFERENCES

[1] Occupational Safety and Health Administration, Permissible Exposure Limits – Annotated Tables https://www.osha.gov/annotated-pels/table-z-1 (accessed Nov 10, 2022).
[2] Annanouch, F.E. et al. ACS Appl. Mater. Interfaces 2016, 8 (16).
[3] Annanouch, F.E. et al. ACS Appl. Mater. Interfaces 2015, 7 (12).
[4] Alagh, A. et al. Sensors Actuators B: Chem. 2021, 326, 128813.

[5] Annanouch, F.E. et al. J. Mat, Chem C. J. Mater. Chem. C, 2022,10, 11027-11039.
[6] Alagh, A. et al. ACS Appl. Mater. Interfaces. 2022, 14, 49, 54946–54960.

ACKNOWLEDGMENTS

Funded in part by the Marie Skłodowska-Curie Actions (MSCA) Research and Innovation Staff Exchange (RISE)H2020-MSCA-RISE- 2018- 823895 'SENSOFT', by MICINN and FEDER grant no. RTI2018-101580-I00 and AGAUR grant no.2017 SGR 418. C.B. is Senior Research Associate of the national funds for Scientific Research (FRS-FNRS, Belgium). E.L. is supported by the Catalan Institute for advanced studies (ICREA) via the 2018 Edition of the ICREA Academia Award.

FIGURES

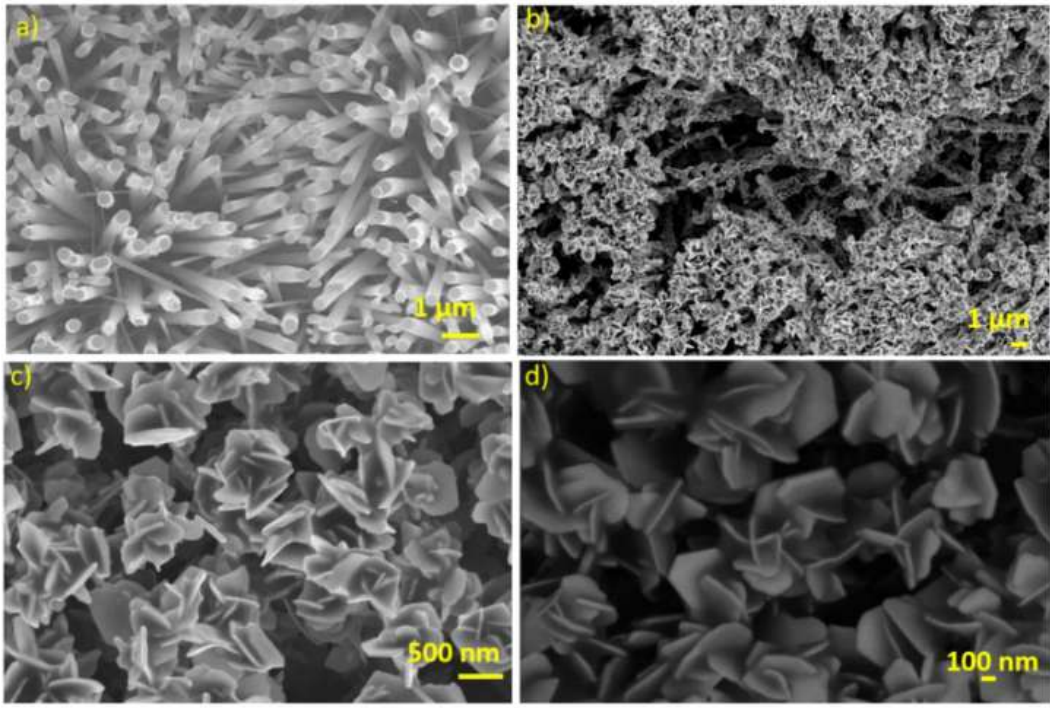

Figure 1. SEM and FESEM images depicting the growth of vertically aligned (a) WO3 nanowires (b) WSe2 nanoplatelets (c) (d) WSe2 nanoflowers. Reproduced from [6]. American Chemical Society.

Acta Microscopica Vol. 32, Supp. 1, 2023
Abstract Book NSSY 2023- Galapagos 23 -29 April, 2023

WEDNESDAY

2D Nanomaterials and Heterostructures

Acta Microscopica Vol. 32, Supp. 1, 2023
Abstract Book NSSY 2023- Galapagos 23 -29 April, 2023

WHY FILLED SINGLE-WALLED CARBON NANOTUBES

Paola Ayala (1)

(1) University of Vienna, Faculty of Physics, A1090 Vienna, Austria
paola.ayala@univie.ac.at

The advances on the science and application of carbon nanotubes within the last three decades have brought to reality the production of materials approaching the theoretical predictions. In particular, the outstanding electronic and optical properties of pristine single-walled carbon nanotubes can be clearly unraveled with more than one spectroscopy technique. However, seeking paths to gain control and modify the material´s properties implies understanding interactions of the SWCNTs with other structures or molecules. This is why unraveling the properties of hybrids of SWCNTs, where they encapsulate other structures, still embraces significant challenges. The physical properties of these materials are strongly related to their morphology and diameter. For instance, their photoluminescence (PL) can be modified by molecules or nanostructures inside the tube´s hollow core. This has been observed for bundles or relatively large- diameter tubes. However, small diameter tubes can form novel hybrids confining linear carbon chains or some types of nanoribbons that offer extremely attractive properties. In this presentation, I will show how our efforts towards identifying the charge transfer from encapsulated nanostructures to SWCNT hosts on hybrids confining linear carbon chains and given chirality nanoribbons. We will discuss the extraction of SWCNT-carbon chain-hybrids protected inside their double-walled counterparts, and on how a diameter-dependent enhancement of the PL can be induced by energy transfer. Also, graphene nanoribbons with a defined chirality will be in the focus of this presentation showing how to discern specific Raman active modes independently from non-encapsulated fragments of ribbon-like molecules.

REFERENCES

[1] Milotti V. et al. *Small Methods*, (2022) (6) (2000110).
[2] Rohringer, P. et al *Adv. Funct. Mater*. (2016) (26) (4874).
[3] Denvier van der Gon D. et al. *Manuscript in preparation* (2023)

ACKNOWLEDGMENTS

P. Ayala acknowledges the fruitful collaboration on the presented topics with Thomas Pichler (University of Vienna-Austria), Kazuhiro Yanagi (Tokyo Metropolitan University-Japan), Lei Shi (Sun Yat-sen University-China), Valeria Milotti (ELETTRA-Italy), Manuel Melle Franco and Jorge Laranjeira (University of Aveiro-Portugal). Also the work of the PhD Students of the Tailored Hybrid Structures Group C. Berkmann, D. Denvier van der Gon, J. Benalcázar is kindly acknowledged.

Acta Microscopica Vol. 32, Supp. 1, 2023
Abstract Book NSSY 2023- Galapagos 23 -29 April, 2023

MOLECULARLY DESIGNED 2D MATERIAL ARCHITECTURES: A ROUT TOWARSD APPLICATIONS

Mildred Quintana[1,2]

Facultad de Ciencias[1] and Centro de Investigación en Ciencias de la Salud y Biomedicina (CICSaB)[2], Universidad Autónoma de San Luis Potosí.
mildred.quintana@uaslp.mx

2D materials namely graphene, MoS_2, WS_2, borophene, black phosphorus, hexagonal boron nitride, etc, are exciting materials with a huge potential for the development of new advanced technologies. The unique combination of properties, such as high specific surface area, chemical stability, mechanical strength, flexibility, high electrical and thermal conductivity, and tunable band gap, make them ideal components for the development of several applications including intelligent coatings, conductive inks, reinforced composites, biomedical devices, smart membranes, and environmentally friendly materials. However, for applicability, several problems arise, including scalability, dispersibility and stability. Authors have proposed chemical functionalization as a feasible solution to render 2D materials dispersible in many solvents and readily for its integration in different matrices. Furthermore, by performing chemical reactions, it is possible to exactly tune the interfacial properties to increase compatibility and integration into functional composites. In this presentation, I will describe our recent efforts on the chemical functionalization of 2D materials towards applications.

FIGURES

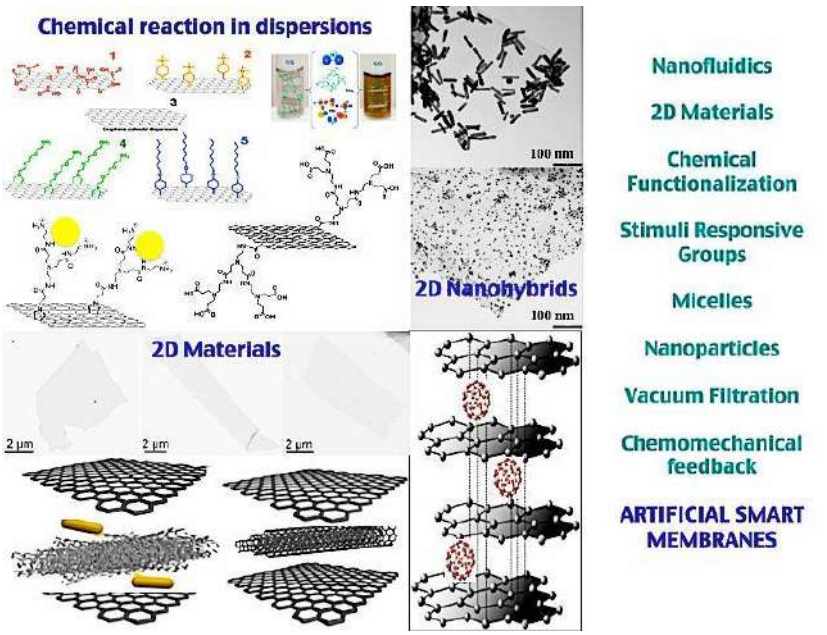

Figure 1. Schematic representation of the chemical functionalization of 2D materials.

Acta Microscopica Vol. 32, Supp. 1, 2023
Abstract Book NSSY 2023- Galapagos 23 -29 April, 2023

2D NANOELECTRODES FOR SINGLE MOLECULE JUNCTIONS

Hillary Rodríguez (1), Selena Barragán (1), Yessenia Falconí (1), Pedro Ortiz (1), Henrry M. Osorio C. (1)
(1) Electronic and magnetic materials group (GI-MEM), Departamento de Física, Escuela Politécnica Nacional. Av. Ladrón de Guevara, E11-253, 170525 Quito, Ecuador.
henrry.osorio@epn.edu.ec

Molecular electronics, in which organic, inorganic or organometallic molecules are connected between two (or three) electrodes to create a nascent electronic device has potential to serve a role in the development of a new technology that could overcome the difficulties now being encountered during top-down scaling of conventional silicon technology. The development and evolution of several experimental techniques, such as scanning tunneling and atomic force microscopies, have enabled us to evaluate the electrical properties across metal-molecule-metal junctions. Together with these techniques, metallic electrodes, especially gold, have been extensively used to address key interrogations related to understanding charge transport mechanisms across the junctions or to propose novel structures to construct molecular diodes or, even better, molecular transistors. However, there are potential drawbacks of using metallic electrodes for the assembly of these junctions, such as: non-compatibility with complementary metal-oxide-semiconductor (CMOS) technologies, surface mobility and high price. Over the last years, the use of non-metallic electrodes has attracted growing attention due to avoiding the use of rare, expensive and potentially toxic materials. Thus, graphene,[1] molybdenum disulfide (MoS2) [2] or gallium arsenide (GaAs) [3] nanoelectrodes have been successfully used to obtain molecular junctions with inherent properties, such us, low attenuation factors, photocurrent or current rectification. Nevertheless, these contacts need expensive methods for deposition or to provide optimal electrical contact. In this talk, I will describe our efforts to construct and characterize molecular junctions based on 2D non-metallic electrodes in a simple way using scanning probe microscopy. Thus, electrical properties of graphene-molecule-gold and MoS2-molecule-gold junctions will be examined. In the first case, multilayer graphene nanosheets were obtained using electrochemical exfoliation of graphite. Subsequently, spray-coated graphene electrodes were constructed from graphene nanosheets. In the second case, multilayer MoS2 nanosheets were obtained using liquid-phase exfoliation of MoS2 powder and after deposited using a drop-casting method to construct a semiconducting electrode. Atomic force microscopy (AFM) was used to evaluate the morphology of the deposited electrodes and scanning tunneling microscopy (STM)-based I(s) method was performed to construct and evaluate the conductance of graphene-molecule-gold and MoS2-molecule-gold junctions. In both cases, the single molecule I-V curve of 4,4'-biphenyldithiol was obtained. A symmetrical I-V curve was obtained for the graphene-molecule-gold junction (Figure 1a), proving that, despite the inherent asymmetry of the molecular junction, no rectification effect was detected. On the other hand, MoS2- molecule-gold junction exhibited an asymmetrical I-V curve (Figure 1b). This indicates the establishment of current rectification, which is related to the asymmetry created with the use of different electrodes to form the junction. In summary, this study paves the way for the use of nanoelectrodes based on 2D-materials to construct single molecule junctions and evaluate charge transport at the molecular level. Importantly, with the use of MoS2 semiconducting nanoelectrodes current rectification is promoted at the molecular level.

REFERENCES

[1] Zhao, S., et al. Nano Research (2021) (1).
[2] Eo, J. S., et al. Advanced Science (2021) (8) (2101390).
[3] Vezzoli, A., et al. Nano Letters (2017) (17) (1109).

ACKNOWLEDGMENTS

Authors are grateful for financial assistance from Escuela Politécnica Nacional in the framework of project PIGR-19-04. In addition, authors thank CEDIA for founding I+D+i-XVII- 2023-48.

FIGURES

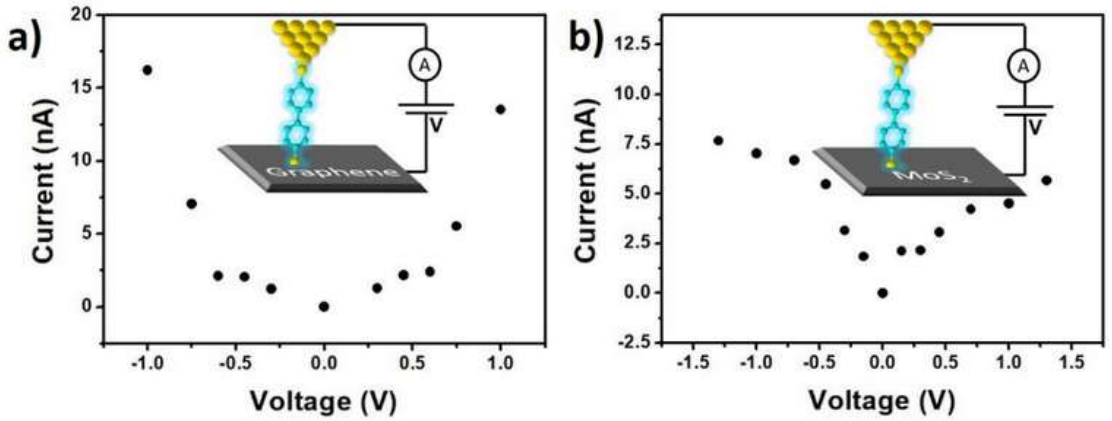

Figure 1. Single molecule I-V curves of 4,4'-biphenyldithiol contacted between two electrodes. a) Graphene-molecule-gold junction and b) MoS2-molecule-gold junction.

Acta Microscopica Vol. 32, Supp. 1, 2023
Abstract Book NSSY 2023- Galapagos 23 -29 April, 2023

RAMAN SPECTROSCOPY: INNOVATIVE SAMPLE SCANNING METHODS, ARTIFICIAL INTELLIGENCE CHEMOMETRICS, IMAGE MICROGEOPROCESSING AND COLOCALIZED MEASUREMENTS WITH SCANNING ELECTRON MICROSCOPY AND X-RAY MICROFLUORESCENCE.

Igor Carvalho (1), Filipe Cabral (1)
(1) Horiba Scientific Brazil, Jundiai – São Paulo, Brazil.
igor.carvalho@horiba.com

This presentation will focus on Raman and NanoRaman applied to the most diverse branches of knowledge. In this presentation you will learn the basic principles of Raman spectroscopy applied to Raman imaging. Applications and instrumentation will be the main topics for a wide range of materials characterization, including polymers, ceramics, biomaterials, life sciences and two-dimensional (2D) materials. Raman and Nanoraman microscopy is one of the only techniques capable of providing non-destructive, accurate analysis combined with high resolution images. Raman spectroscopy provides valuable information about the studied sample, such as chemical and structural composition. Based on the light-matter interaction, we obtain relevant information, such as: particle distribution, homogeneity, grain size, phase changes and several other characteristics of the sample through the chemical evaluation of the material. We will also discuss the combination of laser-excited photoluminescence imaging and Raman scattering of two-dimensional (2D) crystals to reveal the solid-state structure. The development of instrumentation makes possible the hyphenation of Raman with other techniques, such as Photoluminescence and AFM, being able to reach resolutions on a nanometric scale. The technique can be applied in several areas of knowledge, such as pharmaceuticals, photovoltaics, graphene, cells, nanoparticles, microplastics, among others.

DESIGN OF A MULTIFUNCTIONAL NANOSTRUCTURED SYSTEM WITH POTENTIAL APPLICATIONS IN BREAST AND CERVICAL CANCER TREATMENT

Verónica Quilumba-Dutan (1)*, Clara Carreón-Álvarez (2), Sergio Hidalgo-Figueroa (3), Rubén López-Revilla (4), Eugenia Valsami-Jones (5), Swaroop Chakraborty (6), José Luis Rodríguez-López (7)

(1), (7) Advanced Materials Department,
Instituto Potosino de Investigación Científica y Tecnológica, San Luis Potosí, México.
(2) Departamento de Ciencias Naturales y Exactas
Centro Universitario de los Valles, Universidad de Guadalajara, Jalisco, Ameca, México.
(3), (4) Molecular Biology Department, Instituto Potosino de Investigación Científica y Tecnológica, San Luis Potosí, México. (5), (6) School of Geography, Earth, and Environmental Sciences
University of Birmingham, Birmingham, United Kingdom
veronica.quilumba@ipicyt.edu.mx

In 2020, 19.3 million new diagnosed cases of cancer and 10 million cancer deaths were estimated worldwide. Moreover, an estimated 28.4 million new cancer cases are projected to occur in 2040. Particularly, breast and cervical cancers are the most diagnosed cancers and the major cause of cancer deaths in women.[1] Current treatments for the majority of cancers include surgery, chemotherapy, and radiotherapy.[2] However, 45% of cancer patients can be cured by surgery and only 5% can be cured by chemotherapy and radiotherapy.[2] Additionally, cancer radiotherapy requires optimization in terms of how to maximize cancer cell-killing capacity within an acceptable dose that adjacent healthy tissues can tolerate from radiation injury. Also, the administration of drugs during chemotherapy remains having difficulties since the lack of specificity and the poor drug accumulation in the tumors generate undesired side effects in healthy tissues.[3] Alternative solutions to face these challenges include targeted therapy and thermal ablation through the use of nanoparticles (NPs) such as gold NPs with anisotropic morphologies and magnetic NPs.[4] Because of this challenge in current cancer treatment, we have developed a nanostructured modular system with a high degree of hierarchy for the transport and release of drugs, and magneto- and photothermal treatment against cancer. The system consists of magnetic NPs (Fe_3O_4) in the core of a silica (SiO_2) shell and surrounded by multi-branched gold NPs (MBAuNPs). With each of these components, the system comprises superparamagnetic and magnetothermal behavior, hierarchical structure, and photothermal capacity. These properties were confirmed by Scanning (SEM) and Transmission Electron Microscopy (TEM), UV-Vis Spectroscopy, and the measurement of magnetic properties using a Physical Property Measurement System (PPMS). UV-Vis spectrum showed a broad absorbance that includes the near-infrared region (NIR), which makes it possible to use the system in photothermal therapy using radiation with the same wavelength, which is harmless to healthy tissues.[5] Also, SEM and TEM showed a core-shell system with optimal size and morphology (see Fig. 1). Finally, in terms of magnetic properties, the system showed a superparamagnetic behavior, which favors its use in biomedical applications since the NPs do not retain any remanent magnetization once the magnetic field is turned off.[6] In sum, cancer is a global disease with the highest mortality rate.[7] Traditional treatments such as surgery, chemotherapy, and radiotherapy have limited therapeutic effects against cancer and are associated with severe side effects, so they require optimization.[7] We report the development of a multifunctional nanostructured system for local magneto- and photothermal ablation and targeted drug delivery, with potential applications in the treatment of breast and cervical cancers. This purpose was achieved by synthesizing a modular system that is constituted by a magnetic core of Fe_3O_4 NPs, a protective layer of SiO_2, and MBAuNPs. The results imply that the optical, photothermal, and magnetic properties of this system are optimal for biomedical applications.

REFERENCES

[1] Sung H. et al. *CA: a cancer journal for clinicians* (2021) (71) (209-249)
[2] Chatterjee P. and Kumar S. *Materials Today.* (2022) (48) (1754-1758)
[3] Gonzalez-Valdivieso J. et al. *International Journal of Pharmaceutics* (2021) (599) (120438)
[4] Pucci C. et al. *Ecancermedicalscience* (2019) (13)
[5] Carreón-Álvarez C. *AIP Advances* (2020) (10) (125030)

[6] Hervault A. et al. Nanoscale (2014) (6) (11553–11573)
[7] Park W. et al. *Biomaterials research.* (2018) (22) (1-10)

ACKNOWLEDGMENTS

Verónica Quilumba-Dutan acknowledges M.C. Ana Iris Peña-Maldonado, Dr. Héctor Gabriel Silva-Pereyra, and M.C. Beatriz Adriana Rivera-Escoto for their helpful collaboration in the technical measurements using the SEM-EDS, HRTEM, and XRD infrastructure from LINAN-IPICYT. Also, the author appreciates the collaboration of Dr. José Luis Rodriguez-López for making available the laboratory of bio-nanostructures to meet the objectives of this research project. Likewise, the author appreciates all the work and guidance of Dr. Clara Carreón, Dr. Eugenia Valsami-Jones, Dr. Sergio Hidalgo, Dr. Rubén Lopez-Revilla, Dr. José Luis Rodriguez-López, and Dr. Swaroop Chakraborty. Finally, the author acknowledges the scholarship (1089707) offered by CONACYT for pursuing graduate studies.

FIGURES

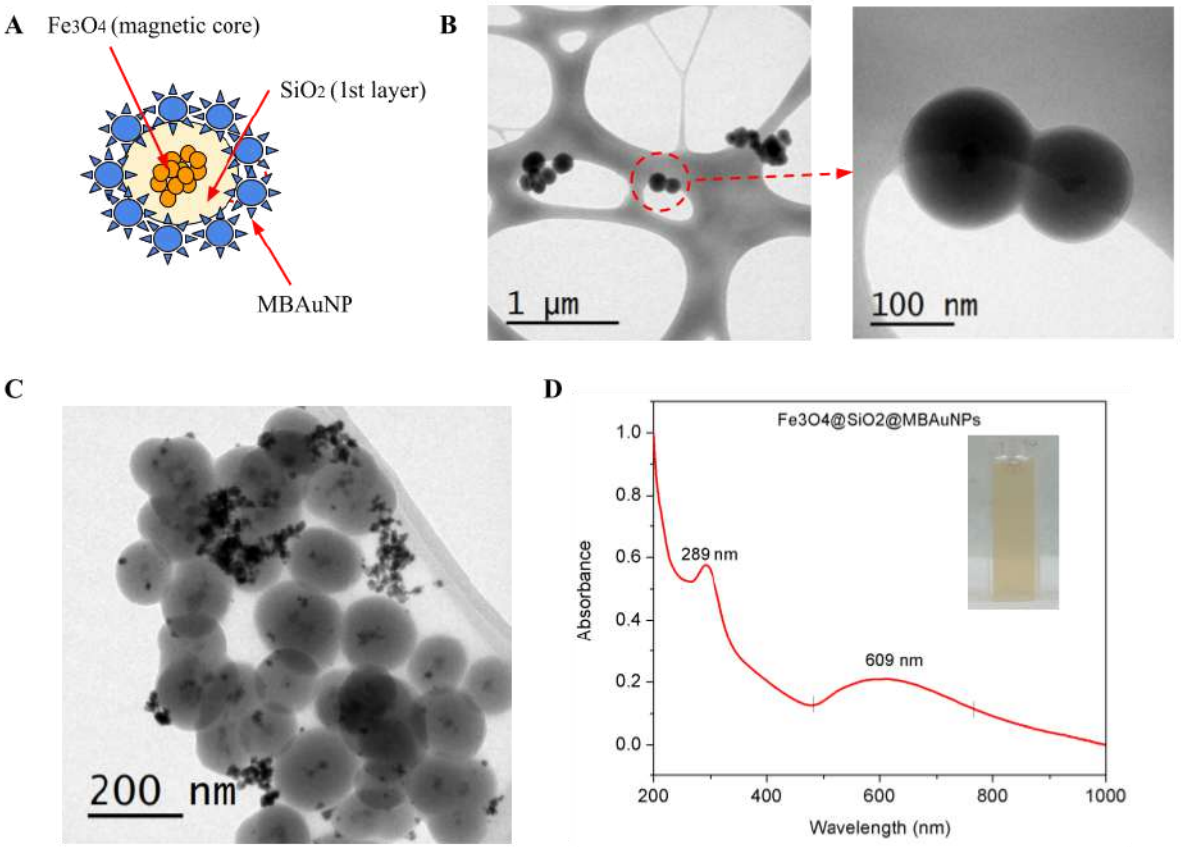

Figure. 1. A multifunctional nanostructured system. **A.** Hypothetical diagram of the modular Fe_3O_4@SiO_2@MBAuNPs system, with each of its components (Fe_3O_4 NPs, SiO_2, and MBAuNPs). **B.** TEM micrograph of core-shell NPs constituted by Fe_3O_4 NPs in the core of a SiO_2 layer. **C.** MBAuNPs surrounding the core-shell NPs in micrograph B. **D**. UV-Vis spectrum for the system Fe_3O_4@SiO_2@MBAuNPs with their maximum absorbance from the UV-Vis region to the NIR region.

Acta Microscopica Vol. 32, Supp. 1, 2023
Abstract Book NSSY 2023- Galapagos 23 -29 April, 2023

MECHANOCHEMICAL SYNTHESIS OF TANTALUM CARBIDE

Adriana Vázquez-Pelayo (1) and Miguel Avalos-Borja (1)

(1) División de Materiales Avanzados, Instituto Potosino de Investigación Científica y Tecnológica, San Luis Potosí, México.
adriana.vazquez@ipicyt.edu.mx

Research on new hard materials has been carried out to improve their characteristics and properties. Currently, materials of light elements and transition metals have gained interest, especially Transition Metal Carbides (TMC) [1]. Tantalum Carbide (TaC) is a promising compound for TMC, as it has very interesting characteristics and properties such as high hardness (17.54 GPa), high melting point (3880 °C) and resistance to chemical attack and oxidation [2]. However, these properties depend on synthesis method, crystalline structure, chemical bond, crystalline defects and grain size. Hot Pressing (HP), Hot Isostatic Processing (HIP) and Spark Plasma Sintering (SPS) are commonly used to consolidate TaC [3]. The aim of the present work was to synthesize TaC by using two very different techniques to improve hardness: mechanical milling (MM) and SPS. MM allows synthesizing materials under environmental conditions generating changes in the morphology and grain size that result in the improvement of hardness. SPS favors atomic diffusion and consolidates the samples at temperatures lower than melting point. Therefore, in this work, TaC was synthesized by MM from a stoichiometric powder mixture of tantalum and carbon with a 1:1 molar ratio. The formation of the material was obtained at 60 min milling time. X-ray diffraction, Scanning Electron Microscopy (SEM) and Transmission Electron Microscopy (TEM) were used to characterize the products. Subsequently, the samples were treated using SPS, reaching a maximum temperature of 1341 °C. Consolidated samples were characterized by X-ray diffraction and X-ray Photoelectron Spectroscopy (XPS) to determine changes in the crystalline structure of the material as well as elucidate the surface chemical composition of the samples. Microhardness was measured using Vickers indentation in accordance with ASTM Standard E384-17 by applying different loads (0.49, 0.98, 2.94, 4.9 and 9.8 N) with a dwell time of 15 s.

After MM, X-ray analysis shows the presence of Ta ($Im\bar{3}m$ space group), TaC ($Fm\bar{3}m$ space group) and WC ($P\bar{6}m2$ space group), WC comes from the milling material (bowl and balls). The morphology of the material is undefined and tends to form agglomerates with an average particle size of 1 µm. The diffraction patterns obtained are characteristic of a polycrystalline material and indicate the presence of TaC. HRTEM analysis shows interplanar distances 2.5 and 2.2 Å, corresponding to (111) and (200) TaC planes, as seen in the $[01\bar{1}]$ zone axis diffraction pattern. Simulations were carried out in the MacTempas software to corroborate the results obtained (see Figure 1).

After SPS treatment, a characterization of the sample was performed with X-ray diffraction and XPS techniques. X-ray diffraction analysis shows the presence of Ta_2O_5 (C2mm space group) which indicate the oxidation of the sample during the SPS, however there is no change in the other phases found in the material after MM. XPS analysis identifies TaC, WC and Ta_2O_5, corroborating the results obtained by X-ray diffraction, additionally, there is no indication of any contaminant on the sample surface. Vickers hardness test shows that hardness decreases as the load increases being a normal Indentation Size Effect (ISE). In the microhardness category with a load of 0.49 N, the sample has a Vickers hardness of 28.6±1.4 GPa, whilst at 0.98 N has a hardness of 23.1±0.9 GPa. On the other hand, within the low load category with an applied load of 4.9 N, the sample has a hardness of 18.2±0.5 GPa GPa and at 9.8 N a hardness of 17.6±0.8 GPa. Comparing the results obtained with other synthesis methods, the hardness in our samples is significantly higher than those reported in the literature (Table 1). Is important to mention that is the first time that TaC is synthesized by MM and afterwards treated by SPS.

REFERENCES

[1] Zhao Z. et al. Annu. Rev. Mater. Res. (2016).
[2] Jiang J. et al. Ceram. Int. (2016) (42) (7118).
[3] Nisar. et al. Int. J. Refract. Met. Hard Mater. (2018) (73) (221).

ACKNOWLEDGMENTS

AV-P acknowledges a scholarship granted by CONACyT. The authors thank LINAN-IPICyT and Polytechnique Montréal for the facilities provided and the access to laboratories. We also acknowledge technical support provided by Beatriz Rivera in X-rays diffraction, Ignacio Becerril in SEM and Vickers hardness test, Jean Philippe Masse in TEM and Josianne Lefebvre in XPS.

FIGURES

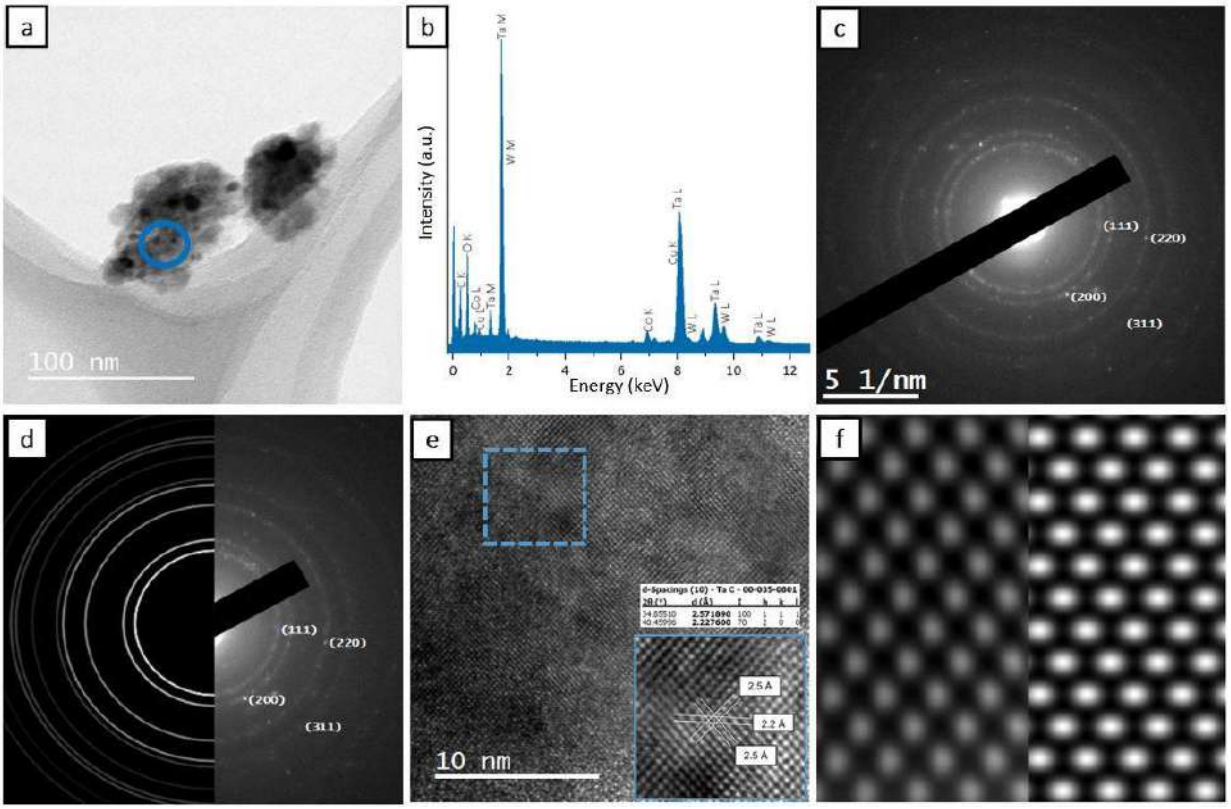

Figure 1. TEM micrographs, a) low magnification, b) EDS from the blue area in a), c) electron diffraction pattern, d) simulated vs experimental DP, e) HRTEM, and f) experimental HRTEM vs simulated.

Table 1. Comparison of Vickers hardness obtained in the present work vs reported in the literature.

Reference	Applied load 9.8 N	Applied load 4.9 N	Applied load 0.49 N
Present work	17.6±0.8 GPa	18.2±0.5 GPa	28.6±1.4 GPa
Cedillos-Barraza et al.	13.9±0.7, 20.4±2.3 GPa		
Silvestroni et al.	11.1±0.7, 13.7±0.3 GPa		
Zhang et al.		14.1±0.2, 16.3±0.2 GPa	
Srinivasa et al.		17.8±3.2, 24.6±2.2 GPa	
Zhao et al.			18.6±0.9 GPa
Weiguo et al.		21.9±0.6 GPa	28.2±0.7 GPa

Acta Microscopica Vol. 32, Supp. 1, 2023
Abstract Book NSSY 2023- Galapagos 23 -29 April, 2023

THURSDAY

Synthesis of Nanostructues

Acta Microscopica Vol. 32, Supp. 1, 2023
Abstract Book NSSY 2023- Galapagos 23 -29 April, 2023

NANOSTRUCTURED SURFACES AS AN INTERESTING ALTERNATIVE FOR ACHIEVING SDG 6 ELECTROCHEMICAL-BASED SOLUTIONS

Karla C. de Freitas Araújo (1), Luis D. Loor-Urgilés (1), Pollyana Castro (1), Amanda D. Gondim (1), Lívia N. Cavalcanti (1), Elisama V. dos Santos (1), Mattia Pierpaoli (2), Mateusz Ficek (2), José Eudes L. Santos (1), Robert Bogdanowicz (2), Carlos A. Martínez-Huitle (1)

(1) Renewable Energies and Environmental Sustainability Research Group, Institute of Chemistry, Federal University of Rio Grande do Norte, Campus Universitário, Av. Salgado Filho 3000, Lagoa Nova, CEP 59078-970, Natal, Rio Grande do Norte, Brazil (2) Faculty of Electronics, Telecommunications and Informatics, Gdańsk University of Technology, 11/12 G. Narutowicza St, Gdańsk 80-233, Poland.
carlosmh@quimica.ufrn.br

In order to create a better and more sustainable future for all societies worldwide, the United Nations Member States have created the Sustainable Development Goals (SDGs). 17 SDGs were established in several subject areas, such as water, energy, climate, oceans, urbanization, transport, science, and technology, to achieve this. Materials science has considerably contributed to the accomplishment of several SDGs, according to report maps of the most current sustainability initiatives and research within each SDG area [3,4]. Advanced materials, for instance, may aid in achieving development objectives in key areas of focus on zero hunger (SDG 2), good health and well-being (SDG 3), clean water and sanitation (SDG 6), affordable and clean energy (SDG 7), industry, innovation and infrastructure (SDG 9), sustainable cities and communities (SDG 11), responsible consumption and production (SDG 12), climate action (SDG 13), and life below water (SDG 14). Then, the scientific and technological domains may develop and construct practical solutions in materials and their applications by identifying essential insights to open novel branches and landscapes for maximizing social benefits. Within this framework, innovative approaches to catalyst creation and electrode production are explored by electrochemistry, electrochemical engineering and material sciences in themes that aim to increase environmental sustainability.

To increase the synergistic effects of electrocatalytic materials to produce potent oxidant species or to increase the active sites on their surfaces, as well as to improve the conversion yield in a fuel cell, high-added-value products, electrolytic treatment for environmental protection, or the detection limit in electroanalysis, the introduction of nanotechnology appears to be a crucial factor. Recently, using the microwave plasma-assisted chemical vapor deposition (CVD) procedure, a novel type of 3D-diamond electrodes with boron-doped carbon nanowalls (B:CNW) was recently produced (Fig. 1), increasing charge transfer and boosting electrochemical performance (Fig. 1a). The usefulness of a boron doped diamond/boron-doped carbon nanowalls (BDD/B:CNW) anodes to degrade organic pollutants has been already examined; however, no efforts at the electrosynthesis of oxidizing species utilizing these diamond-carbon nanostructures have been documented yet. Consequently, the electrosynthesis of sulfate-based oxidizing species was investigated here to provide pertinent answers from both a theoretical and practical standpoint. In the case of electrogenerated oxidizing species, the advances on the identification strategies have facilitated to understand the effect of different experimental factors on their production as well as to comprehend the reactions promoted by them, close to the electrode surface or in the bulk. The majority of EAOPs are based on the production of heterogeneous or homogeneous hydroxyl radicals (•OH) in water medium, and in turn, the modifications in the electrochemical systems to enhance its production, for example, by changing the nature of electrodes (active and nonactive) or by exciting the system with ultrasounds or light irradiation. However, the oxidation via heterogeneous or homogeneous •OH has some advantages and disadvantages. Typically, it quickly occurs as a surface-layer phenomenon inside the reaction cage (i.e. Nernst layer and close to it) with heterogeneous •OH or as volume-oxidation approach in the bulk with homogeneous •OH, due to their concentration and extinction time. For this reason, other oxidants, such as persulfate ($S_2O_8^{2-}$) and sulfate radical ($SO_4^{\bullet-}$), have recently received great attention by the scientific community because of their advantages over •OH, for example, lifetime is more substantial. Persulfate is a relatively stable oxidizing agent that can be electrochemically produced at high concentrations, from the EO of sulfate species see Fig. 1e), depending on the kind of electrode (its formation has been only confirmed at

Pt, doped, and suboxides of Ti, Pb-based oxides, as well as diamond electrodes), electrolyte medium, and its concentration used as well as the current or potential applied. Diamond films are one of the most efficient and inert electrodes for the electrogeneration of $S_2O_8^{2-}$ considering that: (i) $S_2O_8^{2-}$ formation, from the EO of sulfate species, depends on the properties of the electrode (boron doping, sp^2/sp^3 ratio, roughness, electrode support, and thickness), electrolyte medium (sulfuric acid, sulfuric-based acids, or sulfate salts) and its concentration (from 0.1 to 1 mol L^{-1}), as well as the organic-sulfate salt precursor; and (ii) direct ($2SO_4^{2-} \rightarrow S_2O_8^{2-} + 2e^-$, see Fig. 1) or indirect mechanisms are the main routes to electrogenerate $S_2O_8^{2-}$ at diamond films. But, considering that $SO_4^{\bullet-}$ can be generated via reaction with heterogeneous free $^{\bullet}OH$ ($SO_4^{2-} + {}^{\bullet}OH \rightarrow \rightarrow 2SO_4^{\bullet-} \rightarrow S_2O_8^{2-}$), which is formed via water discharge (BDD + $H_2O \rightarrow$ BDD($^{\bullet}OH$) + $H^+ + e^-$, Fig. 1), at indirect mechanism.

In this study, the results revealed that persulfate was easily formed at the BBD electrode, whereas that the ion-radical sulfate might be the most important oxidant at BDD/B:CNW anode when the electrogeneration was compared to other electrocatalytic materials, including BDD surfaces (Fig. 1b). At diamond electrodes, persulfate concentrations varied between 3 and 6 M according to the applied current density (2.5, 5.0, and 15 mA cm^2). Using BDD/B:CNW, methyl orange (MO), a dye-model pollutant, was broken down below the limit of detection in 45 minutes when in-situ sulfate-based oxidizing species were electrogenerated. Residual organic matter in solution, in terms of chemical oxygen demand (COD) values (Fig. 1d), as a function of applied current density (2.5 and 15.0 mA cm^{-2}), after 40 min of electrolysis at different anodic materials in electrochemical oxidation tests at 25 °C showed that BDD/B:CNW anode was an efficient electrocatalytic material, depolluting the synthetic effluent via the action of $S_2O_8^{2-}$ and $SO_4^{\bullet-}$. As innovative electrocatalysts for diverse catalytic applications in the environmental and energy domains, these forms of 3D diamond-carbon nanostructures are therefore promising. In summary, we can conclude that, (i) BDD/B:CNW electrode is constituted by 3D-diamond-carbon nanostructures which increase significantly its electroactive surface area, (ii) in diamond materials, electrochemical measurements have indicated that the complex set of the electrochemical reactions takes at lower and higher over potential regions. However, it mainly seems that the persulfate electrosynthesis depends on the stability/reactivity of $^{\bullet}OH$ and diamond surface active sites to favor the production of SO4−·. In the case of BDD/B:CNW electrode, $SO_4^{\bullet-}$ species are adsorbed at sp^2-active sites, favoring their participation in the oxidation of MO.

REFERENCES

[1] Martínez-Huitle, C.A. et al. *Appl Catal B* (2023) (328) (122430).
[2] de Freitas Araújo, K.C. et al. *Electrochim Acta* (2022) (430) (141069).

ACKNOWLEDGMENTS

Financial support from Conselho Nacional de Desenvolvimento Científico e Tecnológico (CNPq, Brazil) (306323/2018-4, 312595/2019-0, 439344/2018-2, 315879/2021-1, 409196/2022-3, 408110/2022-8), and from Fundação de Amparo à Pesquisa do Estado de São Paulo (Brazil), FAPESP 2014/50945-4 and 2019/13113-4, are gratefully acknowledged.

FIGURES

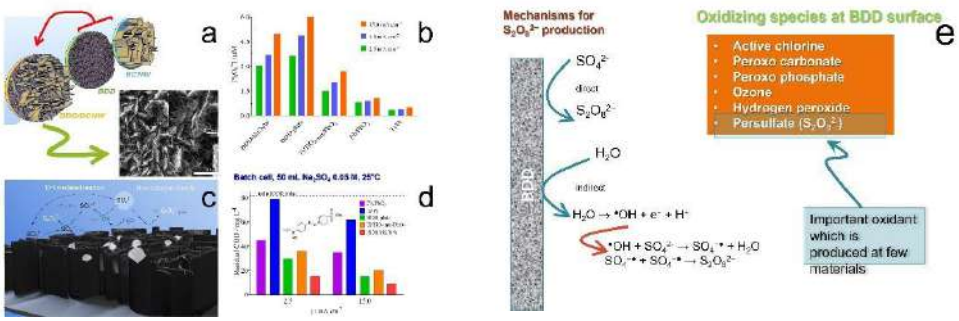

Figure 1. (a) BDD/B:CNW electrode morphology, as observed in the SEM images, (b) production of persulfate at different electrode materials, (c) $S_2O_8^{2-}$ and $SO_4^{\bullet-}$ mechanisms at BDD/B:CNW, (d) COD removal at 2.5 and 15 mA cm^2, (e) persulfate mechanisms electrogeneration.

Acta Microscopica Vol. 32, Supp. 1, 2023
Abstract Book NSSY 2023- Galapagos 23 -29 April, 2023

PURE WATER: THINKING SUSTAINABLY TO REMOVE TOXIC AND RECALCITRANT POLLUTANTS USING NANOPARTICLES AND NANOCOMPOSITES

Víctor H. Guerrero (1), Jennifer Tejedor (1), Carla Valdivieso Ramirez (1)

(1) Department of Materials, Escuela Politécnica Nacional, Quito 170525, Ecuador.
victor.guerrero@epn.edu.ec

Besides impressive social and technological innovations, the last century brought a continuous increase in the population, especially rapid in several developing and emerging countries. This has been associated with growing water, food and energy demands. In particular, the increase in the global demand for clean water and the decrease in the availability of natural renewable resources results in a deteriorating water quality and high pressures on water resources. This, combined with the impacts of phenomena such as climate change and contamination, may have a tremendous effect on agriculture and food supply, health problems, energy markets, and potential for conflicts, among others [1]. Considering these perspectives, it is of paramount importance to develop materials, processes and technologies that could help removing contaminants from water. In this work, the use of nanoparticles and nanocomposites was evaluated, focusing on those that can be synthesized in an environmentally friendly manner, and that can be used to eliminate synthetic dyes, toxic and recalcitrant organic pollutants, and heavy metals. For this purpose, iron oxide and silicon oxide nanoparticles were synthesized using traditional methods, to be compared to eco-friendly approaches employing fruits extracts and organic acids. The nanocomposites were obtained by impregnating the nanoparticles on low-cost, abundant, highly available and easy-to-process agroindustrial lignocellulosic residues. Additionally, graphene oxide (GO) was synthesized following a modified Marcano method, and used to obtain nanocomposites. Characterization techniques such as X-ray diffraction (XRD), scanning (SEM) and transmission (TEM) electron microscopies, dynamic light scattering (DLS), Fourier transform infrared (FTIR), UV-Vis and Raman spectroscopies, and nitrogen adsorption were used to analyze the materials obtained. These analyses allowed to determine the composition, structure, size, surface morphology and functionality, as well as the specific surface area and porosity of the materials obtained. XRD showed that the iron oxide particles were, in general, composed of mixtures of magnetite (Fe_3O_4), hematite (α-Fe_2O_3) and maghemite (γ-Fe_2O_3); while the silica particles were composed of SiO_2. The TEM and DLS analyses confirmed the formation of spherical nanoparticles with sizes ranging from about 5 to 30 nm for the iron oxide, and between about 5 and 10 nm for the silica. FTIR analyses showed that the lignocellulosic residues exhibited mostly hydroxyl and carboxyl groups, which could interact with contaminants and favor their removal from aqueous solutions [2]. Raman spectroscopy analyses performed on the GO exhibited the characteristic D, G and 2D bands, with a I_D/I_G ratio of 0.88, which was greater than that for the graphite (0.43) used as precursor [3]. The specific surface area obtained using the Brunauer-Emmett-Teller method showed values up to about 60, 220, and 260 m^2/g for iron oxide, silica and GO, respectively. The lignocellulosic residues had specific surface areas of the order of 1 m^2/g. Batch test analyses demonstrated that the nanoparticles synthesized using agricultural residues, as extracts or as precursors, showed high adsorption performance for removing dyes (e.g., methylene blue and methyl orange), emerging contaminants (e.g., caffeine, triclosan), and heavy metal ions (e.g., Zn(II), Cr(VI)). It is worth mentioning that the iron oxide nanoparticles also exhibited antioxidant activities against 1,1-diphenyl-2-picrylhydrazyl (DPPH). The lignocellulosic residues (e.g., fruit peels, sawdust) showed also high removal efficiencies but relatively low adsorptive capacities. The addition of nanoparticles to these residues improved the adsorptive capacities and efficiencies, and reduced the optimal contact times for the composites. The adsorption data fitted well, in general, the Freundlich and Sips isotherm models, as well as the pseudo-second-order kinetics model. Summarizing, the results obtained indicate that agricultural residues offer low-cost, sustainable alternatives to synthetize high performance adsorbents. They also allow us to define strategies and select materials that could be advantageously integrated in water treatment technologies.

REFERENCES

[1] Borgomeo E. et al. *Earth's Future* (2020) (8) (e2020EF001495).
[2] Stjepanovic M. et al. *J. Mol. Liq.* (2019) (285) (535).
[3] Almeida-Naranjo C. (2023) *Remediation* (2023).

ACKNOWLEDGMENTS

The authors would like to acknowledge the support of the Escuela Politécnica Nacional through the project grants PIS-18-01, PIGR-19-05, and PIM-20-03.

Acta Microscopica Vol. 32, Supp. 1, 2023
Abstract Book NSSY 2023- Galapagos 23 -29 April, 2023

CITOTOXICITY OF NANOPARTICLES WITH BIOMEDICAL APPLICATIONS AN OVERVIEW

Lenin J. Ramírez-Cando (1), Nayeli Gómez (1), Raúl Davalos-Monteiro (1), Carlos Reinoso (2), and, Ronny Ordoñez (1)

(1) School of Biological Sciences and Engineering, Yachay University for Experimental Technology and Research (Yachay Tech), Hacienda San José S/N, Proyecto Yachay, 100115, Urcuquí, Ecuador.
(2) School of Physical Sciences and Nanotechnology, Yachay University for Experimental Technology and Research (Yachay Tech), Hacienda San José S/N, Proyecto Yachay, 100115, Urcuquí, Ecuador.
lramirez@yachaytech.edu.ec

Recently there has been a great interest in nanoparticles (NPs) as potential therapeutic agents. The shortcomings of conventional non-biological synthesis methods such as generation of toxic byproducts, energy consumptions, and involved cost have shifted the attention towards green syntheses of NPs. Among noble metal NPs, gold nanoparticles (AuNPs), silver (AgNPs) and iron oxides IONPs are the most extensively used ones, owing to their unique physicochemical properties. NPs have potential therapeutic applications, as those are synthesized with biomolecules as reducing and stabilizing agent(s). The new methods of NPs synthesis are simple, eco-friendly, and cost-effective with the use of renewable energy sources, despite this their toxicity is not well-known yet. Although thousands of different nanoparticles (NPs) have been identified and synthesized to date, well-defined, consistent guidelines to control their exposure and evaluate their potential toxicity have yet to be fully established. As potential applications of nanotechnology in numerous fields multiply, there is an increased awareness of the issue of nanomaterials' toxicity among scientists and producers managing them. An updated inventory of customer products containing NPs estimates that they currently number over 5.000; ten years ago, they were one fifth of this. More often than not, products bear no information regarding the presence of NPs in the indicated list of ingredients or components. Consumers are therefore largely unaware of the extent to which nanomaterials have entered our lives, let alone their potential risks. Moreover, the lack of certainties with regard to the safe use of NPs is curbing their applications in the biomedical field, especially in the diagnosis and treatment of cancer, where they are performing outstandingly but are not yet being exploited as much as they could. The production of radical oxygen species is a predominant mechanism leading to metal NPs-driven carcinogenesis. The release of particularly reactive metal ions capable of crossing cell membranes has also been implicated in NPs toxicity. In this overview we discuss the origin, behavior and biological toxicity of different metal NPs with the aim of rationalizing related health hazards and calling attention to toxicological concerns involved in their increasingly widespread use.

Acta Microscopica Vol. 32, Supp. 1, 2023
Abstract Book NSSY 2023- Galapagos 23 -29 April, 2023

CONVERTING POLYMERIC SOLUTIONS INTO BIOMEDICAL NANOFIBERS THROUGH ELECTROSPINNING - AN OVERVIEW OF WORKING PARAMETERS

E. Chuisaca-Londa [a], D. Osorio-Ordóñez [a], J. Dávalos-Monteiro [b], L. Ramirez-Cando [a], R. Dávalos-Monteiro [a, c] *

[a] School of Biological Science and Engineering, Yachay Tech University, Urcuquí, Ecuador.
[a] King Abdullah University of Science and Technology KAUST, Thuwal, Kingdom of Saudi Arabia.
[c] Advanced Materials Research Group (GIMA) - Superior Polytechnical School of Chimborazo, Riobamba, Ecuador.
rdavalos@yachaytech.edu.ec

Electrospinning is perhaps the most flexible method to produce nanofibers nowadays. Polymeric solutions are capable of being converted into nanofibers with a wide variety of biomedical applications, from wound healing textiles to smart and complex drug delivery systems. The production of these biomedical nanofibers depends on the correct application of the working parameters. The analysis of the electrospinning working parameters are divided into three main streams: i) the electrospinning equipment conditions, ii) the polymeric solution properties and iii) the ambient conditions. In this work, a detailed overview of the electrospinning working parameters and their impact in the final production of biomedical nanofibers is presented.

REFERENCES

[1] Teo, W. E., & Ramakrishna, S. (2006). A review on electrospinning design and nanofibre assemblies. Nanotechnology, 17(14), R89.

[2] Agarwal, S., Wendorff, J. H., & Greiner, A. (2008). Use of electrospinning technique for biomedical applications. Polymer, 49(26), 5603-5621.

[3] Poshina, D., & Otsuka, I. (2021). Electrospun Polysaccharidic Textiles for Biomedical Applications. Textiles, 1(2), 152-169.

[4] Sinha, M. K., Das, B. R., Bharathi, D., Prasad, N. E., Kishore, B., Raj, P., & Kumar, K. (2020). Electrospun nanofibrous materials for biomedical textiles. Materials Today: Proceedings, 21, 1818-1826.

[5] Kailasa, S., Reddy, M. S. B., Maurya, M. R., Rani, B. G., Rao, K. V., & Sadasivuni, K. K. (2021). Electrospun nanofibers: materials, synthesis parameters, and their role in sensing applications. Macromolecular Materials and Engineering, 306(11), 2100410.

[6] Chen, S., Li, R., Li, X., & Xie, J. (2018). Electrospinning: An enabling nanotechnology platform for drug delivery and regenerative medicine. Advanced drug delivery reviews, 132, 188-213.

[7] Cseri, L., Topuz, F., Abdulhamid, M. A., Alammar, A., Budd, P. M., & Szekely, G. (2021). Electrospun adsorptive nanofibrous membranes from ion exchange polymers to snare textile dyes from wastewater. Advanced Materials Technologies, 6(10), 2000955.

[8] Sun, G., Sun, L., Xie, H., & Liu, J. (2016). Electrospinning of nanofibers for energy applications. Nanomaterials, 6(7), 129.

[9] Villarreal-Gómez, L. J., Cornejo-Bravo, J. M., Vera-Graziano, R., & Grande, D. (2016). Electrospinning as a powerful technique for biomedical applications: a critically selected survey. Journal of biomaterials science, polymer edition, 27(2), 157-176.

[10] Meinel, A. J., Germershaus, O., Luhmann, T., Merkle, H. P., & Meinel, L. (2012). Electrospun matrices for localized drug delivery: current technologies and selected biomedical applications. European Journal of Pharmaceutics and Biopharmaceutics, 81(1), 1-13.

[11] Cheng, H., Yang, X., Che, X., Yang, M., & Zhai, G. (2018). Biomedical application and controlled drug release of electrospun fibrous materials. Materials Science and Engineering: C, 90, 750-763.

[12] T. Mazoochi, V. Jabbari (2011), Chitosan nanofibrous scaffold fabricated via electrospinning: the effect of processing parameters on the nanofiber morphology, Int. J. Polym. Anal. Char. 16 277–289.

[13] Taylor G (1964) Disintegration of water drops in an electric feld. Proc R Soc Lond A 280(1382):383–397

[14] Haider, A., Haider, S., & Kang, I.-K. (2015). A comprehensive review summarizing the effect of electrospinning parameters and potential applications of nanofibers in biomedical and biotechnology. Arabian Journal of Chemistry. doi:10.1016/j.arabjc.2015.11.015

[15] Hu, J.; Wang, X.; Ding, B.; Lin, J.; Yu, J.; Sun, G. (2011). One-Step Electro-Spinning/Netting Technique for Controllably Preparing Polyurethane Nano-Fiber/Net. Macromol. Rapid Commun., 32, 1729−1734.

[16] Ibrahim, H.M., & Klingner, A. (2020). A review on electrospun polymeric nanofibers: Production parameters and potential applications. Polymer Testing, 90, 106647.

ACKNOWLEDGMENTS

Authors want to thank the Biomaterials Laboratory of the School of Biological Sciences and Engineering at Yachay Tech University for supporting this research project.

FIGURES

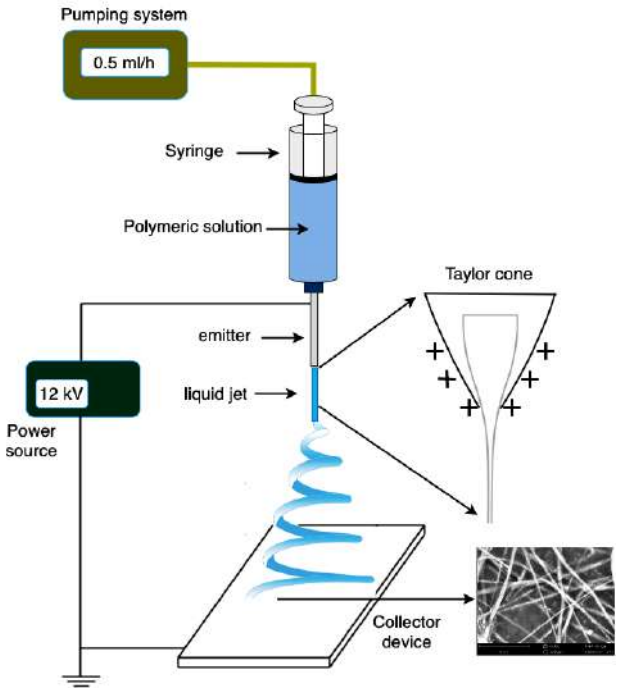

Figure 1. Electrospinning Schematic for nanofiber production

Acta Microscopica Vol. 32, Supp. 1, 2023
Abstract Book NSSY 2023- Galapagos 23 -29 April, 2023

SILVER NANOPARTICLES AND ITS APLICATION IN PRESERVATIVE SOLUTIONS OF CUT FLOWERS

Hilda-Araceli Zavaleta-Mancera (1), Itzel Villegas-Velázquez (1), Columba Vicencio-Salas Solís (2), Luis Manuel Carrillo-López (3).

(1) Botany Department, Colegio de Postgraduados en Ciencias Agrícolas (COLPOS), Montecillo, Texcoco México. (2) Plant Physiology Department, COLPOS (3) Faculty of Zootechnics and Ecology, CONACYT-Universidad Autónoma de Chihuahua, Mexico.
arazavaleta@colpos.mx

Silver nanoparticles (AgNPs) are well recognized by its antibacterial properties because they reduce cytoplasmic membrane thickness, lose the cell wall, and condense DNA molecules. Floriculture is an intensive type of agriculture and the income per unit area from floriculture is much higher than any other branch of agriculture. Cut flowers are very important for human society: they offer beauty and spirit comfort, they offer sick's to speed recovery, they are used to express love, happiness, in birthdays or gratefulness worship in temples. In Mexico, cut flowers are a big industry, 20% of our production is exported to the USA and Canada, but the losses at postharvest carry significant economic losses because of poor management, attack by microorganisms, and vascular system blockage from bacteria and embolism (bubble airs). Ag^{+} are known to be a good antibacterial agent and prevent ethylene ($H_2C=CH_2$) production, the hormone of plant senescence. The objective of the present research was comparing the capacity of biosynthesized AgNPs to extend vase life of Chrysanthemum, Roses and Alstroemeria, which are some of the most commercialized flowers in Mexico and in the world. For *Chrysanthemum* experiments we used AgNps synthesized with 5 mL of *Chemopodium abrosioides* extracts and 10 mM $AgNO_3$ according to López-Carrillo et al. (2014). For Roses and Alstroemeria experiments we used AgNps synthesized with 3 mL *Camelia sinensis* extract according to Nakhjavani, M. et al. (2017). Flowers were obtained from Coxflor company and local growers from the Estate of México. For all experiments the design was completely random with 5-15 replicas. For *Chrysanthemum* cv. Puma, AgNps (10.2 ± 4.3 nm) (0.01, 0.05, 0.1, 0.5, 1.0 mM) were added to the preservative solution: vase life and bacterial counting was compared to control (Fig. 1). Low concentrations (0.01, 0.05 mM) of AgNPs increased vase life, promoted inflorescence diameter, and reduce bacterial count (Table 1). For *Rosa hybrid* cv. Freedom, we use AgNPs of 21.50 ±0.63 (Fig. 2). The treatments were: a) 1.0 mg L^{-1} AgNPs, b) 1.0 mg L-1 AgNPs + 2% sucrose, c) 1.0 mg L^{-1} AgNPs + 80 mgL^{-1} citric acid, pH 4, d) 1.0 mg L^{-1} AgNPs + 2% sucrose + citric acid, e) control (water). Ag NPs + citric acid had the longest vase life, large consumption (147.08 mL) and reduction of bacterial population (Table 2). It has been reported the beneficial effects of sucrose in preservative solutions but in Rose it increased bacterial counting. For *Alstroemeria* cv. Fogo we use AgNPs of 15.79 nm diameter and 0.85 roundness (Fig. 3). We screened AgNps (0, 4, 8, 16, 32, 50, 66, 94, 132 mg L^{-1} NPsAg) to pulse solution but it did not increase vase life. Combination of pulse solution (50 mg L^{-1}) and vase solution (0.5 mg L^{-1} NPsAg) was tested: a) pulsing for 24 h, b) pulsing + preservative solution, c) spraying pulse solution, and d) control (water).). When NPsAg was added to the preservative solution, antimicrobial activity was observed but no positive effect on vase life. We arrived at the conclusion that the vase life response was related to the degree of ethylene sensitivity of each specie. *Alstroemeria*, is a flower reported as low/not sensitive to ethylene y contrast *Rosa hybrida* respond to AgNPs because most of the cultivars are high ethylene sensitive. *Chrysanthemum*, is reported as a medium ethylene sensitive flower. But in all cases bacteria contamination was controlled by the AgNPs, it is a very desirable effect for postharvest management and flower exportation.

REFERENCES

[1] Nakhjavani, M. et al. 2017. *Heat Mass Transfer.* (2017) (53):3201-3209. Doi:10.1007/s00231-017-2065-9
[2] Carrillo- López L.M. et al., *J. Nanomaterials*. (2016) (Doi:10.1155/2016/951750)
[3] Vicencio-Salas Solís C. et al., *Agrociencia* (2018) (52):951-965.

ACKNOWLEDGMENTS

The authors thank CONACyT for the Master and PhD scholarships of the second and third authors. We are grateful to Simon Morales for technical assistance at the Electron Microscopy Unit of the Postgraduate Collage of Agriculture (UME-CP).

FIGURES

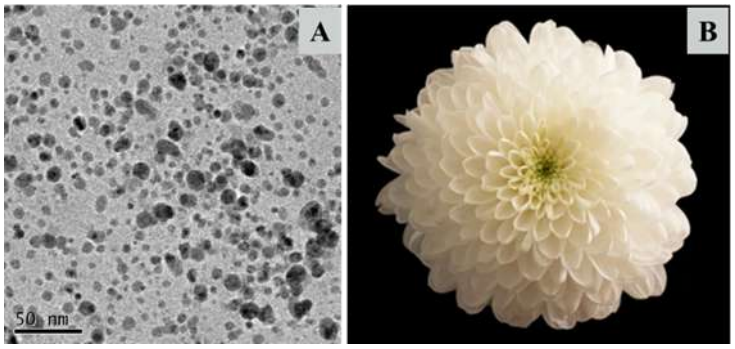

Figure. 1 Silver nanoparticles and plant material. A. Electron micrograph of AgNPs (10.2 ± 4.3 nm, 0.87 roundeness) synthesized with *C. abrosioides* extracts, TEM (Tecnai Spirit 2, Thermo Fisher) 100 keV and B. *Chrysanthemum* cv. Puma at harvest.

Table 1. Effect of Ag nanoparticle concentration (mM) on vase life (d), opening of *Chrysanthemum* inflorescences and bacterial inhibition in preservative solution.

AgNps (mM)	Vase life (d)	Diameter Inflorescences (cm)	Bacterial count (UCFmL^{-1})
control	12b	6.23c	105
0.01	21a	6.86b	2c
0.5	19.33a	6.96a	1c
0.10	19.33a	7.03a	0c
0.50	17.33b	6.16b	0c
1.0	17.00b	5.83b	0c
5.0	15.66b	6.16b	102c

Bacterial count is average of 5 experiments. Different letters in columns indicate statistical differences (Tuckey $p<0.05$)

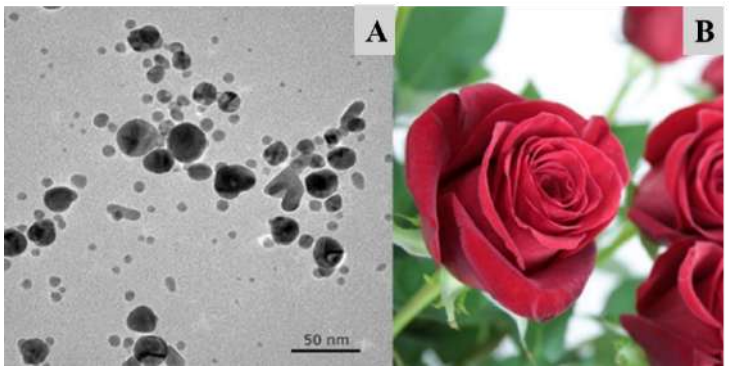

Figure. 2 Silver nanoparticles and plant material. A. Electron micrograph of AgNPs (21.50 nm, 0.86 roundness) synthesized with *C. sinensis* extracts, TEM (Tecnai Spirit 2, Thermo Fisher) 100 keV, B. *Rosa hybrid* cv. Fredom at harvest.

Table 2. Effect of AgNPs treatments on vase life, accumulated water consumption of *Rosa hybrida* cv. Fredom and bacterial count preservative solution (day 8).

AgNPs treatments	Vase life (d)	Water Consumption (mL)	Bacterial count (UCFmL^{-1})
Control	3.2c	96.8c	3.51a
NPs	5.4b	126.40b	2.36ab
NPs+S	3.9c	86.29d	2.91a
NPs+CA	7.5 a	147.08a	0.85a
NPs+CA+S	5.3 b	116.86b	1.26b

CA: 80 mgL^{-1}, Citric acid, S: 2% sucrose. Different letters in columns indicate significant differences (Tukey, $p<0.05$, n=15)

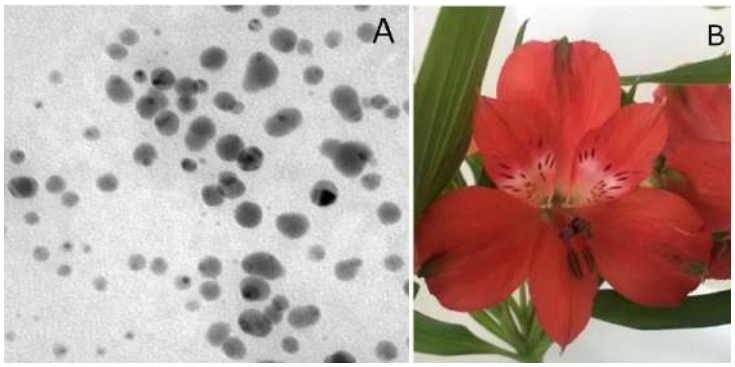

Figure. 2 Silver nanoparticles and plant material. A. Electron micrograph of AgNPs (15.79 nm, 0.85 roundness) synthesized with *C. sinensis* extracts, TEM (Tecnai Spirit 2, Thermo Fisher)100 keV, B. *Alstroemeria* cv. Fogo at harvest.

Table 3. Effect of AgNPs treatments on vase life, relative fresh weight (%) and Total chlorophyll (µg cm^{-2}) at final vase life of *Alsroemeria* cv. Fogo at harvest (day 21).

AgNPs Treatments (mgL^{-1})	Relative fresh weight (%)	Total Chl (µg cm^{-2})
Control	76.70	20.08
Pulse *	84.87	26.79
Pulse*+preservative**	85.96	25.09
Spraying *	86.48	13.39

(*) AgNPs 50 mgL^{-1}, (**) AgNPs 0.5 mg L^{-1}. No significant differences in columns (Tukey, $p<0.05$, n=15).

Acta Microscopica Vol. 32, Supp. 1, 2023
Abstract Book NSSY 2023- Galapagos 23 -29 April, 2023

RAMAN SPECTROSCOPY: INNOVATIVE SAMPLE SCANNING METHODS, ARTIFICIAL INTELLIGENCE CHEMOMETRICS, IMAGE MICROGEOPROCESSING AND COLOCALIZED MEASUREMENTS WITH SCANNING ELECTRON MICROSCOPY AND X-RAY MICROFLUORESCENCE.

Igor Carvalho (1), Filipe Cabral (1)
(1) Horiba Scientific Brazil, Jundiai – São Paulo, Brazil.
igor.carvalho@horiba.com

This presentation will focus on Raman and NanoRaman applied to the most diverse branches of knowledge. In this presentation you will learn the basic principles of Raman spectroscopy applied to Raman imaging. Applications and instrumentation will be the main topics for a wide range of materials characterization, including polymers, ceramics, biomaterials, life sciences and two-dimensional (2D) materials. Raman and Nanoraman microscopy is one of the only techniques capable of providing non-destructive, accurate analysis combined with high resolution images. Raman spectroscopy provides valuable information about the studied sample, such as chemical and structural composition. Based on the light-matter interaction, we obtain relevant information, such as: particle distribution, homogeneity, grain size, phase changes and several other characteristics of the sample through the chemical evaluation of the material. We will also discuss the combination of laser-excited photoluminescence imaging and Raman scattering of two-dimensional (2D) crystals to reveal the solid-state structure. The development of instrumentation makes possible the hyphenation of Raman with other techniques, such as Photoluminescence and AFM, being able to reach resolutions on a nanometric scale. The technique can be applied in several areas of knowledge, such as pharmaceuticals, photovoltaics, graphene, cells, nanoparticles, microplastics, among others.

Acta Microscopica Vol. 32, Supp. 1, 2023
Abstract Book NSSY 2023- Galapagos 23 -29 April, 2023

ANISOTROPIC VORTEX SQUEEZING AND SUPERCURRENT DIODE EFFECT IN NON-CENTROSYMMETRIC RASHBA SUPERCONDUCTORS

D. Kochan1,2

1 Institute for Theoretical Physics, University of Regensburg, 93040 Regensburg, Germany
2 Institute of Physics, Slovak Academy of Sciences, 84511 Bratislava, Slovakia
denis.kochan@ur.de

Most of 2D superconductors are of type II, i.e., they are penetrated by quantized vortices when exposed to out-of-plane magnetic fields. In the presence of a supercurrent, a Lorentz-like force acts on the vortices, leading to drift and dissipation. The current-induced vortex motion is impeded by pinning at defects. Usually, the pinning strength decreases upon any type of pair-breaking interaction that perturbs a system.
In the talk I will discuss surprising experimental evidence showing an unexpected enhancement of pinning in synthetic Rashba 2D superconductors when applying an in-plane magnetic field. When rotating the in-plane component of the field with respect to the driving current, the vortex inductance turns out to be highly anisotropic. We explain this phenomenon as a direct manifestation of Lifshitz invariant that is allowed in the Ginzburg-Landau free energy when space-inversion and time-reversal symmetries are broken. As demonstrated in our experiment [1], elliptic squeezing of vortices---an inherent property of the non-centrosymmetric superconducting condensate---provides an access to fundamentally new property of Rashba superconductors, and offers an entirely novel approach to vortex manipulation.
Another interesting feature of the non-centrosymmetric superconductors in the applied magnetic field is the supercurrent diode effect---the critical current in one direction exceeds its counterpart in the opposite one---what stems from the Cooper pairs with finite centre of mass momentum. In the pioneering experiment [2] we demonstrated the emergence of the supercurrent diode effect in the Josephson junctions based on synthetic Rashba superconductors made of Al-InAs quantum wells. In the talk, I will discuss a novel experimental method---measurements of the Josephson inductance---and the semiquantitative microscopic model capturing all the essential features as observed in the experiment.

REFERENCES

[1] L. Fuchs, D. Kochan, C. Baumgartner, S. Reinhardt, S. Gronin, G. Gardner, T. Lindemann, M. Manfra, C. Strunk, N. Paradiso; Physical Review X 12 (4), 041020 (2022).
[2] C. Baumgartner, L. Fuchs, A. Costa, S. Reinhardt, S. Gronin, G. Gardner, T. Lindemann, M. Manfra, P. Faria Junior, D. Kochan, J. Fabian, N. Paradiso, C. Strunk; Nature Nanotechnology 17 (1), 39 (2022).

FIGURES

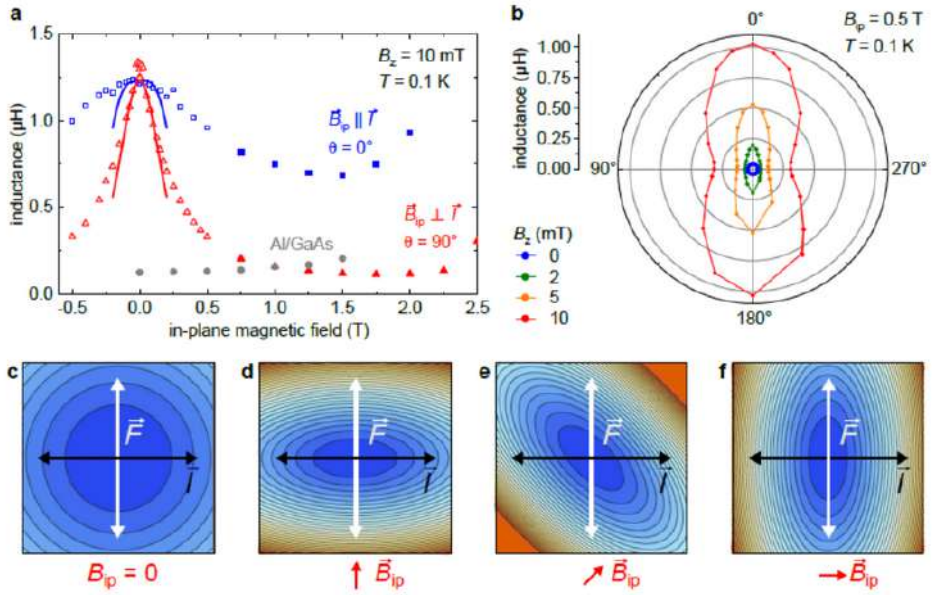

Figure 1. a, Sample inductance of Rashba superconductor as a function of in-plane magnetic field for different orientations of the driving current (red and blue symbols). The controlled measurement (grey symbols) corresponds to a centrosymmetric (i.e. non-Rashba) superconductor. b, Polar plot showing the angle dependence of the vortex inductance for selected values of out-of-plane magnetic field. c, The color plot schematically represents the modulus of the order parameter, |ψ (x,y)|2, near the core of a pinned vortex, in the absence of an in-plane field. The horizontal black arrow represents the direction of a current bias, while the white arrow indicates the direction at which a Lorentz force acts on a pinned vortex. The measured vortex inductance is rotation symmetric and inversely proportional to the curvature of |ψ (x,y)|2 along the force direction. d-f, When a finite in-plane field is applied the vortex core is squeezed as a consequence of the Rashba spin-orbit interaction, reflecting the measured change in vortex inductance. The curvature is always probed along the white axis, rotating the in-plane magnetic field the vortex rotates keeping its small elliptic axis parallel with the direction of the in-plane field. This allows one to extract from the vortex inductance the spatial profile –order parameter tomography--of |ψ (x,y)|2

.

FRIDAY

Theory and Simulations in Nanoscience

Acta Microscopica Vol. 32, Supp. 1, 2023
Abstract Book NSSY 2023- Galapagos 23 -29 April, 2023

SPINTERFACE EFFECTS IN ELECTRON TRANSPORT IN CHIRAL MOLECULAR JUNCTIONS

Vladimiro Mujica (1)

(1) Arizona State University, School of Molecular Sciences, Tempe, AZ 85287, U.S.A
vmujica@asu.edu

The term spinterface was coined in spintronics and refers to changes in the interfacial and surface electric and magnetic moments due to spin polarization effects. Spinterface has been proven to be an important element in understanding magnetoresistive effects in single molecule-junctions and it also plays an essential role in triggering the spin polarization response associated with the Chiral-Induced Spin Selectivity (CISS) effect. In this contribution, I will explore the fundamentals of spinterface and how it affects spin polarization and electron transport in chiral interfaces. I will specifically consider the case of a nano-junction consisting of two electrodes (one of them magnetic) and a chiral molecular bridge. The description of spin-polarized transport requires the explicit inclusion of spin-orbit interaction, and the breaking of space-inversion and time-reversal symmetries. The former is associated with chirality, whereas the latter requires the consideration of the molecule as an open system. Furthermore, the analysis of the experimental results in these single-molecule devices explicitly requires the inclusion of spinterface effects to account for the observed asymmetry in the conductance and spin polarization effects, which is the main objective of our study.

REFERENCES

[1] Clarice D. Aiello, John M. Abendroth, Muneer Abbas, Andrei Afanasev, Shivang Agarwal, Amartya S. Banerjee, David N. Beratan, Jason N. Belling, Bertrand Berche, Antia Botana, Justin R. Caram, Giuseppe Luca Celardo, Gianaurelio Cuniberti, Aitzol Garcia-Etxarri, Arezoo Dianat, Ismael Diez-Perez, Yuqi Guo, Rafael Gutierrez, Carmen Herrmann, Joshua Hihath, Suneet Kale, Philip Kurian, Ying-Cheng Lai, Tianhan Liu, Alexander Lopez, Ernesto Medina, Vladimiro Mujica, Ron Naaman, Mohammadreza Noormandipour, Julio L. Palma, Yossi Paltiel, William Petuskey, João Carlos Ribeiro-Silva, Juan José Saenz, Elton J. G. Santos, Maria Solyanik-Gorgone, Volker J. Sorger, Dominik M. Stemer, Jesus M. Ugalde, Ana Valdes-Curiel, Solmar Varela, David H. Waldeck, Michael R. Wasielewski, Paul S. Weiss, Helmut Zacharias, and Qing Hua Wang. A Chirality-Based Quantum Leap, ACS Nano 2022 16 (4), 4989-5035 DOI: 10.1021/acsnano.1c01347

[2] Albert C Aragonès, Ernesto Medina, Miriam Ferrer‐Huerta, Nuria Gimeno, Meritxell Teixidó, Julio L Palma, Nongjian Tao, Jesus M Ugalde, Ernest Giralt, Ismael Díez‐Pérez, Vladimiro Mujica
"Measuring the Spin Polarization Power of a Single Chiral Molecule", Small 13(2017)1602519.

[3] Aragonès AC, Aravena D, Ugalde JM, Medina E, Gutierrez R, Ruiz E, Mujica V, Díez-Pérez I. Magnetoresistive single-molecule junctions: The role of the spinterface and the CISS effect. Isr J Chem [Internet]. 2022;62(11-12)

ACKNOWLEDGMENTS

V.M acknowledges the support of the W. M. Keck Foundation through the grant **Chirality, Spin Coherence and Entanglement in Quantum Biology.**

Acta Microscopica Vol. 32, Supp. 1, 2023
Abstract Book NSSY 2023- Galapagos 23 -29 April, 2023

CHIRALLY INDUCED SPIN SELECTIVITY: POLARIZATION FROM DECOHERENCE

Ernesto Medina (1), Solmar Varela (2), Mayra Peralta (4) Bertrand Berche (5), Vladimiro Mujica

(1)Departamento de Física, Universidad San Francisco de Quito, Quito, Ecuador (2) Institute of Materials Science and Nanotechnology, TU Dresden, Germany (3) School of Molecular Sciences, Tempe, Arizona, USA (4) Institute for Material Science, TU Dresden, Germany (5) Laboratoire de Physique et Chimie Theorique, University of Lorraine, Nancy, France.
emedina@usfq.edu.ec

Chirally induced spin selectivity (CISS) has been an intriguing topic of research for almost two decades now and in spite of all the astonishing. experimental manifestations and applications, it has still not completely yielded a complete theory. The experimental evidence of a strong spin selective effect in mostly organic molecules such as individual DNA, Oligopeptides, Proteins, amino acids, helicene, Photosystem I[1], and carbon nanotubes, among many other point chiral and helical structures or chirally connected structures[2]. Two major experimental setups are generally realized: i) Photoelectrons transiting through chiral self-assembled monolayers (SAMS) spin-polarized perpendicular to the SAM surface and ii) STM-Junctions, where electrons transit a single molecule, and spin is injected into a metal or a ferromagnet. In both setups, astonishing polarizations of up to 60%[3,4] are observed, superior to those that can be produced by ferromagnets, albeit in different time scales. In this work, we briefly discuss our group's contributions that have become permanent building blocks in understanding the CISS effect and some of the questions that linger in the problem. We will restrict our discussion to the STM-junction measurements, which most clearly define a single-molecule effect and the transport configuration as a two-terminal problem. In the first theoretical models, the spin-orbit coupling (SOC was surmised to be the spin-active ingredient since no sources of exchange interactions could reasonably be identified in the organic molecules in which the effect is observed. Nevertheless, the source of the coupling was a mystery since the effect's large size seems to require a large SOC in the eV range. We identified early on that this would entail huge electric fields that are not found in the physical system, not even in the atomic nuclei, which result in the well-known relativistic corrections to the atomic spectrum. It was settled going forward that the intrinsic SO coupling of the atoms involved is in the units to tens of meV range at most. In most tight-binding models, this produced only very small transport polarizations, although much larger than those of classical gas phase experiments for point chiral molecules. A very elegant way to see the material sources of the SOC is by thinking of long molecules as quasi-one-dimensional solids and using the k.p argument in a Hamiltonian that includes SOC.

Taking into account the electron filling of the mobile electron orbitals and using the wave functions of that filling as a basis, one can show that the SOC comes from the electric fields of the atomic nuclei, and the momenta involved are those of the electron clouds of the molecular component atoms where the SOC enters

$$\Delta_{\cdot\,\cdot\,\cdot\,\cdot} = (\hbar^2/4m_0^2c^2)\langle n'\sigma'|\mathbf{p}\cdot\sigma\times(\nabla V_0)|n\sigma\rangle,$$

showing the relevant momenta and field.

$$\sum_{n,\sigma}\left\{\left[E_n(\mathbf{0})+\frac{\hbar^2k^2}{2m_0}\right]\delta_{nn'}\delta_{\sigma\sigma'}+\frac{\hbar}{m_0}\mathbf{k}\cdot\mathbf{P}_{nn'\sigma\sigma'}+\langle\langle V(r)\rangle\rangle+\Delta_{nn'\sigma\sigma'}\right\}c_{\nu n\sigma}(\mathbf{k})=E_\nu(\mathbf{k})|c_{\nu n'\sigma'}(\mathbf{k})\rangle$$

gradients are those expected from the local orbitals while referring only to kinetic quantities[5].

Another challenge to theories was related to the two terminal setups and measurement of spin polarization. The work of van Wees et al [6] reminded the community that time reversal symmetric coupling could not polarize spin by itself in two terminal measurements (see also [2]). This is a consequence of the Onsager relations applicable to the linear regime. A natural source of time-reversal symmetry breaking (TRSB) is a third probe that can couple to the electron transport. This can occur via electron-phonon interactions where

phonons have a thermal distribution [7] or via a third probe that at least scrambles the phase information of the electrons while preserving unitarity. Also a major problem of previous theoretical models is the assumption of metallic-like transport that does not occur in molecular transport. We addressed both shortcomings in a quasi-one-dimensional Rashba model tunneling under a spin active barrier coupled to a third probe. The model is unitary but includes dephasing effects due to an electron reservoir implemented through a Buttiker probe[8]. As expected, the model does not yield net polarization in the two-terminal setup but yields strong polarizations for meV SO coupling (See Figure 1). The scenario for this effect is that tunneling exponentially enhances the dephasing effects of the third probe in the Safeway a magnetic field under the barrier would work. We believe this model is amenable to coupling to either electron-phonon or electron-electron interactions in contact with a thermal reservoir and would explain spin polarization in the linear regime.

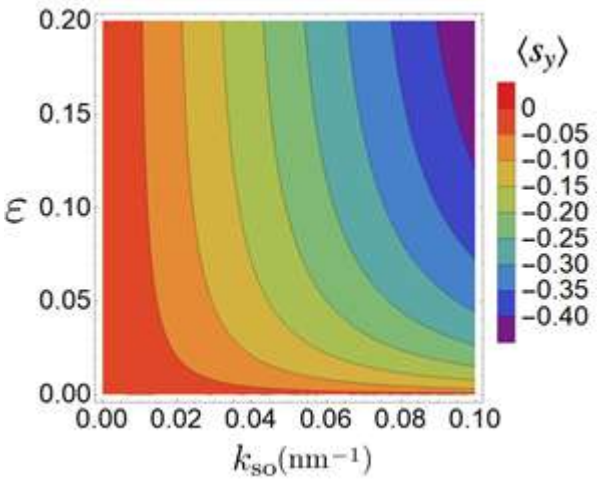

Figure 1: Polarization produced by a decoherence probe (controlled by) coupled to tunneling in a SO active barrier. The color shades represent the generated y component of the spin induced by time reversal symmetry breaking as a function of the spin-orbit strength . A large spin polarization is achieved by the atomic SOC exponentiated by tunneling

Another challenge to theories was related to the two terminal setups and measurement of spin polarization. The work of van Wees et al [6] reminded the community that time reversal symmetric coupling could not polarize spin by itself in two terminal measurements (see also [2]). This is a consequence of the Onsager relations applicable to the linear regime. A natural source of time-reversal symmetry breaking (TRSB) is a third probe that can couple to the electron transport. This can occur via electron-phonon interactions where phonons have a thermal distribution [7] or via a third probe that at least scrambles the phase information of the electrons while preserving unitarity. Also a major problem of previous theoretical models is the assumption of metallic-like transport that does not occur in molecular transport. We addressed both shortcomings in a quasi-one-dimensional Rashba model tunneling under a spin active barrier coupled to a third probe. The model is unitary but includes dephasing effects due to an electron reservoir implemented through a Buttiker probe[8]. As expected, the model does not yield net polarization in the two-terminal setup but yields strong polarizations for meV SO coupling (See Figure 1). The scenario for this effect is that tunneling exponentially enhances the dephasing effects of the third probe in the Safeway a magnetic field under the barrier would work. We believe this model is amenable to coupling to either electron-phonon or electron-electron interactions in contact with a thermal reservoir and would explain spin polarization in the linear regime.

REFERENCES

[1] Naaman R, Waldeck D. H. Annu. Rev. Phys. Chem. (2015)(66)(263).
[2] Guo A.-M Phys. Rev. B (2016)(94)(165409).
[3] Gohler B. et al Science (2011)(331)(894).
[4] Xie Z. et al Nano Lett. (2011)(11)(4652).
[5] Winkler R. (2003) *Spin-Orbit Coupling Effects in Two Dimensional Electron and Hole Systems,* Berlin Springer-Verlag.
[6] Yang X. et al Nano Lett. (2020) (20), (6148).
[7] Fransson J. Phys. Rev. B (2020)(102)(235416).
[8] Varela S. et al Arxiv: 2301.02156 (2023).

ACKNOWLEDGMENTS

EM thanks POLI grant POLI 014EM of USFQ for funding and visiting Professorships to the University of Lorraine.

Acta Microscopica Vol. 32, Supp. 1, 2023
Abstract Book NSSY 2023- Galapagos 23 -29 April, 2023

AB INITIO STUDIES OF BULK AND (001) SURFACES OF THE METAL HALIDE DOUBLE PEROVSKITE $CS_2AU_2CL_6$

Anthony Vizcaino (1), Henry Pinto (2)

(1) CompNano Group, School of Physical Sciences and Nanotechnology, Yachay Tech University, Urcuqui 100119, Ecuador. (2) CompNano Group, School of Physical Sciences and Nanotechnology, Yachay Tech University, Urcuqui 100119, Ecuador.
anthony.vizcaino@hotmail.com

Perovskites are materials that have gained particular importance in recent years due to their application in the electronics industry, such as semiconductors and piezoelectrics. Furthermore, many materials can be considered perovskites if they have an atomic structure defined by $A_2B_2X_6$. Among all these possibilities, we present the study of $Cs_2Au_2Cl_6$ metal halide double perovskites, which use elements that do not harm the environment and do not produce as much damage as before (lead), aligning our research with the UN sustainable development goals: climate action and affordable, clean energy. This work builds on a previous study of the Integrated experimental and theoretical approach for the efficient design and synthesis of gold-based double-halide perovskites. However, it is considered relevant to deepen the study of this compound to establish a state-of-the-art that complements the previous analyses. We perform Density Functional Theory (DFT) surface calculations using the SCAN functional (Strongly Constrained and Appropriately Normed), 4-layer slab model and vacuum of 15 Å; to determine the electronic properties. We analyzed all the atomic models that this material could have; one terminated in gold and chlorine (model A), the other terminated in chlorine and cesium and chlorine (model B), and we also created models with point defect vacancies by removing chlorine atoms from the surface and subsurface with the objective of manipulate the band gap. The most stable model $Cs_2Au_2Cl_6$ is the surface B, which was determined using the energy of the system, with a difference in energy of 0.10 eV from surface A. We calculated the partial density of states (PDOS), and the results suggest that on the surface, the valence band has contributions of gold and chlorine, which correspond mainly to the Au-d, Cl-p states, and a lesser extent, the cesium contribution belongs to Cs-p states. Meanwhile, the conduction band has gold, chlorine, and cesium contributions with Au-s, Au-d, Cl-p, and Cs-d states. Of all the models presented, only the l4a-2clv, l4b-2clv2B, and l4a are insulators; all other atomic models show metallic behavior in their outermost layer. In addition, we simulated Scanning Tunneling Microscope (STM) images showing that the surface atoms in model A correspond to gold and in model B correspond to chlorine. We also computed Ultraviolet Photoelectron Spectroscopy (UPS) images, and in all models studied, there is a significant contribution from gold and chlorine atoms and a small contribution from cesium. Additionally, the formation of energy vacancies was calculated from where the models (l4b-clvB) and (l4a-clv) are the ones that require less energy to be produced. Finally, we calculate the work function for all the models, (l4a-sclvB) and (l4b-2clv2A), which require less energy. Further DFT work could be done using bromine (Br) or iodine (I) elements instead of chlorine to determine which gold-based double-halide perovskites exhibit the best electronic and mechanical properties.

REFERENCES

[1] Bajorowicz, B.; Mikolajczyk, A.; Pinto, H. P.; Miodynska, M.; Lisowski, W.; Klimczuk, T.; Kaplan-Ashiri, I.; Kazes, M.; Oron, D.; Zaleska-Medynska, A. Integrated experimental and theoretical approach for efficient design and synthesis of gold-based double halide perovskites. The Journal of Physical Chemistry C 2020, 124, 26769–26779

[2] Giustino, F. Materials modelling using density functional theory: properties and predictions; Oxford University Press, 2014

[3] Freysoldt, C.; Grabowski, B.; Hickel, T.; Neugebauer, J.; Kresse, G.; Janotti, A.; Van de Walle, C. G. First-principles calculations for point defects in solids. Reviews of modern physics 2014, 86, 253

ACKNOWLEDGMENTS

My sincere gratitude to my tutor Henry Pinto for being my guide, teacher, and friend during my time at Yachay Tech.

FIGURES

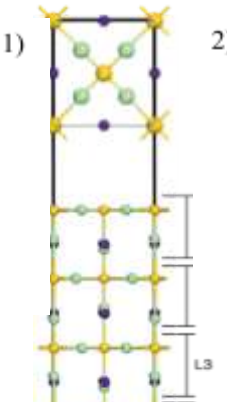

Fig 1. Atomic structure model A

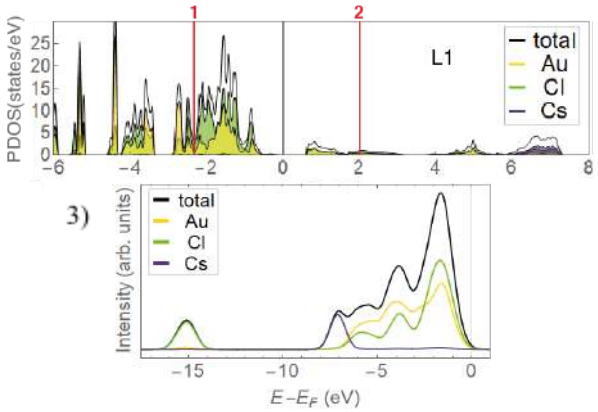

Fig 3. UPS of the surface

SURFACE MODEL A

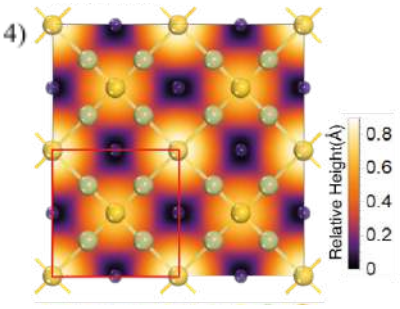

Fig 4. STM and relative height using V_{bias} = -1.10 V

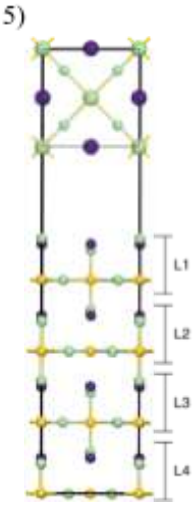

Fig 5. Atomic structure model B

SURFACE MODEL B

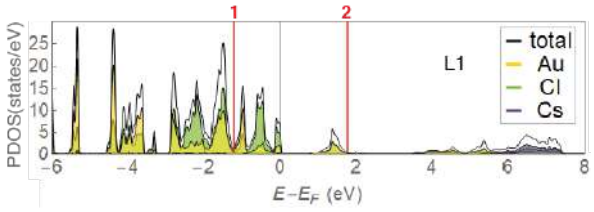

Fig 6. PDOS of the outermost layer

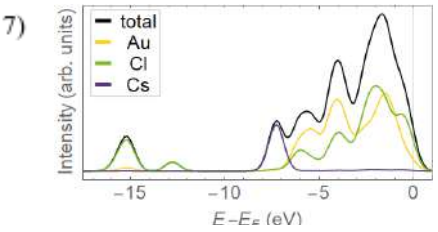

Fig 7. UPS of the surface

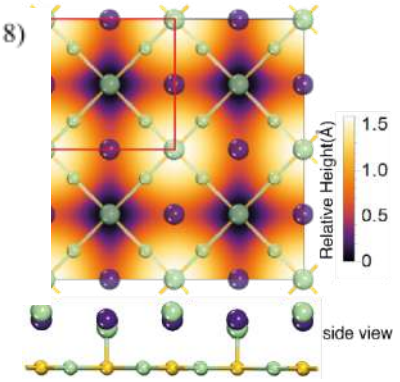

Fig 8. STM and relative height using V_{bias} = -0.85 V

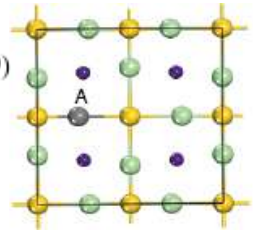

Fig 9. A vacancy for Surface A

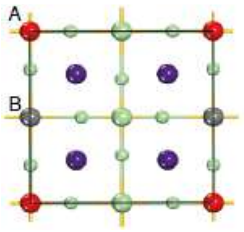

Fig 10. A and B vacancies for Surface B

Table 1. Results summary. Vacancy type, behavior, work function (ϕ), and energy vacancy formation.

Vacancy Type	Behaviour	ϕ (eV)	Energy Formation(eV)
l4a-clv	metallic	6.31	16.26
l4a-2clv	insulator	6.74	24.83
l4a-sclvA	metallic	6.96	16.39
l4a-sclvB	metallic	6.28	17.88
l4b-clvA	metallic	4.68	18.29
l4b-clvB	metallic	3.54	17.20
l4b-2clv2A	metallic	2.31	35.33
l4b-2clv2B	insulator	3.89	34.62

Acta Microscopica Vol. 32, Supp. 1, 2023
Abstract Book NSSY 2023- Galapagos 23 -29 April, 2023

COLLECTIVE VIBRATIONS IN HOMOGENEOUS CARBON NANOTUBE BUNDLES

Charlotte Berrezueta-Palacios(1), Dekel Nakar(2), Anna Wroblewska(3), Oisín Garrity(1), Han Li(4), Benjamin Scott Flavel(4), Ernesto Joselevich(2), Stephanie Reich(1) and Georgy Gordeev(1, 5)
(1) Department of Physics, Freie Universität Berlin, Berlin 14195,Germany. (2) Department of Materials and Interfaces, Weizmann Institute of Science, Rehovot 7610001, Israel. (3) Faculty of Physics, Warsaw University of Technology,

Koszykowa 75, 00-662, Warsaw, Poland. (4) Institute of Nanotechnology, Karlsruhe Institute of TechnologyHermann-von-Helmholtz-Platz 1, 76344 Eggenstein-Leopoldshafen, Germany. (5) Department of Physics and Materials Science, University of Luxembourg, L-4422 Belvaux, Luxembourg.
charlotte.berrezueta@fu-berlin.de

Carbon nanotubes (CNTs) are tiny hollow cylinders made of carbon. Raman spectroscopy is one of the most widespread techniques for the analysis of CNT, as it can identify their microscopic structure. In particular, much attention is paid to the low frequency region where the radial breathing mode (RBM) peak is observed. Because of their curved structure, RBM peak arises as a unique spectral feature from CNTs it describes the breathing-like behavior originating from the symmetric vibration in a radial direction with respect to the tube axis. For isolated tubes, a single peak is observed with a frequency that is inversely proportional to the tube's diameter. The physical properties of individual CNTs differ from the CNT bundles, aggregated CNT form and are regulated by its chiral purity and degree of bundling. The higher-dimensional arrangement of nanomaterials materials can influence their vibrational modes. When identical CNTs get arranged into Two-dimensional hexagonal lattices, their vibrational properties were predicted to change and additional low-frequency modes were expected in the Raman spectrum arising from collective vibrations [1]. However, the experimental study of collective vibrations has been limited due to the difficulty in obtaining homogeneous chirality bundles. To observe these collective vibrational features, one must measure high-quality single chirality bundles which are still a current challenge in synthesis processes. There are two approaches that can create homogeneous aggregations of nanotubes: a solution based on a CNT solution vacuum filtration and direct coiling during CVD growth. Both approaches in principle can yield extremely pure material. Here, we present a Raman study of the collective vibrational modes arising from homogeneous bundles formed by a SWCNT coil and a homogeneous carbon nanotube film. Through a self-coiling mechanism, carbon nanotubes can be arranged into coils after grown during their synthesis process and comprise perfectly aligned homologous bundles with a radial shape. By characterizing and comparing the physical properties of the coil with respect to its ends, the bundling effects can be isolated and studied[2,3]. In such structures we observe two breathing-like modes RBM(B1) and RBM(B2) in contrast to the single radial breathing mode characteristic for isolated tubes. We investigate the exciton-phonon coupling for these modes with resonant Raman spectroscopy finding the same resonance energy for both BM peaks and confirming that both modes originate from the same chirality bundle. Additionally, we study the tube's diameter dependence of vibrational coupling by analyzing different tube's diameter coils and film samples. We compare our experimental findings with theoretical lattice-dynamical study of infinite bundles of identical tubes accomplished within a valence force field (VVF) model with intertube interactions described by a Lennard Jones potential. These results provide an insight into intra-tube lattice dynamics in carbon nanotubes bundles for better understanding of collective vibrational effects.

REFERENCES

[1] Popov, V.N.et al. Physical Review B, (2001) 63(23), p.233407.
[2] Shadmi, N. et al. 2016, 16(4), pp.2152-2158.
[3] Nakar, Det et al. 2019. Nano Letters, 20(2), pp.953-962.

FIGURES

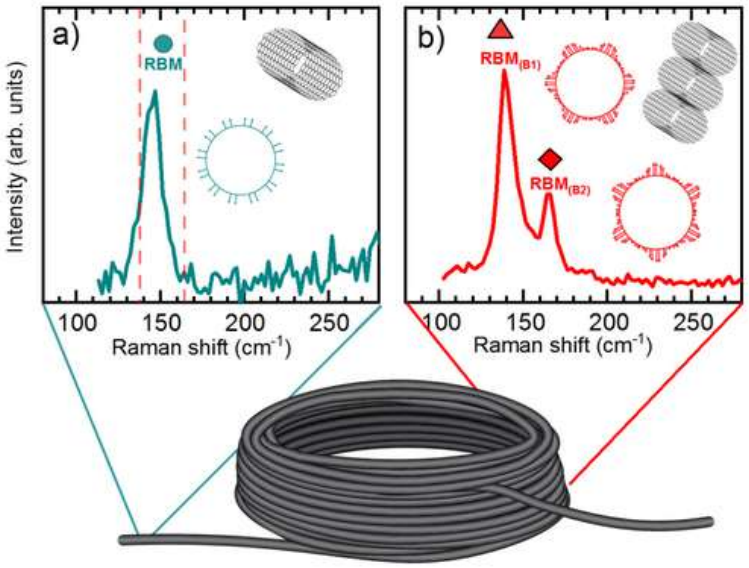

Figure1. Raman spectroscopy of the Radial breathing modes of carbon nanotube coil. a) Raman spectra for tail and b) coil (isolated vs bundles effects). The peaks originating from collective vibrations are observed by RBM(B1) and RBM(B2).

Acta Microscopica Vol. 32, Supp. 1, 2023
Abstract Book NSSY 2023- Galapagos 23 -29 April, 2023

TUESDAY

Poster Session 1

SYNTHESIS OF A CAFFEINE/POLY (VYNIL ALCOHOL) POLYMER WITH UV-SHIELDING PROPERTIES

José Trujillo (1), Luis Corredor (1), Julio C. Chacón-Torres (1*)

(1) School of Physical Sciences and Nanotechnology, Yachay Tech University, 100119 Urcuquí, Ecuador.
Email: jose.trujillo@yachaytech.edu.ec

UV-radiation covers a wavelength range from 100 to 400 nm and is divided into three bands: UVA (320-400 nm), UVB (280-320 nm), and UVC (100-280 nm) [1]. Such radiation is one of the principal factors that causes degradation and performance reduction of polymer-related products [1]. Polymers and their composites offer promising suitable alternatives in the field of radiation shielding due to its lightweight, durability, flexibility along with superior physical, mechanical, optical, and radiation resistance properties [2, 3]. Poly (vinyl alcohol) (PVA) is a prominent material as a UV-shield, in addition it has nontoxic and biocompatible properties, a good tensile strength, flexibility, hardness, enhanced chemical resistance and aroma barrier characteristics [2]. However, at wet conditions, such properties are diminished because of the plasticizing action of water molecules [2]. On the other hand, special attention should be taken to caffeine (an organic methyl xanthine molecule derived from coffee), whose absorption peak locates at 272 nm [1]. In general, it has been showed that PVA properties are enhanced when this polymer is doped or functionalized [1, 2] enhancing its, UV- and thermal-oxidative stability without a significant loss of transparency, due to a higher crystallinity of the polymeric composite (nucleation effect) [1]. Thus, in this work a transparent caffeine/PVA composite was developed aiming for advanced UV-protective characteristics. Caffeine was extracted from coffee by refluxing 50 grams of coffee into 200 ml of hot water. The solution was vacuum filtered while it was still hot. An organic phase was obtained *via* liquid-liquid extraction with chloroform, and then dried with magnesium sulphate. Finally, caffeine was sublimated (recrystallized) by using a crystallizing dish. In parallel, a 5% (w/w) PVA solution was made. A composite of caffeine/PVA was synthesized into an Eppendorf tube, by using a vortex mixer. After obtaining a homogenous solution, the composite was spin coated on a SiO_2 wafer obtaining films of caffeine/PVA at different %w/w concentrations: 0, 0.25, 0.50, 1.00, 1.25, 1.50, 5.00, and 6.00. The optical absorption of right radiation was tested by UV-vis spectroscopy in a range from 250 nm to 500 nm. As observed in Figure 1a), the best absorption was obtained at 1.00% caffeine concentration with a peak at about 280 nm associated to the C=O group in caffeine [1]. On the other hand, films at 5% and 6% caffeine concentration showed similar absorbance ability but they were very brittle. It is important to mention that caffeine doping of the films actually gave them a protective property against ultraviolet rays since a pure PVA film does not absorb any of the light at the analyzed wavelength range, as observed in the yellow line of Figure 1a). In Figure 1b), pure commercial caffeine was compared to our extracted caffeine within 1% caffeine/PVA films revealing increased conjugation of the chromophore in the pure caffeine composite. Furthermore, the maximum absorbance of the extracted caffeine film was decreased by approximately 0.3 units which is good enough compared to its pure counterpart. Since all UVC and some UVB rays are absorbed in the ozone Earth's layer, the most damaging natural UV radiation is in between 290 and 350 nm (towards UVA zone) [1]. The polymer shows absorption in a good range into the damaging range of UV natural light. The development of this advanced polymeric composite is of high importance to Ecuador because of the extreme UV indices at the equatorial region, specially at the highlands (Andean zone) where the ozone layer is thinner. This PVA composite could provide a suitable base for a sunscreen due to biocompatibility, be used in fibers for UV-filtering clothes, create a proper coverage in food packaging, even this material could be used for UV coating technological purposes as a safer and more efficient alternative for corrosion resistance in many important industrial markets within the country.

REFERENCES

[1] Y. Lyu, X. Gu, and Y. Mao. *Industrial & Engineering Chemistry Research* (2020) (59) (8640).
[2] Aslam, M.; Kalyar, M. A.; Raza, Z. A. *Polymer Engineering & Science* (2018) (58) (2119–2132).
[3] Tuttle, M. E. (2003) *Structural Analysis of Polymeric Composite Materials*; New York, Crc Press, pp. 1-14.

ACKNOWLEDGMENTS

We thank the support of the laboratory technician Zaillmar Morales at Yachay Tech's Laboratories from the School of Chemical Sciences and Engineering.

FIGURES

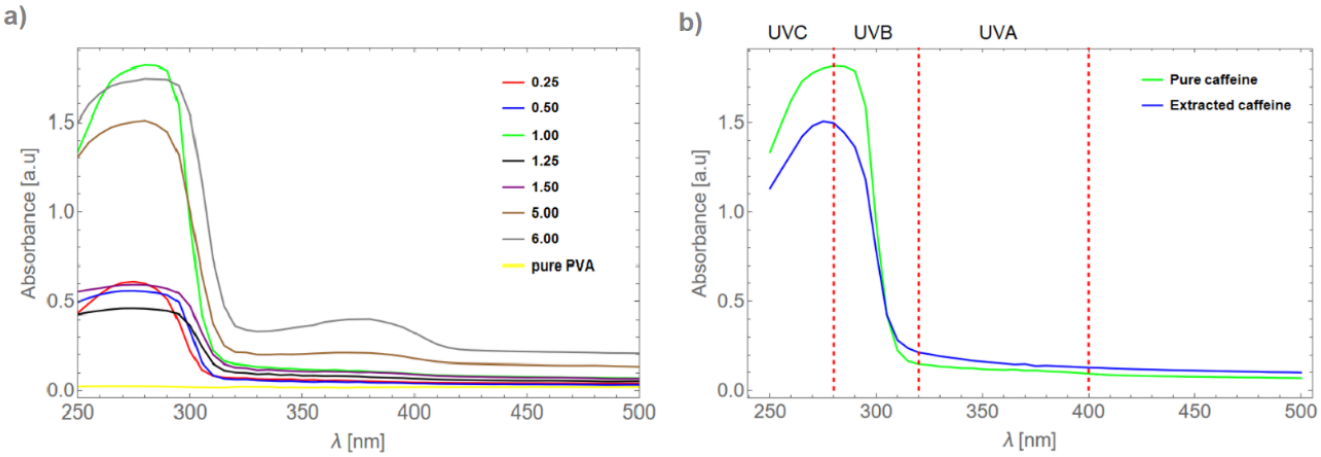

Figure 1. UV-VIS spectra of PVA films a) at different % w/w pure-caffeine concentrations, and b) doped with pure-caffeine vs. extracted-caffeine at 1% concentration.

Acta Microscopica Vol. 32, Supp. 1, 2023
Abstract Book NSSY 2023- Galapagos 23 -29 April, 2023

INACTIVATION OF POTENTIALLY TOXIC CYANOBACTERIA BY PHOTOCATALYTIC BISMUTH OXYIODIDE MICROSPHERES

Virginia del Carmen Rivadeneira (1), Michael Zuarez-Chamba (1), Miguel Quishpe (1), Miguel Herrera Robledo (1)

(1) Ikiam Amazon Regional University, Tena-Napo, Ecuador.
Email: virginia.rivadeneira@est.ikiam.edu.ec

The progressive deterioration of surface waters has been observed for many years. Toxic cyanobacterial blooms have become commonplace in water bodies around the world as a result of eutrophication and climate change, posing a serious threat to tourism or fisheries[2]. Cyanobacteria are gram-negative bacteria that are common members of the freshwater phytoplankton community. Their presence in drinking water is therefore of concern because of their ability to produce toxins that can impair water quality[3]. Cyanobacteria of the genus *Microcystis* sp. are the major producers of cyanotoxins such as microcystin-LR (MC-LR). In order to remove this type of cyanobacteria, physical, chemical and microbial technologies have been developed and applied[2]. However, these technologies, although promising, have limitations[2]. In this regard, heterogeneous photocatalysis has emerged as a potential alternative tool due to its ability to take advantage of solar radiation to inactivate pathogenic microorganisms present in wastewater treatment plant (WWTP) effluents. The visible light responsive three dimensional hierarchical bismuth oxyiodide microsphere architecture can be attributed to more efficient charge separation, small particle size, high specific surface area and suitable energy band structure[2]. Therefore, the aim of the present work is to evaluate the effectiveness of BiOI and $Bi_4O_5I_2$ microspheres in the inactivation of potentially toxic cyanobacteria under visible light. To achieve this objective, first, a 1 liter water sample was taken at the Ikiam WWTP. Next, a particular cyanobacterium was isolated with BG-11 selective medium using the streak depletion technique. Once the strain was considered pure, it was massaged in flasks containing BG-11 liquid medium using a constant aeration pump and 16:8 light/dark photoperiod. Then, gram staining was performed to morphologically identify the type of cyanobacteria under an optical microscope. However, because the morphology of the microalga *Chlorella vulgaris* is similar to Microcystis aeruginosa, a molecular analysis of the prepared stock was performed to rule out whether or not the presence of this microalga. The molecular analysis was done by PCR and electrophoresis and the 16S gene was used as reference. In addition, amplification of the mcyA gene was performed in order to identify whether cyanobacteria produce cyanotoxins. Finally, photocatalytic evaluations were performed using 50 mg of BiOI and $Bi_4O_5I_2$ microspheres, and 100 ml of cyanobacteria culture with an initial concentration of 100 µg/L. The solution was left for 1 hour in dark and then irradiated with white LED light (400W) for 10 hours. Aliquots were taken at 1 hour intervals to count live cells and extract chlorophyll a, which are indicators of cyanobacterial inactivation. Staining results indicate that the isolated cyanobacteria are gram negative. On the other hand, molecular analysis showed that there is no presence of microalgae and that the cyanobacteria that are present express the mcyA gene. The latter means that the cyanobacteria are capable of producing a variant of the cyanotoxin microcystin. Photocatalysis tests showed that the BiOI and $Bi_4O_5I_2$ photocatalysts can efficiently inactivate the cyanobacteria. With the BiOI photocatalyst after 11 hours, a 92.97% decrease of chlorophyll a was obtained. While with the $Bi_4O_5I_2$ photocatalyst it was 95.49%. In conclusion, the inactivation of potentially toxic cyanobacteria with BiOI microspheres was favorable; however, $Bi_4O_5I_2$ proved to be efficient with 3% more inactivation in the same time, without a significant difference between both processes, which makes it promising for the process of inactivating cyanobacteria in aquatic ecosystems.

REFERENCES

[1] Harke MJ, Steffen MM, Gobler CJ, Otten TG, Wilhelm SW, Wood SA, et al. A review of the global ecology, genomics, and biogeography of the toxic cyanobacterium, Microcystis spp. Harmful Algae. 2016;54: 4–20. doi:10.1016/j.hal.2015.12.007.

[2] He X, Wu P, Wang S, Wang A, Wang C, Ding P. Inactivation of harmful algae using photocatalysts: Mechanisms and performance. Journal of Cleaner Production. Elsevier Ltd; 2021. doi:10.1016/j.jclepro.2020.125755. [3] Xu Y, Yang J, Ou M, Wang Y, Jia J. Study of Microcystis aeruginosa inhibition by electrochemical method. Biochemical Engineering Journal. 2007;36: 215–220. doi:10.1016/j.bej.2007.02.022.

ACKNOWLEDGMENTS

To the laboratories of the Universidad Regional Amazónica Ikiam, to the Corporación Ecuatoriana para el Desarrollo de la Investigación y la Academia (CEDIA) through the CEPRA XVI-2022-21 DEGRADACIÓN CONTAMINANTES project and to the Erasmus + CBHE program through the NB LAB project (Contract number: 619346-EPP-1-2020-1-DE-EPPKA2- CBHE-JP).

FIGURES

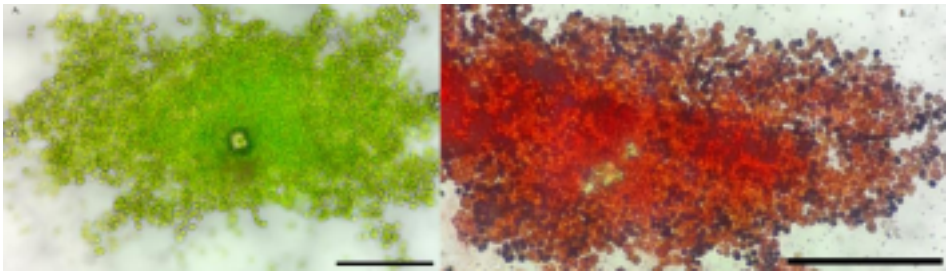

Figure 1. Micrographs of *Microcystis* sp. under light microscope. A. Without gram staining; B. With gram staining. Scale bar = 80 µm

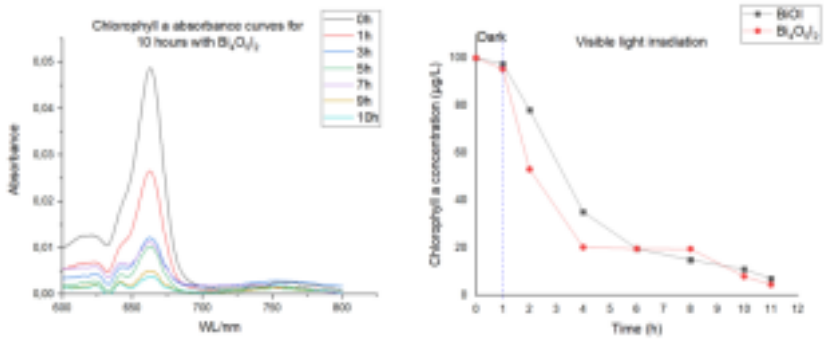

Figure 2. Plots of the inactivation of potentially toxic cyanobacteria for 11 hours. A. Absorbance curves of chlorophyll a with $Bi_4O_5I_2$; B. Decrease in chlorophyll concentration with BiOI and $Bi_4O_5I_2$.

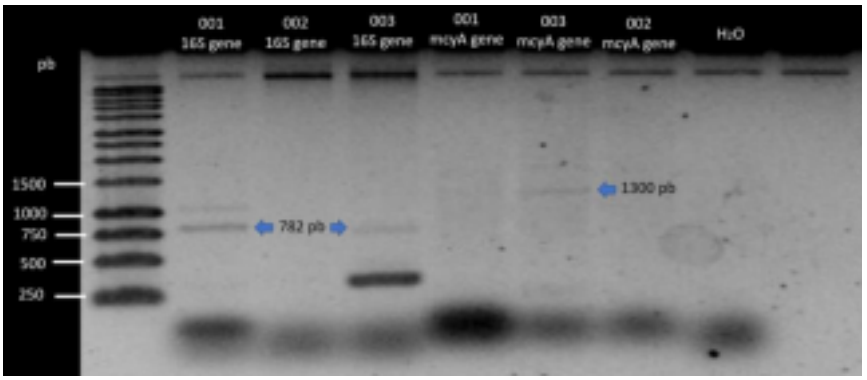

Figure 3. Photographic record of an electrophoresis run of the different PCR products, using the primers 27F/809R of the 16S gene, to obtain 782bp fragments, and the MSF/MSR primers of the microcystin synthetase gene (mcyA) to obtain 1300bp fragments in the potentially toxic cyanobacterial samples.

Acta Microscopica Vol. 32, Supp. 1, 2023
Abstract Book NSSY 2023- Galapagos 23 -29 April, 2023

PRELIMINARY RESULTS ON THE USE OF *PERSEA AMERICANA* EXTRACTS AS A BIORESOURCE FOR THE PRODUCTION OF SILVER NANOPARTICLES

Bryan Vargas (1), Raúl Dávalos (1), Jonathan Escorza (2).

(1) School of Biological Sciences and Engineering, Yachay Tech University, Hacienda San José s/n, San Miguel de Urcuquí 100119, Ecuador. (2) School of Physical Sciences and Engineering, Yachay Tech University, Hacienda San José s/n, San Miguel de Urcuquí 100119, Ecuador.
bryan.vargasp@yachaytech.edu.ec

Bio-nanotechnology constitutes a novel methodology that enables the production of different types of nanomaterials by making use of natural bioresources, namely bacteria, algae, fungi, plant extracts, single biomolecules or even viruses. Unlike chemical or physical routes, biosynthesis produces nanomaterials with improved biocompatibility, a key-advantage for their application in the biomedical field. Besides the interesting properties that biosynthesized nanomaterials display, this methodology is environmentally friendly (avoids the use of toxic reagents or the generation of toxic byproducts) and offers low production costs. Metallic nanoparticles can be synthesized through this methodology, and are of special interest for material scientists due to their wide variety of applications. Silver nanoparticles (AgNPs), for example, possess interesting optical, electrical, thermal and biological properties, which allows them to be used in the biomedical field. For this reason, it results of special interest to study the biosynthesis of silver nanoparticles by using natural resources that we have available. The aim of this work is to evaluate the use of plant extracts from food waste as bioagents for the production of silver nanoparticles with suitable properties for biomedical applications. Here, we have used different extracts of *Persea americana* (avocado) seeds, a vegetal material with no-known use and considered as waste in the Ecuadorian food industry, for the green synthesis of silver nanoparticles. The extracts were prepared using three different solvents including ethanol, acidified methanol and water, and characterized with FTIR spectroscopy. The FTIR spectra of the extracts showed remarkable peak differences among them, which tell us that different solvents extract different biomolecules from the vegetal material. Then, the extracts were challenged to a silver salt (silver nitrate), and after 2 hours of incubation at 40 °C, the reaction took an amber color, characteristic of AgNPs. The evolution of the reaction through time was evaluated using UV-VIS spectroscopy, as the time passed, the absorption peak at 415 nanometers became more and more intense, confirming the formation of AgNPs. Apart from UV-VIS spectroscopy, the resulting nanoparticles were characterized by Scanning Electron Microscopy (SEM) showing spherical nanoparticles of different sizes ranging from 40 to 100 nanometers. Some important parameters that influence de biosynthesis of nanoparticles are: 1) the type of solvent used in the extraction, 2) the temperature and the time used for the formation of nanoparticles, 3) the pH and 4) the concentration of the extract. AgNPs were stored at -20 °C, and its stability was evaluated during one month using UV-VIS spectroscopy. We find out that the peak at 415 nm remained stable with no change during this period of time, which probes that the methodology used here for AgNPs biosynthesis generates highly stable nanoparticles. The results obtained in the present preliminary work highlight the importance of plant extracts, in this case avocado waste extracts, as a promising natural bioresource for the fabrication of valuable nanomaterials such as biocompatible silver nanoparticles. In this sense, the future work will consist in evaluating the biocompatibility of the synthesized AgNPs in comparison with AgNPs produced with chemical routes, also to characterize the extract and the nanoparticles with other techniques namely HPLC, XRD, DLS and TEM. This information will allow us to understand the underlying mechanisms of nanoparticle synthesis. Once these mechanisms are fully elucidated, we will be able to design AgNPs with tunable physico-chemical properties, increasing its range of applications.

REFERENCES

[1] Yanchatuña O. et al. *Molecules* (2022) (27) (458).
[2] Zhang X. et al. *Int J Mol Sci*. (2016) (17) (1534).
[3] Rajkumar G. et al. *J Mol Liquids.* (2022) (368) (120638).

ACKNOWLEDGMENTS

The authors thank to Yachay Tech University for giving the facilities and the equipment to carry out this work. Also, special thanks to professor Gema González who helped us to perform the SEM analysis.

FIGURES

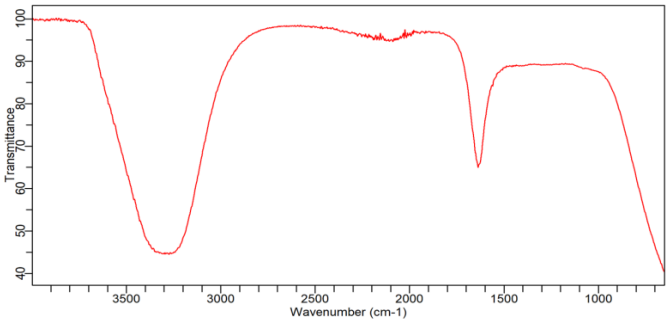

Figure 1: FTIR spectra of *P. americana* aqueous extract showing peaks at 3350 and 1630 cm^{-1}.

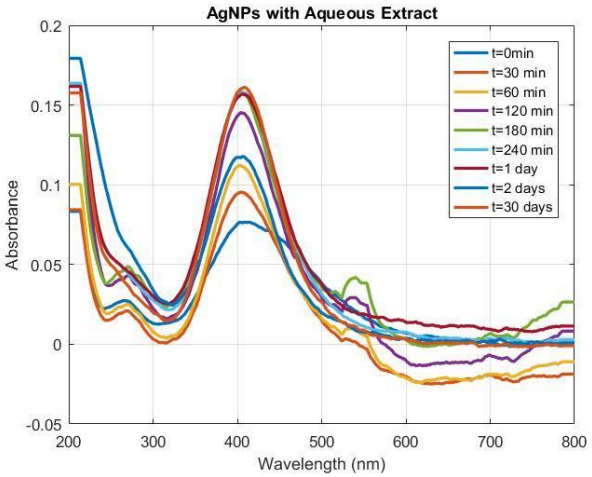

Figure 2: UV-VIS spectra evolution of biosynthesized AgNPs. The absorption peak was 415 nm.

CHARACTERIZATION OF PLANT MATERIAL FROM AMAZONIAN PLANTS FOR THE PREPARATION OF CORROSION INHIBITORS

Elián Cuadros (1), Estefany Almeida (1), Pablo Cisneros (1)

(1)Yachay Tech University, School of Chemical Science and Engineering, Urcuquí, Ecuador.
elian.cuadros@yachaytech.edu.ec

Ecuador, one of the most megadiverse countries in the world, has approximately 10% of all plant species on the planet, so its study is a challenge for modern science . Furthermore, the chemical study of plants with reported biological activity. This work is focused on the study of two plants of great importance in the Ecuadorian Amazon, which are dragon's blood and ungurahua oil, as promised. Dragon's Blood (Croton lechleri) is a tree rich in natural products such as alkaloids and phenolic compounds, its extract has a reddish resin appearance. which has been used for centuries in traditional medicine to treat a variety of ailments. The extract contains high levels of proanthocyanidins, a type of polyphenol, which are believed to have anti-inflammatory, antibacterial, and antiviral properties. In recent years, there has been growing interest in the potential medicinal uses of Croton lechleri, and researchers are exploring its potential as a treatment for conditions such as wound healing, digestive disorders, and cancer. Ungurahua (*Oenocarpus bataua*) contains significant levels of antioxidants and total phenolic compounds, including procyanidins, anthocyanins, and other polyphenols such as stilbenes, phenolic acids, and condensed tannins; It is an oil palm native to the Amazon whose product, ungurahua oil, has a high-quality chemical composition comparable to olive oil. In recent years, there has been growing interest in the potential of *Oenocarpus bataua* as a sustainable source of food and biofuel, due to its ability to grow in diverse environments and its high productivity. Some researchers are also exploring the potential medicinal uses of the tree and its products. Furthermore, the potential applications of these plants as corrosion inhibitors. Corrosion inhibitors are chemical substances that are added to a system (such as a metal surface or an aqueous solution) to reduce or prevent the corrosion of metals. They work by forming a protective barrier on the metal surface, reducing the reaction between the metal and its environment, or by changing the environment to become less aggressive. Common types of inhibitors include organic inhibitors, such as inhibitors that contain nitrogen and/or phosphorus, and inorganic inhibitors, such as nitrates and phosphates. IIn this project, the purification process was carried out with the use of chloroform from the aforementioned plants, with the use of recrystallization and thin layer chromatography (TLC) techniques. For the characterization of the fractions obtained, IR (Figure. 1) and UV-Vis spectroscopy, and corrosion inhibition tests with Aluminum-6061 were carried out. In addition, the determination of the saponification index, solubility tests, and the determination of secondary metabolites was carried out. Finally, after the purification process, a yield of 14% and 34% was obtained of Dragon's Blood. After the different analytical results, the presence of Taspina (secotetrahydroisoquinoline alkaloid) was confirmed with the use of IR.

REFERENCES

[1]Cruz, J., Martınez, R., Genesca, J., & Garcıa-Ochoa, E. (2004). Experimental and theoretical study of 1-(2-ethylamino)-2-methylimidazoline as an inhibitor of carbon steel corrosion in acid media. Journal of Electroanalytical Chemistry, 566(1), 111-121.

[2] Carrillo, W., Carpio, C., Morales, D., & Silva, M. (2018). Fatty acids content in ungurahua oil (oenocarpus bataua) from ecuador. findings on adulteration of ungurahua oil in ecuador. *Asian Journal of Pharmaceutical and Clinical Research*, 391-394.

[3] Gutiérrez, L. F.; Rosada, L. M.; Jiménez, Á. Chemical Composition of Sacha Inchi (*Plukenetia Volubilis* L.) Seeds and Characteristics of Their Lipid Fraction. *Grasas y Aceites* 2011, *62* (1), 76–83. https://doi.org/10.3989/gya044510.

ACKNOWLEDGMENTS

We are grateful to PhD. Pablo Cisneros for this project, PhD. Alex Palma for their support and guidance. Also, to the Yachay Tech University for the use of laboratories and equipment.

FIGURES

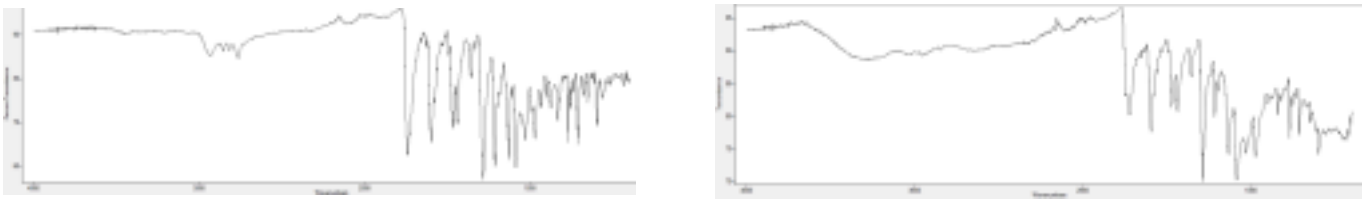

(a) **(b)**

Figure 1. IR Spectra obtained for (a) Taspina, and (b) Taspina HCl.

FIRST PRINCIPLES STUDIES OF TOPOLOGICAL DEFECTIVE GRAPHENE-BASED SUPERLATTICES WITH H ADATOMS

Leonel A. Cabrera (1), and Henry P. Pinto (1)

(1)School of Physical Sciences and Nanotechnology, Yachay Tech University, 100119-Urcuqui, Ecuador Email: leonel.cabrera@yachaytech.edu.ec

In this work, we have studied graphene superlattices with an interesting topological defect called the flower-like Defect (FLD); additionally, we include patterned H adatoms. The so-called flower-like defect (FLD) forms part of the family of grain boundary loops, specifically, the rotational grain boundary family [1]. The FLD can be seen as the rotation of a 24-carbon section to the lattice, which reconfigures the covalent bonds surrounding the flower, creating pentagons and heptagons structures. It would seem that the FLD has C vacancies due to the non-hexagonal structures, but this is not true; in fact, it preserves the density of atoms and the coordination of the pristine graphene. We aim to look for a fundamental understanding of these systems' possible bandgap openings and magnetic properties. The simulations will predict the structure stability, electronic structure, energy formations, simulated scanning tunneling microscopy (STM) images, and possible magnetic properties. DFT calculations were performed with VASP using the meta-GGA functional with van der Waals dispersions r2SCAN+rvv10. The projector augmented wave (PAW) potentials described the core electrons. Additionally, an appropriate kinetic cutoff energy is required to represent the wave functions in a finite (but large enough) basis set of plane wave functions. A convergence process with a criterion of 1 meV per atom was used, obtaining a cutoff energy value of 950 eV. Similarly, a Monkhorst-Pack k-point mesh of 21x21x1 was chosen with a separation of 0.022x2π $Å^{-1}$in the reciprocal space. For all the superlattices, ionic relaxations were allowed to optimize the atoms until all the forces were less than 0.01 eV $Å^{-1}$. The motivation for placing H adatoms in the FLD came to light in [2]. This work reported a significant contribution (2pz orbitals) of the edge C atoms of the FLD to the electronic structure. Then, we expected that H adatoms at the borders of the FLD would notably affect the superlattices' electronic structure. However, we discovered that this hypothesis is only partially true. The next candidate was the Moire-like H pattern reported by Balog, et al. [3], showing a significant change in the electronic structure and motivating us to study two distinct regions of this pattern separately. Ultimately, we selected three regions to analyze the effect of H adatoms in the electronic structure: the border, the inner, and the outer part of the flower, as depicted in FIG. 1. As a starting point; we chose the 6x6 graphene superlattice (FIG. 2). Within these regions, different patterned H configurations were tested for this specific superlattice, changing the sites, directions, and numbers of the H adatoms. We selected only the H configurations with a meaningful change in the band structure and higher formation energies to repeat them for other superlattices.

REFERENCES

[1] Cockayne, E., Rutter, G. M., Guisinger, N. P., Crain, J. N., First, P. N., Stroscio, J. A. (2011). Grain boundary loops in graphene. Physical Review B, 83(19), 195425.
[2] D. Garzon, Dec. 2021, Electronic structure of nobel-graphene based superlattices, Yachay Tech University, Urcuqui 110119. https://repositorio.yachaytech.edu.ec/handle/123456789/449.
[3] Balog, R., Jørgensen, B., Nilsson, L., Andersen, M., Rienks, E., Bianchi, M., ... & Hornekær, L. (2010). Bandgap opening in graphene induced by patterned hydrogen adsorption. Nature materials, 9(4), 315-319.

ACKNOWLEDGMENTS

We are thankful for the fruitful discussions with Domenica Garzon. We also would like to thank the support of the School of Physical Sciences and Nanotechnology at Yachay Tech University.

FIGURES

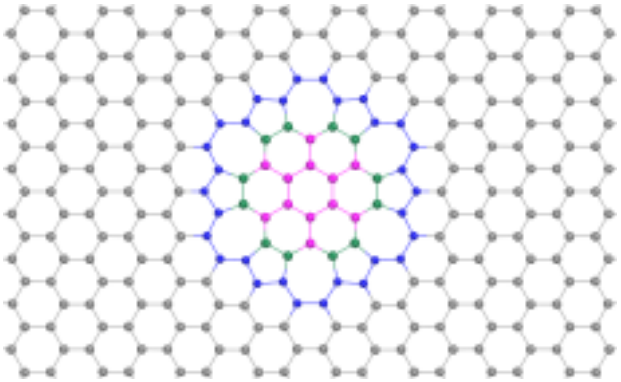

Figure 1. (a) Border (green), (b) inner (magenta), and (c) outer (blue) atoms of the FLD.

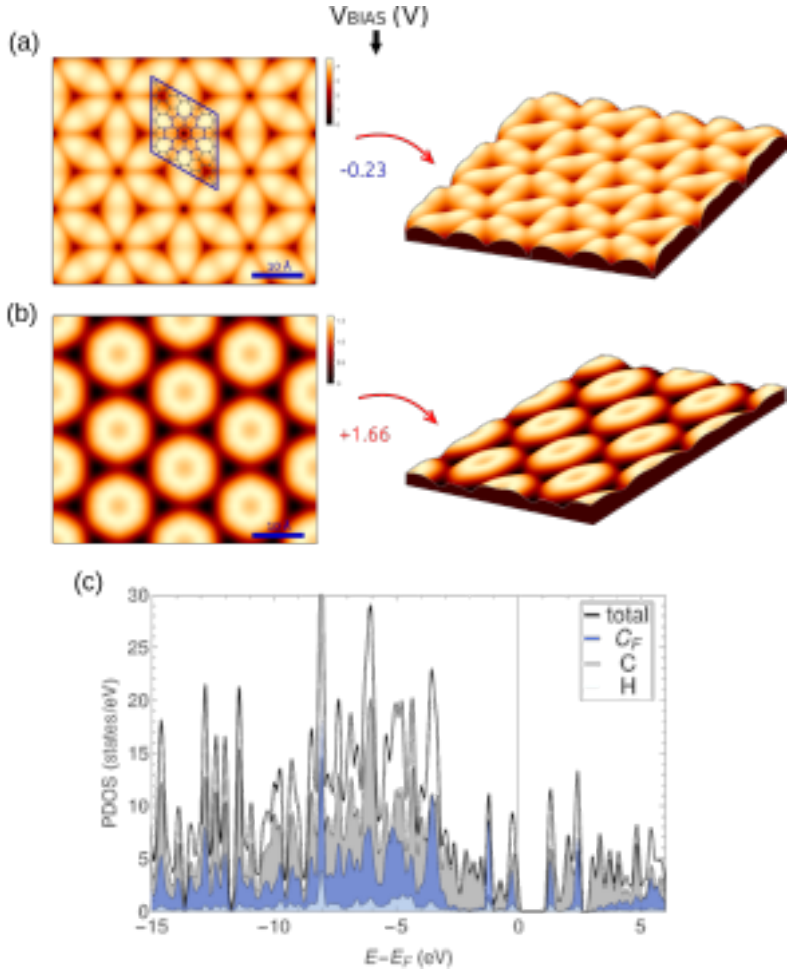

Figure 2. Results for 6x6 graphene superlattice with 12 patterned H adatoms placed on the border of the FLD. Simulated STM images with a bias voltage of (a) -0.23 V (occupied states) and (b) +1.66 (unoccupied states). (c) Computed density of states (DOS) with a bandgap of 1.16 eV.

Acta Microscopica Vol. 32, Supp. 1, 2023
Abstract Book NSSY 2023- Galapagos 23 -29 April, 2023

BLENDS OF TPS WITH MODIFIED MWCNT: CHARACTERIZATION AND APPLICATION

Bryan Garces (1), Luis Corredor (2), Rose Mary Michell (3), Juan Pablo Tafur (1).

(1) School of Chemical Sciences and Engineering. Yachay Tech University. Urcuquí. Ecuador (2) School of Physical Sciences and Nanotechnology. Yachay Tech University. Urcuquí. Ecuador (3) Marthin -Luther University. Halle. Germany.
Email: bryan.garces@yachaytech.edu.ec

In recent years, polymers derived from renewable sources have emerged as an eco-friendly alternative to combat all the pollution generated by synthetics[1], with starch being one of the most promising sources, but with problems such as its poor mechanical, thermal, and conductive properties. Therefore, for this work, MWCNT-COOH (f-MWCNT) was used as a nanofiller to improve starch shortcomings. The objective of this study is the characterization of the samples. First, starch was extracted from the Hass avocado seed to carry out the work. Next, MWCNT was synthesized using the Chemical Vapor Deposition (CVD) equipment with the $CaCO_3$ catalyst and acetylene as a carbon source. For the functionalization of MWCNT was performed, an acid treatment was using HNO_3 conc. Finally, the samples were synthesized in reflux for 14 hours using a starch/glycerol ratio of 100/30 mass and 1% Vitamin E. The composites contain various amounts of MWCNT-COOH (0.5%, 1%, 2%, and 4%), with which the properties were evaluated through X-ray photoelectron spectroscopy, Raman spectroscopy, TGA, X-ray diffraction, electrochemical characterization, and degradability assays. From the analyses, we demonstrate the presence of the carboxylic functionalization of carbon nanotubes by comparing the spectroscopic information obtained with that reported in the literature. Through the XPS spectrum, the elemental study of carbon nanotubes and blends was carried out. As a result, the functionalization of the nanotubes was verified as having a 91.7% of C after its functionalization. In Figure 1. the Raman spectrum irradiated with a laser of 532 nm is shown, where the appearance of the characteristic bands is seen in 1351cm^{-1} (band D), 1577.4 cm^{-1} (band G), and 1620 cm^{-1} (band D '), where the proportion of intensities of the G and D bands is a quantification of the number of carboxyl groups introduced by functionalization. Comparing the I_G/I_D ratio, being 1.5 for MWCNT and 1.3 for f-MWCNT, the increase in disorganization due to the functionalization reaction[2] can be concluded. Figure. 2 shows the thermograms of the composites evaluating the thermal stability and the behavior of the decomposition of the starch samples, where it was observed that the thermal stability of the TPS/f-MWCNT composites was higher as an increase in the quantity of f-MWCNT taking into account the temperature at which the rate of thermal degradation is maximum, being for pure TPS is 312.74°C, and 317.9°C for TPS 4%. This is attributed to the increase in crystallinity samples due to the grafting between the carboxylic group of f-MWCNT and the hydroxyl group of starch, which is confirmed by the diffractograms obtained through X-ray diffraction of the samples (Figure 3), where the incorporation of the f-MWCNT in the starch destroys its crystallinity at low percentages of f-WCNT but for high rates increase crystallinity, increasing the mobility of the chains and increasing thermal stability[3], being the crystallinity degree 21.25% and 22.21% for 1% and 4% f-MWCNT, respectively. The electrical conductivity of TPS/f-MWCNT composites was studied at different temperatures showing a decrease in the conductivity for temperatures up to 30°C (Figure 6). The electrical conductivity was measured at room temperature, increasing the electrical conductivity for composites above 1% f-MWCNT and decreasing for those below respecting with pure TPS, being 2.1 x 10^{-8} and 1.1 x 10^{-7} S/cm for pure TPS and TPS 4% f-MWCNT. The study of degradability was taken by two assays, Respirometry test (Figure 5) and degradation in compost measuring the conversion of the polymer in CO_2 and water; and the loss of weight in the humus, respectively, showing rapid degradation of the sample with 1% of f-MWCNT in comparison with the other samples. The UV-vis spectrum of samples provides evidence of interactions between the carboxyl group of f-MWCNT, and the hydroxyl group of starch observed at 278 nm and having in 222 nm the π-π^* transition, furnishing the evidence that starch macromolecules were grafted to the surface of f-MWCNT. The TPS/f-MWCNT blend films increase electrical conductivity by incorporating 2% and 4% f-MWCNT and enhance thermal stability in any quantitative f-MWCNT. The enhancement in these properties may enable the material for electronic, electrostatically dissipative material, and semiconductor applications.

REFERENCES

[1] Yurdakul, H. et al. *Applied Polymer Science.* (2012) (127) (812).
[2] Montanheiro, T. L. d. A. et al. *Materials Research.* (2014) (30)(55)
[3] Sarat K.Swain. et al. *Carbohydrate Polymers.* (2013) (94) (663)

FIGURES

Figure 1. Raman spectrums of MWCNT and f-MWCNT

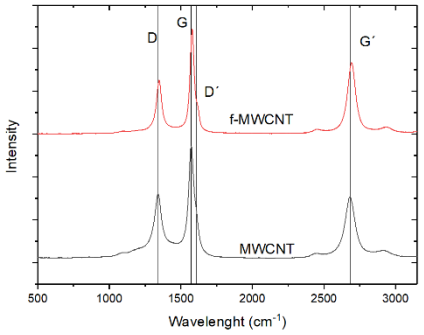

Figure 2. Retained weight versus temperature of indicated TPS/f-MWCNT blends

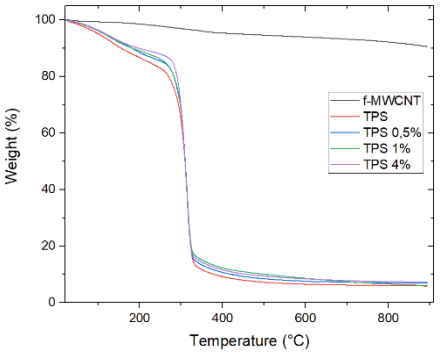

Figure 3. Diffractograms of TPS and its blends

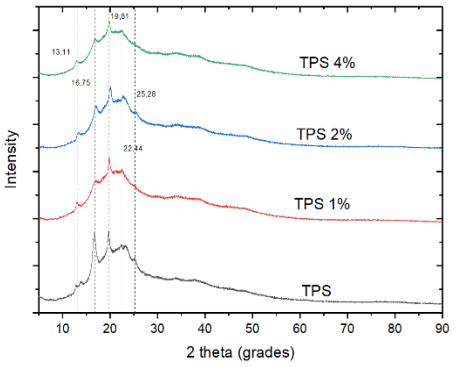

Figure 4. UV-vis spectrum of TPS and TPS/f-MWCNT blends.

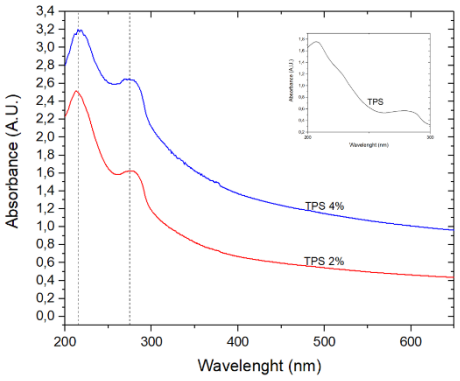

Figure 5. Amount of C released for the blends of TPS with f-MWCNT

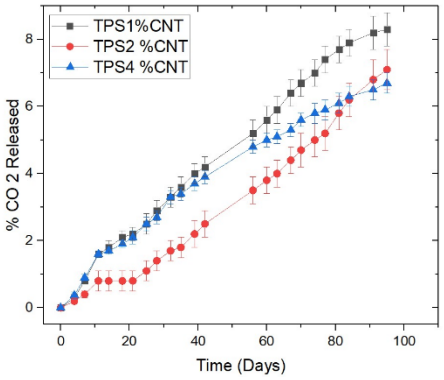

Figure 6. Electrical conductivity of TPS/f-MWCNT blends.

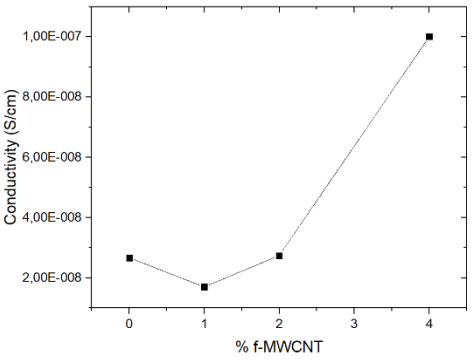

SYNTHESIS OF POLY(3-{[2-(2-METHOXYETHOXY) ETHOXY] METHYL} THIOPHENE 2,5-DYIL) FOR ORGANIC ELECTROCHEMICAL TRANSISTORS APPLICATIONS

Gilda Quezada (1)(2), Preeti Yadav (1), Christine Luscombe (1).

(1) Pi-Conjugated Polymers Unit, Okinawa Institute of Science and Technology (OIST), Onna, Okinawa 904-0495, Japan. (2) School of Physics Science and Nanotechnology, Yachay Tech University, Urcuqui, Imbabura 100-119, Ecuador.
gilda.quezada@yachaytech.edu.ec

Organic electrochemical transistors (OECTs) exhibit a hybrid electrical–ionic conduction mechanism, where electrochemical doping/dedoping of the channel yields a significant modulation of conductivity at low operating voltages (<1V) [1]. This effect enables very low levels of detection of biological materials through signal amplification. OECTs have emerged as a promising platform for transducing small changes of ion concentrations to large changes in electrical current, garnered considerable interest for sensing and bioelectronic applications. In previous studies, ethylene glycol-based side chain polymers have shown very promising ion uptake and transport properties in both p-type and n-type polymers in aqueous electrolytes [2]. OECT performance enhancement using oligoethylene glycol side chains is generalizable to several different conjugated backbones, including polythiophene, benzodithiophene, propylenedioxythiophenes, and bithiophene-thieno-thiophene [3]. In this study, we report the synthesis and performance of Poly(3-{[2-(2-methoxyethoxy) ethoxy] methyl} thiophene-2,5-dyil) (P3MEEMT) as organic semiconductor channel for accumulation-mode organic electrochemical transistors (OECTs). P3MEEMT consists of a thiophene backbone and an oligoethylene glycol-side chain with a methylene spacer bonded to the thiophene ring and the first oxygen atom of the oligoethylene glycol chain. Figure 1 represents the steps involved in the synthesis of 2,5-dibromo-3-methoxyethoxyethoxymethylthiophene (3MEEMT) monomer starting with the bromination of 3-thiophenemethanol (I) using NBS, producing 2,5-dibromo-3-thiophenemethanol (II), which on treatment with Phosphorus tribromide yields 80% of compound III. In the next step, compound III was treated with diethylene glycol monomethyl ether (DGME) and NaH to give 3MEEMT monomer in 60% yield. The polymerization of 3MEEMT was achieved via Kumada Catalyst Transfer Polymerization (KTCP). 3MEEMT monomer was first activated with one equivalent of isopropyl magnesium chloride lithium chloride complex (*i* PrMgCl•LiCl) in THF, followed by addition of Ni(dppp)Cl_2 to initiate the cross-coupling to form the conjugated polymer. The polymerization reaction was quenched using dil. HCl; and MeOH induced the precipitation of the polymer, enabling isolation over a filter. The polymer was purified using successive Soxhlet extractions with MeOH, acetone, and hexane. Then, it was collected with $CHCl_3$, and rotary evaporation was used to remove the remain solvent. Finally, the polymer was dried under high vacuum and storage. Figure 2 shows the structural characterization of 3MEEMT and P3MEEMT made through proton nuclear magnetic resonance (^{1}H NMR). P3MEEMT showed a number average molecular weight (M_n) of 9,2 kg/mol and a dispersity of 1,45 through size exclusion chromatography (SEC). The use of P3MEEMT as conductive channel layer for OECTs application is in progress (Figure 3). The OECT device fabrication consists of the deposition of a negative resistor on Si substrate through spin coating, followed by UV light exposure and resist development. Metal deposition of gold, for the source (S) and drain (D) electrodes, is accomplished via e-beam evaporation, and the resist lift-off is achieved by soaking wafers in acetone solution. Then P3MEEMT is spin coated onto OECT substrates and an insulating layer is used to avoid the direct contact between the gold electrodes and the electrolyte. An Ag/AgCl pellet is immersed in the electrolyte to work as the gate electrode (G). The operation of the OECT is controlled by voltages applied to the gate electrode (Ag/AgCl) and drain electrode (D) during further characterizations. The development of an improved sensor design methodology via OECT-based organic transistor device is the next challenge. A molecular imprinted polymer (MIPs) layer will be introduced strategically in the OECT sensor assembly to produce an increased selectivity

for a specific molecule (serotonin) in an aqueous environment.

REFERENCES

[1] Chen E. et al. J. Mater. Chem. A (2022) (10) (10738)
[2] Flagg L. et al. J. Am. Chem. Soc. (2019) (141) (4345)
[3] Rivnay J. et al. Nat. Rev. Mater. (2018) (3) (17086)

ACKNOWLEDGMENTS

Financial support from the Okinawa Institute of Science and Technology Graduate University is gratefully acknowledged.

FIGURES

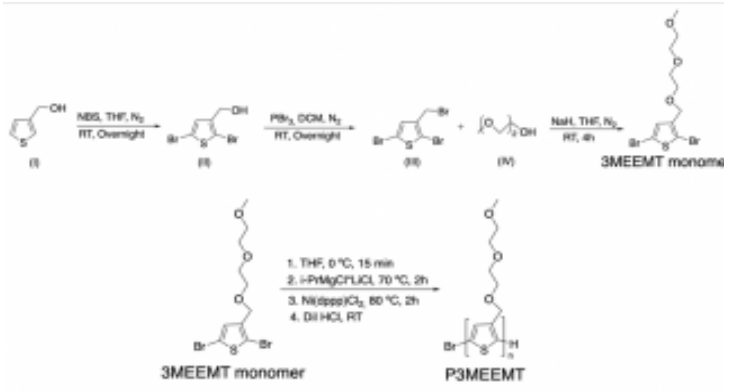

Figure 1. Synthesis schemes of 3MEEMT monomer and P3MEEMT by Kumada Catalyst Transfer Polymerization (KCTP).

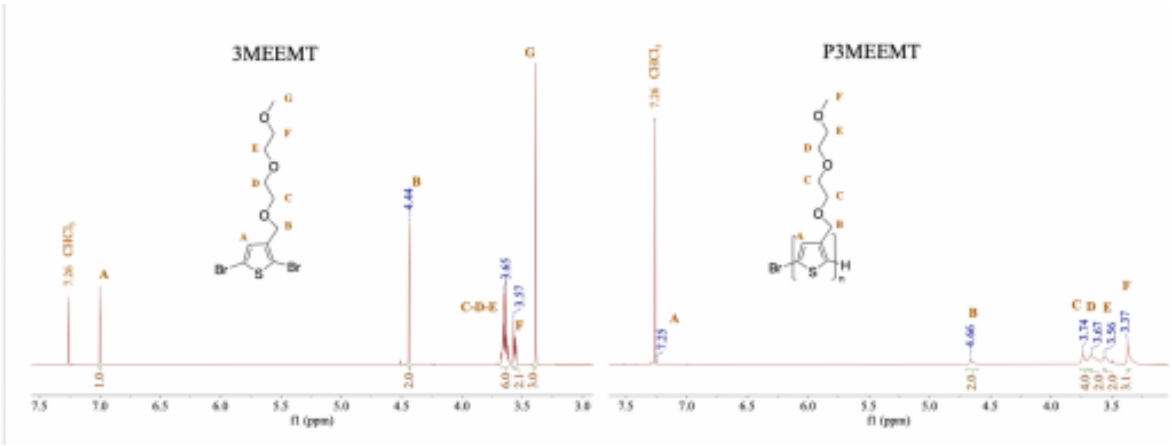

Figure 2. 1H NMR of 3MEEMT and P3MEET with backbone peak labels

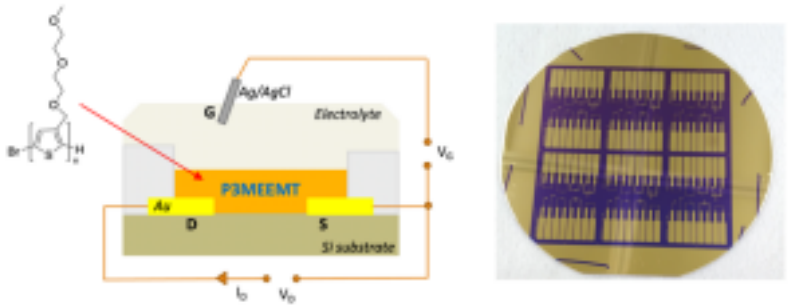

Figure 3. Schematic representation and photograph of OECT devices using P3MEEMT as conductive layer.

Acta Microscopica Vol. 32, Supp. 1, 2023
Abstract Book NSSY 2023- Galapagos 23 -29 April, 2023

OBTENTION AND CHARACTERIZATION OF COLLAGEN FROM EGGSHELL MEMBRANE

Nardy J. Sallo-Chabla (1), Caterine Yesenia Carrasco Montesdeoca* (2).

(1) School of Physics and Nanotechnology, University of Research of Experimental Technology Yachay, Urcuquí - Imbabura 100115, Ecuador.
(2) School of Biological Sciences and Engineering, University of Research of Experimental Technology Yachay, Urcuquí - Imbabura 100115, Ecuador.
nardy.sallo@yachaytech.edu.ec

Collagen is a fibrous protein that is a major component of the extracellular matrix in connective tissues in the body. There are at least 28 different types of collagen identified so far, but collagen type I is the most abundant type in the body, making up about 90% of the collagen in bone tissue, and is also found in other tissues such as skin and tendons. Moreover, due to their excellent biocompatibility and low immunogenicity, collagen-based biomaterials are of the most importance for tissue engineering and regenerative medicine. Collagen can be extracted from a variety of sources, including land-based animals like cows and pigs, but there are some limitations to using these sources. For example, concerns about disease transmission, ethical considerations, and limited availability have led to exploring safe and cost-effective alternative sources of collagen. [1] In this context, collagen extraction from by-products is one of the most recent and promising perspectives. Thus, considering the high egg production in Ecuador, which reaches values of 4.000 million per year, and the potential content of collagen, this project studies the extraction and characterization of collagen from eggshell membranes (ESM). This research aimed to compare two methods to optimize a reproducible extraction protocol and assess the physical and chemical properties. The first method starts by immersing the hen eggshell in 0.5M HCl overnight, followed by a wash using 0.1M NaOH for one hour and rowing with distilled water ten times. After that, the ESM was mechanically stripped from the shell. In the second treatment, the eggshell membranes are manually separated from the eggshells and then washed with distilled water to remove debris or dirt. Then, the membranes were treated with an aqueous acetic acid solution (16g/l) three times to remove mineral substances. After that, an acetic acid - sodium acetate buffer solution is to adjust the pH (4.8 - 5.0), and then it is dehydrated using ethyl alcohol. The final sample of the eggshell membrane was obtained using only applying a cleaning treatment with distilled water. After each treatment, samples are immersed in a 0.5M solution of acetic acid for 24h hours at room temperature to allow for the collagen to dissolve. After the acid treatment, the eggshell membranes are filtered to remove any impurities or solid particles. The acid solution is neutralized with sodium hydroxide to bring the pH of the solution to a neutral level. The neutralized solution is then cooled to induce collagen precipitation (-20ºC for 24h). The precipitated collagen is then collected by centrifugation and washed with distilled water to remove any remaining impurities. Finally, the collagen is freeze-dried to produce a fine powder. After the extraction process, the characteristics of ESM were assessed by Fourier transforms infrared spectroscopy, Raman spectroscopy, and differential scanning calorimetry. The FTIR showed that the separation methods did not alter the chemical structures and clarified the composition of the fibrous proteins of the ESM. FTIR provided information on main peaks for amide I (~1630 cm^{-1}), II (~1550 cm^{-1}), III (~1232 cm^{-1}), as well as for amide A (~3275 cm^{-1}), B (~2930 cm^{-1}) [2]. The molecular structure was also confirmed using Raman spectroscopy showing three predominant bands corresponding to C-H deformation (~1450 cm^{-1}), C=O stretching of the peptide bond (amide-I band) (1666 - 1700 cm^{-1}), and C-H stretching modes (~2930 cm^{-1}), demonstrating the presence of collagen type I [3]. Moreover, from the amide II peak identified at 1522 cm^{-1}(at FTIR spectra), the helix structure of the molecule can be confirmed; hence, by contrasting with the spectra for treatments A and B, we can conclude that the acetic acid method maintains a better structure of collagen, allowing a good dispersion of proteins in eggshell membranes. Currently, we are conducting studies to determine the thermal properties of the extracted collagen by a thermogravimetric Analysis (TGA) and analysis of differential scanning calorimetry (DSC). Therefore, the thermal denaturation temperature of collagen ESM will be determined, allowing us to evaluate the applicability for developing a hydrogel for various usage in biomedical and tissue engineering.

REFERENCES

[1] Zurita-Méndez, N. et al. Front Bioeng Biotechnol. 2022)(10)
[2] Zhao, Y. et al. Biotechnology. (2009)(8)
[3] Paschou, A. et al.The FEBS journal. (2018) (285) (2641-2653)

ACKNOWLEDGMENTS

We thank the support of the laboratory technicians at Yachay Tech's Laboratories from the School of Biological Sciences and Engineering, the School of Physical Sciences and Nanotechnology, and the School of Chemistry and Engineering.

FIGURES

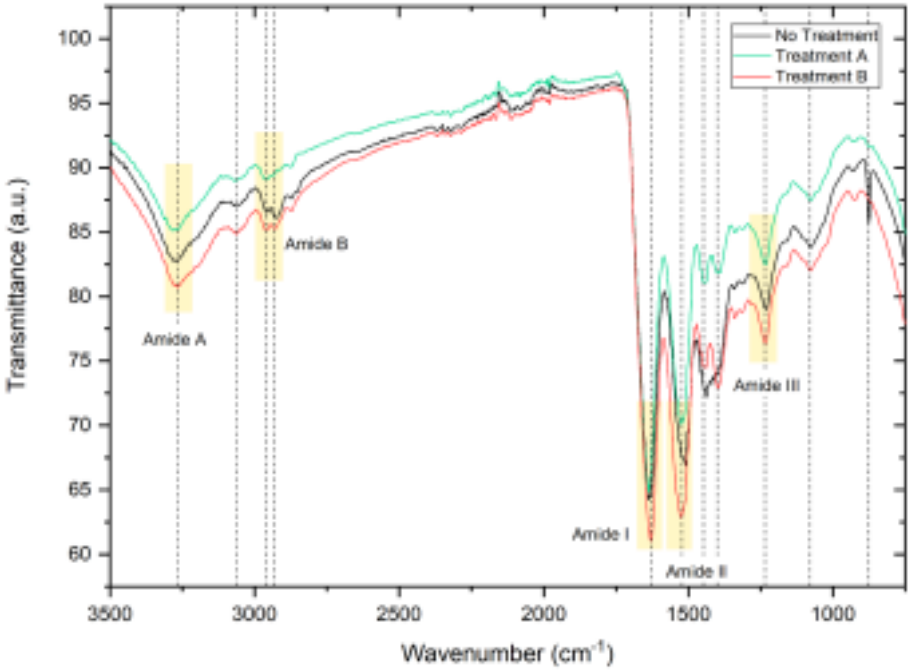

Figure 1. FTIR of the samples obtained for each treatment: without treatment (black), treatment A (green), treatment B (red). Characteristic peaks for amide I, II, III, A and B are clearly identified.

THURSDAY

Poster Session 2

Acta Microscopica Vol. 32, Supp. 1, 2023
Abstract Book NSSY 2023- Galapagos 23 -29 April, 2023

ANTIBACTERIAL ACTIVITY OF METAL NANOPARTICLES AGAINST BACTERIA OF CLINICAL ORIGIN

Marcelo Guerrero-Almonacid (1), Manuel Parigüana (2), Gema González (3), Zoraya López-Cabaña (4)

(1) Bio&Nano Materials Lab Drug Delivery and Controlled Release, Universidad de Talca, 3460000 Talca, Maule, Chile. Email: marcelo.guerrero@utalca.cl
(2) Bio&Nano Materials Lab Drug Delivery and Controlled Release, Universidad de Talca, 3460000 Talca, Maule, Chile
(3) Yachay Tech University, School of Physical Sciences and Nanotechnology, 100119 Urcuquí, Ecuador
(4) Chemistry Institute of Natural Resources, University of Talca, PO Box 747, Talca, Chile

Infections by multi-drug resistant (MDR) bacteria will cause around 10 million deaths in 2050 according information from the World Health Organization. The increase of MDR isolates occurs mainly in hospitals, creating a bacterial population for each health center. These bacteria are carried by health professionals, colonize instrumentation and infect to long-term patients. This fact has been aggravated by COVID-19 pandemic, where thousands of patients acquired a secondary bacterial infection [1]. Therefore, it is essential to research new therapeutic alternatives to classic antibiotics that do not generate resistance in a short period of time and allow treatment according to the bacterial strain, resistance profile and the kind of sample. A widely studied therapeutic alternative in recent years corresponds to the use of metal nanoparticles (NPM) with antibacterial properties. The most studied correspond to NPMs of Silver, Zinc, Copper and Magnesium [2]. However, previous research shows that antibacterial activity requires high concentrations of NPM to be effective. In addition, these NPMs are evaluated only in bacterial strains used in quality control, including environmental bacteria [3]. For this reason, the need arises to evaluate the antibacterial properties of these NPMs in strains of clinical origin, in order to obtain an objective view of their potential clinical use. **Objective**: Evaluate the antimicrobial activity of different metallic nanoparticles against bacteria of clinical origin, isolated in the city of Talca, Maule, Chile. **Methodology**: Six different metallic nanoparticles were synthesized, Silver (AgNps), Magnesium oxide (MgONps), Zinc oxide (ZnONps), Bismuth oxide (Bi_2O_3Nps), Cerium oxide (CeO_2Nps) and Copper oxide (CuONps). Synthesis included two NPMs reduction methods, first one using sodium hydroxide (NaOH) and second, tannic acid (Ta.ac). The Mueller-Hinton agar diffusion method was used to evaluate the antimicrobial activity against eight different bacterial species of clinical origin, including: *Staphylococcus aureus*, *Pseudomonas aeruginosa* and *Acinetobacter baumannii*, due to their clinical importance. Bacterial inoculums were prepared from overnight pure cultures. The concentration of the inoculum in physiological serum (0.9% NaCl) was 0.5 Mac Farland, standardized by spectrophotometric reading between 0.08-0.1 AU at 625nm wavelength. Different NPMs were dissolved in sterile water, concentration 1mg/100uL. 50uL of each NPM was dispensed into wells previously made in the agar. The inoculated plates were left at 37°C for 18 hours. After this, the interpretation was carried out. **Results**: The AgNps presented growth inhibition against seven of eight bacterial species evaluated in this study, including *Staphylococcus aureus*, *Pseudomonas aeruginosa* and *Acinetobacter baumannii*, with inhibition halos of 16, 19 and 20 mm of diameter respectively (Table N°1). The CuONps presented specific activity against *A. baumannii*. MgONps, ZnONps, Bi_2O_3Nps and CeO_2Nps did not present inhibition against the evaluated bacteria (Figure N°1). No difference in antimicrobial activity was observed between NPMs reduced with NaOH and reduced with Ta-ac. **Conclusions**: In this study, the activity of six different NPMs was evaluated against eight bacterial strains of clinical origin. AgNps and CuONps inhibited growth against bacteria of clinical origin. The rest of the NPMs evaluated did not present activity despite following the synthesis protocols reported in literature that included effective antibacterial activity. This fact could be explained by the use of bacterial strains of clinical origin, since they can express different types of mechanisms that confer resistance to antibiotics and to the NPNs of this study. It is necessary to evaluate the antibacterial capacity of different compounds that are currently postulated as an alternative to classical antibiotics. Both, against bacterial strains of clinical origin and certified bacterial strains, in order to obtain objective information regarding the susceptibility of the circulating bacterial population in health centers. of each geographical area. Thus, finding the best treatment alternative, according to each particular case of infection, bacterial species and resistance profile.

REFERENCES

[1] Chih-Cheng Lai. et al. *Elsevier Sci*. (2021) (57) (106324).
[2] Rodriguez-Barajas N. et al. *Bentham. Sci*. (2022) (22) (2506-2526).
[3] Alaoui Mdarhri H. et al. *Antibiotics, MDPI.* (2022) (11) (1826).

ACKNOWLEDGMENTS

The authors thank the Institute of Chemistry and Natural Resources of the University of Talca and the FOVI210019 project.

FIGURES

		AgNps	MgONps	ZnONps	Bi_2O_3Nps	CeO_2Nps	CuONps	PC	NC
A	*S.aureus*	16	0	0	0	0	0	15	0
B	*P.aeruginosa*	19	0	0	0	0	0	18	0
C	*A.baumannii*	20	0	0	0	0	14	19	0
D	*E.coli*	17	0	0	0	0	0	19	0
E	*K.pneumoniae*	16	0	0	0	0	0	19	0
F	*E.cloacae*	16	0	0	0	0	0	19	0
G	*C.freundii*	22	0	0	0	0	0	20	0
H	*S.maltophilia*	0	0	0	0	0	0	0	0

Table 1. Measurement of inhibition halos diameter expressed in mm. NPM against different bacterial strains of clinical origin. PC: Positive control corresponding to peptide with broad-spectrum antimicrobial activity. NC: Negative control corresponding to sterile water.

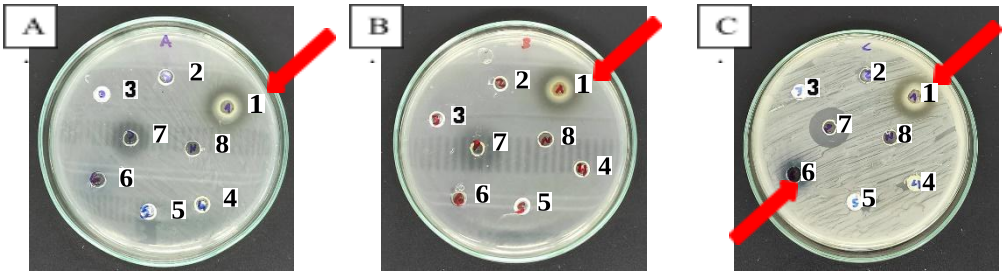

Figure 1. Diffusion plates on Mueller-Hinton agar. In A) *S.aureus*, B) *P.aeruginosa* and C) *A.baumannii*. Growth inhibition caused by AgNps against bacteria of clinical relevance is evidenced. In C, the inhibition of bacterial growth caused by CuNps is evident. NPM: AgNps (1), MgONps (2), ZnONps (3), Bi_2O_3Nps (4), CeO_2Nps (5), CuONps (6), Positive Control (7), Negative Control (8).

Acta Microscopica Vol. 32, Supp. 1, 2023
Abstract Book NSSY 2023- Galapagos 23 -29 April, 2023

PHOTOINDUCED QUANTUM TRANSPORT

Jeyson P. Alomoto (1), Daniel González (1), Duncan J. Mowbray (1), Vito Despoja (2).
(1)1School of Physical Sciences and Nanotechnology, Yachay Tech University, Urcuquı́ 100119, Ecuador.

(2)Institute of Physics, 10000 Zagreb, Croatia

Creating organic photovoltaics that are both cost-effective and environmentally friendly is a current goal in the field of physical and nanotechnology scientific research. To achieve this, it is needed to explore the use of computational methods to design the next generation of OPVs. However, accurately describing the way large molecules within these systems undergo excitation processes requires the development of advanced computational techniques. Once it is constructed a stable computational model, it is possible to effectively describe the physical properties of interest of our system and then contribute to the efforts of getting novel materials to the society. Specifically, our point of interest is the External Quantum Efficiency (EQE) of a photovoltaic device, which determines how much a device is capable of converting incident photons into electrons. In order to develop new and better OPVs materials, modeling the EQE of a solar cell using ab initio methods to accurately describe their efficiency is necessary. To address this problem, we must include the optical absorption process at the independent particle approximation level as a coupling between two leads of the conducting circuit (FIG. 1). At the quantum regime, it is possible to use the non-equilibrium Green's function formalism to determine the EQE of these types of systems. By the implementation of a python code based on GPAW, it is possible to achieve the computational calculations to obtain the observables of interest in this system. Particularly, different models were used for constructions of SWCNT with different chiralities. The difference in the chiralities characterize if the SWCNT is metallic or semiconducting. The optical absorption, charge carrier generation and the charge transport of low dimensional organic photovoltaic systems such as a carbon chain and single-walled carbon nanotubes (SWCNTs) have been analyzed. Particularly, the SWCNTs were modeled using this computational structure. Taking into account the region of available allowed states for absorption to occur, the absorption and transmission probability T is calculated as a function of the initial energy.
The absorption, transmission, overlapping and Kohn Sham Hamiltonian matrices are represented using a linear combination of atomic orbitals (LCAO). To test our method for calculating the EQE of a system, we first apply it to a simple two-level four site tight-binding (TB) toy-model system consisting of an occupied and unoccupied band coupled via an external electromagnetic field (FIG. 2). The absorption and transmission probability and its behavior is shown as a function of initial energy and excitation energy (FIG. 3). We find a four atom periodic carbon chain aligned in the x-direction has a relaxed carbon-carbon bond length of $d_{C-C} \approx 1.39$ Å. Finally, contributing to the computational design of novel low-dimensional organic photovoltaic systems could enhance research and development in this important area of physics.

REFERENCES

[1] Glowacki, J. Jung, J. Ulanski, and A. Rybak, 2.33 - Conductivity Measurements, in Polymer Science: A Comprehensive Reference, edited by K. Matyjaszewski and M. Möller (Elsevier, Amsterdam, 2012) pp. 847–877.
[2] Y. Meir and N. S. Wingreen, Landauer formula for the current through an interacting electron region, Phys. Rev. Lett 68, 2512 (1992).
[3] S. Datta, Electronic Transport in Mesoscopic Systems, Cambridge Studies in Semiconductor Physics and Microelectronic Engineering (Cambridge University Press, Cambridge, 1995).
[4] C. Meis and P. R. Dahoo, Vector potential quantization and the photon wave-particle representation, J. Phys. Conf. 738, 012099

ACKNOWLEDGMENTS

I would like to express our deep gratitude to our thesis advisor, Duncan Mowbray, for their exceptional guidance, support, and mentorship. Their unwavering dedication to excellence and their ability to challenge us intellectually have been instrumental in our academic and personal growth. We extend our gratitude to the School of Physical Science and Nanotechnology for providing the resources and infrastructure necessary for the successful completion of this research.

Finally, we would like to thank our families and friends for their love, encouragement, and support throughout our academic journey. Their unwavering belief in us has been a constant source of motivation, and we are deeply grateful for their presence in our lives.

FIGURES

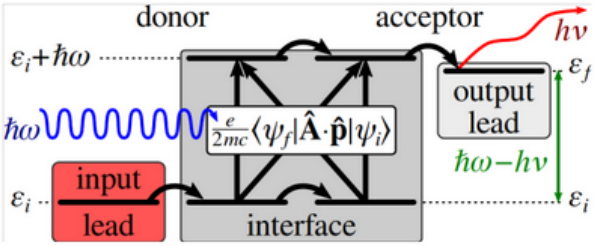

FIG. 1: Schematic of an excitation process across a donor–acceptor interface from an occupied initial state with energy εi in the input lead to an unoccupied intermediate state with energy $\varepsilon i + \hbar\omega$ via the interaction between an external electromagnetic field with vector potential $\hat{\mathbf{A}}$ and momenta $\hat{\mathbf{p}}$, $e/2mc\langle\psi f|\hat{A}\cdot\hat{p}|\psi i\rangle$ and via coupling to a $2mc$ phonon mode of energy hν to an unoccupied final state with energy $\varepsilon f = \varepsilon i + \hbar\omega - h\nu$ in the output lead.

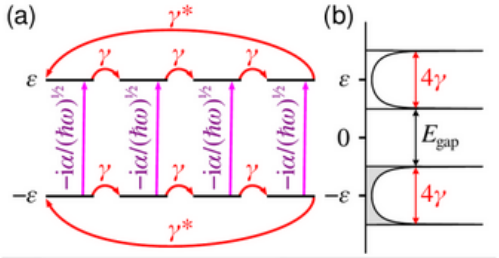

FIG. 2: (a) Schematic depicting a two level four site tight-binding (TB) model $|\varphi\pm i\rangle$ with onsite energies $\pm\varepsilon$ (black lines), interatomic coupling γ (red arrows), and occupied to unoccupied coupling via the external electromagnetic field $-i\alpha/(\hbar\omega)$^1/2 (magenta arrows) and (b) calculated density of states (DOS) showing energy gap Egap , band widths 4γ, and occupation (gray filling).

Acta Microscopica Vol. 32, Supp. 1, 2023
Abstract Book NSSY 2023- Galapagos 23 -29 April, 2023

FACILE METHOD FOR DISPERSING ECUADORIAN CVD CARBON NANOTUBES AND ANALYSIS THROUGH RAMAN SPECTROSCOPY, SEM AND XPS

Óscar Ortiz (1), José Pizha (2). Julio C. Chacón-Torres (2*)

(1) Departamento de Materiales, Facultad de Ingeniería Mecánica, Escuela Politécnica Nacional, Quito, Ecuador.
(2) School of Physical Sciences and Nanotechnology, Yachay Tech University, 100119 Urcuquí, Ecuador.
oscar.ortiz02@epn.edu.ec

Carbon nanotubes (CNTs), a 1D-allotrope form of carbon, excel from their exceptional chemical and physical properties [1]. In order to fully exploit their physical and electronic properties, the carbon nanotubes must be individualized and purified after their synthesis process. There exist various studies that report the possibility of dispersing [2], purifying [3] and to individualize carbon nanotubes [4]. Two of the main effective routes towards CNTs individualization are: (i) chemical by means of surfactants, solvents, and strong acids; and (ii) mechanical by means of ultrasound or shear mixing. However, the main drawback of these techniques lies in the final morphology of the resulting material causing defects in the walls of the nanotubes or fractures that alters the intrinsic properties of the nanotubes [5]. In addition, the use of surfactants is not friendly to the environment and leaves residues on the surface of the nanotube that require post treatments to be removed [6]. In this work, we report a facile green synthesis method to obtain a homogeneous and stable dispersion of carbon nanotubes in a water solution based on the principle of intercalation of compounds. A solution of saline water was made at different concentrations were carbon nanotubes got immersed and further dispersed by using an ultrasonic bath. Four samples were made showing a stable dispersion over time two hours. A drop of the CNTs/NaCl solution was drop casted on a silicon dioxide wafer by spin coating. Individual carbon nanotubes were obtained and analyzed by Raman spectroscopy. The best dispersion and individualization was obtained when 2 [mg] of CNTs were added to a 3422 [mM] NaCl solution in distilled water. We were able to find several individualized CNTs from which their Raman spectra reveals the characteristic G-, D- and 2D-lines from a multi-walled carbon nanotube without functionalization and highly crystalline. The D/G ratio obtained for the individualized CNT was about 0.3 revealing a low defect concentration. However, the is a prominent peak around 270 cm^{-1} in the region of the RBMs, which may indicate the potential presence of single-walled carbon nanotubes, that may have created a small bundle. This method reveals a facile novel method to successfully individualize carbon nanotubes in aqueous solutions that can be potentially extended to diverse carbon allotropes, but it need further studies. Moreover, this methodology can be scaled-up aiming for a mass production of individualized carbon nanotubes for industrial applications.

REFERENCES

[1] Mathur R. (2016) *Carbon nanomaterials: synthesis, structure, properties and applications*, Taylor & Francis, pp. 83-84.
[2] Huang Y. et al. *Polymers* (2012) (4) (276).
[3] Domagała K. et al. *Mater. Lett.* (2019) (253) (272).
[4] Pénicaud A. et al. *Carbon* (2014) (67) (361).
[5] Paredes J. et al. *Langmuir* (2004) (20) (5149).
[6] Badmus S. et al. *Environ. Sci. Pollut. Res.* (2021) (28) (62087).

ACKNOWLEDGMENTS

We thank the support of the laboratory technicians at Yachay Tech's Laboratories from the School of Physical Sciences and Nanotechnology.

FIGURES

Figure 1. a) Homogeneous and stable dispersion of carbon nanotubes in a water solution. b) A drop of the CNTs/NaCl solution on a silicon dioxide wafer. c) A carbon nanotube individualized and observed with a 100X optical microscope objective.

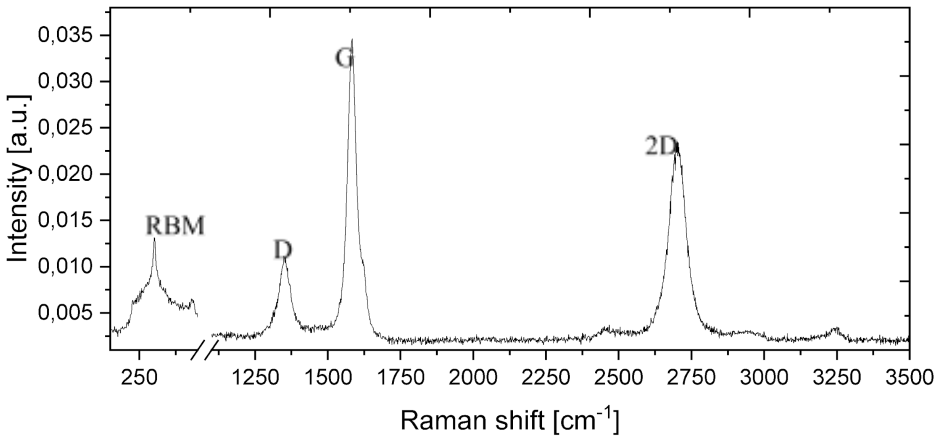

Figure 2. Raman spectra of a multiwalled carbon nanotube.

SYNTHESIS AND CHARACTERIZATION OF CHITOSAN FIBERS *VIA* ELECTROSPINNING

Dulexy Solano (1), Luis Corredor (2), Julio C. Chacón-Torres (2*).

(1) School of Biological Sciences and Engineering, Yachay Tech University, Urcuquí 100115, Imbabura, Ecuador.
(2) School of Physical Sciences and Nanotechnology, Yachay Tech University, Urcuquí 100115, Imbabura, Ecuador.
dulexy.solano@yachaytech.edu.ec

Chitosan is one of the most abundant natural polysaccharides, and the global market volume is expected to reach 2.55 x10^9 dollars by 2022 [1]. The high demand for chitosan is due to its unique properties in the biomedical field: biologically renewable, biodegradable, biocompatible, non-antigenic, non-toxic, and biofunctionality [2]. One of the main ways of obtaining chitosan is based on reusing a large percentage of waste representing around 40% of total shrimp production in Ecuador [3]. Obtaining biomaterials from natural waste can be recognized as an innovative technique to inspire a new frontier based on the current research improve tissue engineering scaffolds by increasing their cytocompatibility while mimicking the native extracellular matrix [4]. In this work we produced pure chitosan fibers using 3 types of chitosan sources: 1) shrimp chitosan, 2) crab chitosan and 3) commercial chitosan purchased from Sigma-Aldrich. The chitosan solutions dissolved in acetic acid (AcOH) were reinforced with multi-walled carbon nanotubes (MWCNTs) to improve their viscosity. In order to produce the fibers, a standard electrospinning device was used employing a 10 mL syringe attached to a stainless steel needle into a programmable syringe pump using an aluminum foil as a collector placed 6-18 cm from the end of the syringe. Samples were collected for 1 hour for each experiment and then the fibers were characterized by Raman spectroscopy. The entire process is described in Figure 1. Among the different chitosan solutions tested for the electrospinning of chitosan none of them produced a visible jet as the electric field was applied (data not shown). By changing the solvent to Trifluoroacetic acid (TFA), chitosan fibers obtained onto the collector. Figure 2 shows chitosan electrospun fibers with smooth surface and bead-free uniform diameters along their lengths. There exist two possible reasons to explain the successful fibers formation when using TFA: (i) TFA forms salts with the amino groups of chitosan, and this salt formation destroys the rigid interaction between the chitosan molecules, making them ready to be electrospun; (ii) the high volatility of TFA is advantageous for the rapid solidification of the electrified jet of the chitosan-TFA solution. Figure 3 shows the electrospun chitosan nanofiber characterization via Raman spectroscopy, revealing amide groups terminated chitosan nanofibers with a stable structure. The prominent Raman peaks are assigned as follows; the CC stretching region (1050-1200 cm^{-1}), Amide III bands (1230-1270 cm^{-1}), and -NH amide I (1600 cm^{-1}) [5]. The electrospun chitosan nanofibers exhibit weak trans-amide conformation (1310-1350 cm^{-1} and 1420-1490 cm^{-1}). The successful chitosan fibers obtained by electrospinning serve as a novel route to produce smart scaffold applicable, especially for tissue engineering. In contrast to conventional wound treatment, chitosan fibers prevent scarring in the treatment of large wounds, such as burns and abrasions [6] The developed fibers are very promising to act as localized drug delivery systems for wound care applications. Finally, the wide panel of chitosan properties and processed materials gives to this biosourced polymer a quite promising future as biomaterial as demonstrated by emerging products on the market notably in the wound dressing field.

REFERENCES

[1] Fatullayeva, S., Tagiyev, D., Zeynalov, N., Mammadova, S., & Aliyeva, E. (2022). Recent advances of chitosan-based polymers in biomedical applications and environmental protection. *Journal of Polymer Research*, *29*(7), 259. https://doi.org/10.1007/s10965-022-03121-3

[2] Antaby, E., Klinkhammer, K., & Sabantina, L. (2021). Electrospinning of chitosan for antibacterial applications—current trends. In *Applied Sciences (Switzerland)* (Vol. 11, Issue 24). MDPI. https://doi.org/10.3390/app112411937.

[3] Costa, P. (2013). *Estudio de viabilidad de exportacion de desechos procesados de camaron generados por las mayores exportadoras ecuatorianas hacia China*.

[4] Sakkara, S., Santosh, S., & Reddy, N. (2020). *Chitosan Fibers*.

[5] J. S. Stephens, D. B. Chase, and J. F. Rabolt, *Macromolecules*, 37, 877 (2004)
[6] Cui, C., Sun, S., Wu, S., Chen, S., Ma, J., & Zhou, F. (2021). Electrospun chitosan nanofibers for wound healing application. In *Engineered Regeneration* (Vol. 2, pp. 82–90). KeAi Communications Co. https://doi.org/10.1016/j.engreg.2021.08.001

ACKNOWLEDGMENTS

Thanks to MSc. Ana Carmen Valbuena Inciarte for her support in the synthesis of the polymer solution.

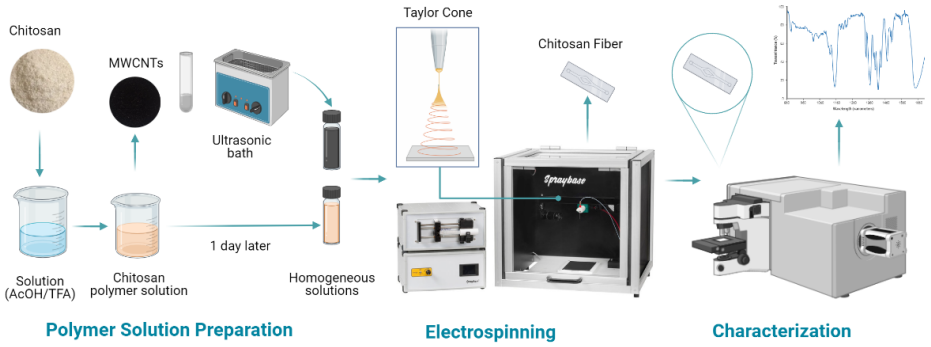

Figure 1. Illustration of the fiber synthesis process carries out by electrospinning.

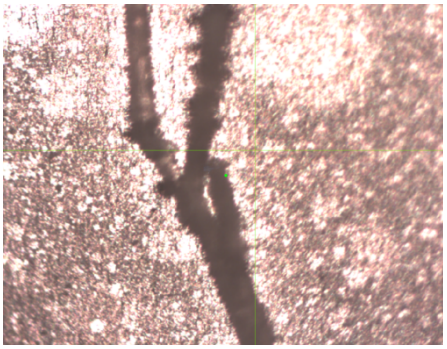

Figure 2. Raman image of the chitosan electrospun fibers

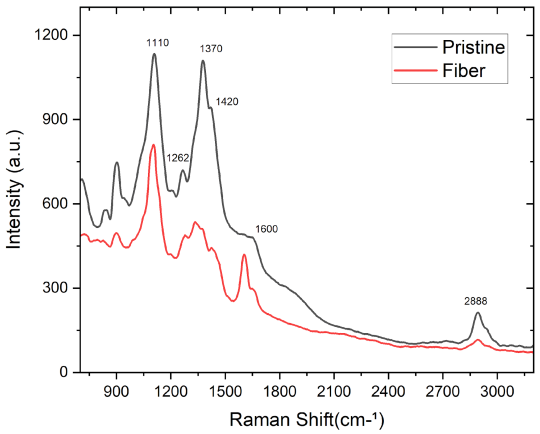

Figure 3. Raman spectra of the chitosan bulk and electrospun fiber excited with 785 nm laser.

Acta Microscopica Vol. 32, Supp. 1, 2023
Abstract Book NSSY 2023- Galapagos 23 -29 April, 2023

Fabrication of electrodes with MWCNTs-functionalized PVDF polymeric membranes to be applied on Microbial Fuel Cells.

León Ocaña (1), Jonathan Escorza (1), Yolanda Angulo (2), Carlos Reinoso (1).

(1)School of Physical Sciences and Nanotechnology, Yachay Experimental Technology Research University, Urcuquí-Ecuador. (2) Center for Nanoscience and Nanotechnology, Universidad de las Fuerzas Armadas ESPE, Sangolquí-Ecuador.
leon.ocana@yachaytech.edu.ec

The world's demand for electrical energy has been growing at an unprecedented rate over the past few decades[1]. With the rise of industrialization and urbanization, coupled with the rapid expansion of technology and population growth, the consumption of electricity has been increasing exponentially every year. This has led to a need for alternative sources of renewable energy that can keep up with the growing demand for power while reducing the reliance on non-renewable fossil fuels[2]. One promising solution to this problem is the use of Microbial Fuel Cells (MFCs) which have been shown to be capable of harvesting electrons produced by the bioelectrogenesis through biomass metabolism[3]. MFCs are an emerging technology that could revolutionize the way we generate electricity. The cells rely on the ability of certain microorganisms to generate an electric current as a byproduct of their metabolic processes. This current can be captured by electrodes placed in the cell, which then converts it into usable electrical power. This process has been increased by using special electrodes. In this research, we have produced electrodes based on polyvinylidene fluoride (PVDF) thin films, modified with multi-walled carbon nanotubes (MWCNTs) and used to coat stainless steel meshes. Electrochemical impedance analysis (EIS), cyclic voltammetry (CV), Raman spectroscopy were performed to study the electrodes. Characterization of the cyanobacterial voltage generation on a MFC and its culture media has been done. The preliminary results show a promising relationship between voltage generation, the concentration of MWCNTs, and the number of layers deposited in the mesh. These findings have contributed significant new insights in this field and have helped to build on the previous research regarding the fabrication of the membranes alone. The benefits of MFCs include their ability to use a wide variety of organic substrates, their low maintenance requirements, and their relatively simple design. In addition, MFCs are not subject to the same limitations as traditional power sources, such as wind and solar power, which are dependent on weather conditions. MFCs can operate continuously as long as they are provided with a constant supply of organic matter. Overall, this research has demonstrated the potential of MFCs as a viable alternative energy source, capable of producing electricity in a sustainable and environmentally friendly manner. Further research is needed to optimize the efficiency and scalability of MFCs, but the potential for this technology is immense. With continued investment and innovation, MFCs could play a key role in meeting the world's growing energy demands while reducing our carbon footprint and preserving our planet for future generations.

REFERENCES

[1] Khan, I., Hou, F., & Le, H. P. (2021). The impact of natural resources, energy consumption, and population growth on environmental quality: Fresh evidence from the United States of America. Science of the Total Environment, 754, 142222.
[2] Levenda, A. M., Behrsin, I., & Disano, F. (2021). Renewable energy for whom? A global systematic review of the environmental justice implications of renewable energy technologies. Energy Research & Social Science, 71, 101837.
[3] Obileke, K., Onyeaka, H., Meyer, E. L., & Nwokolo, N. (2021). Microbial fuel cells, a renewable energy technology for bio-electricity generation: A mini-review. Electrochemistry Communications, 125, 107003.

ACKNOWLEDGMENTS

Carlos Reinoso, Ph.D. Jonathan Escorza, Ms.C, and Yolanda Angulo, Ph.D. have been of fundamental aid in the completion and execution of this research for that this would not be possible.

FIGURES

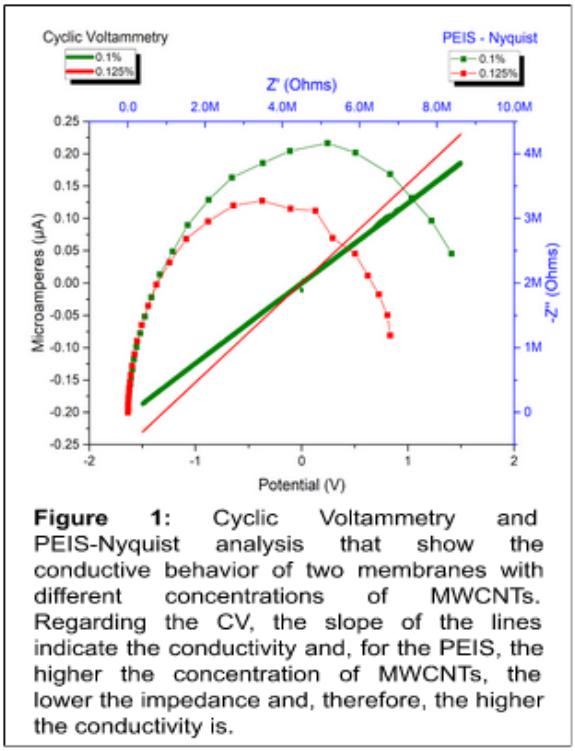

Figure 1: Cyclic Voltammetry and PEIS-Nyquist analysis that show the conductive behavior of two membranes with different concentrations of MWCNTs. Regarding the CV, the slope of the lines indicate the conductivity and, for the PEIS, the higher the concentration of MWCNTs, the lower the impedance and, therefore, the higher the conductivity is.

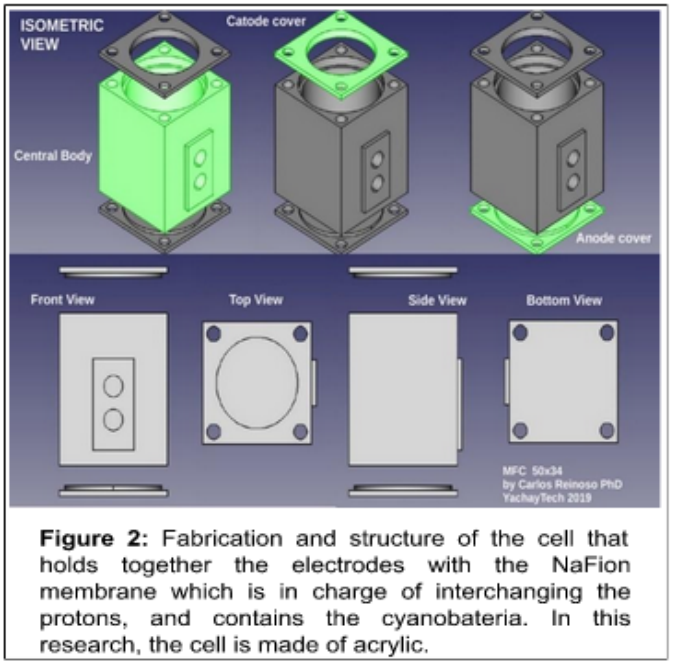

Figure 2: Fabrication and structure of the cell that holds together the electrodes with the NaFion membrane which is in charge of interchanging the protons, and contains the cyanobateria. In this research, the cell is made of acrylic.

Acta Microscopica Vol. 32, Supp. 1, 2023
Abstract Book NSSY 2023- Galapagos 23 -29 April, 2023

EXCITATION OF N2 MOLECULES AS A DENSITY MODIFIER: A THEORETHICAL APPROACH

Jean Villa (1), Thibault Terencio (1, 2)
(1) School of Chemistry and Engineering, YachayTech, 100119 Urcuquí . Ecuador. (2) CATS INVESTIGATION GROUP (CAtalysis Theory & Spectroscopy, YachayTech, 100119 Urcuquí . Ecuador)
jean.villa@yachaytech.edu.ec.com

Flying is an ancient dream of man since his origins. Despite the generation of air-pollution, planes are currently the adopted approach, but has been in competition with gas balloons throughout history, until the burning of a zeppelin in 1937 provoked by the main defect of this technology: use flammable hydrogen as lifting gas. Hence, this later technology was secluded during the coming years. The present work focuses on presenting an alternative, the analysis of changing micro-molecular properties of a N2 gas molecule as a starting point for the modification of macro-molecular properties of interest such as volume and density. The interest of this work arises from the need to acquire gas system with lower density than their non-modified ground state gas. For this case, N2 gas is considered since it is a source of wide availability around the world and can be used without limitations in an eco-friendly manner. Also, considering its applicability for flying purposes in airships, the results are contrasted with the typical employed source for the age of the airships. Specifically, by using TDDFT and MD calculations is proved that the excitation of fundamental state N2 molecules to higher electronic states increases the volume of the system and decrease the density of it at standard conditions. Furthermore, the introduction of additional physical and chemical parameters as temperature, mass, and ionic species of N2 provide additional information so as to evaluate their influence into the desired macro-properties.

REFERENCES

[1] Crouch, Tom (2004). Wings: A History of Aviation from Kites to the Space Age. New York, New York: W.W. Norton Co. ISBN 0-393-32620-9
[2] Lofthus, A.; Krupenie, P. H. The Spectrum of Molecular Nitrogen. J. Phys. Chem. Ref. Data 1977, 6 (1), 113ˆa307. https://doi.org/10.1063/1.555546.
[3] Gillan, C. J.; Tennyson, J.; McLaughlin, B. M.; Burke, P. G. Low-Energy Electron Impact Excitation of the Nitrogen Molecule: Optically Forbidden Transitions. J. Phys. B At. Mol. Opt. Phys. 1996, 29 (8), 1531ˆa1547. https://doi.org/10.1088/0953-4075/29/8/017.

FIGURES

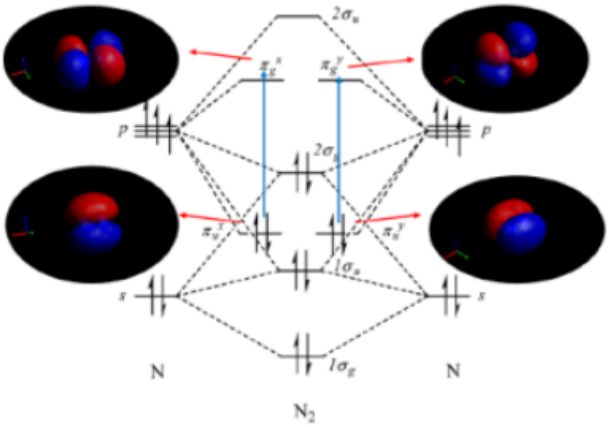

Figure1. MO diagram of N2 molecule with orbitals involved at the first excited state

Acta Microscopica Vol. 32, Supp. 1, 2023
Abstract Book NSSY 2023- Galapagos 23 -29 April, 2023

STRUCTURAL PROPERTIES IN BARIUM TITANATE USING MODIFIERS FOR PIEZOELECTRIC EFFECT

Carlos Mendoza-Ochoa (1), Gema González (1).

(1) Yachay Tech University, School of Physical Sciences & Nanotechnology, 100119-Urcuquí, Ecuador.
carlos.mendoza@yachaytech.edu.ec

Barium Titanate ($BaTiO_3$) is a perovskite considered as one of the most promising materials of the twenty-first century. Indeed, its $BaTiO_3$ structure is shown to be the single most versatile ceramic host [1]. In this context, the present research is focused on the study of Barium Titanate ($BaTiO_3$) perovskite structure using modifiers such as $CaCO_3$ and LiCl at 3wt%, 5wt%, and 7 wt% to analyze the change in phase transition at 700°C, 1000°C, and 1200°C temperatures. The research explain the behavior of Barium Titanate systems studying phase transitions by X-Ray Diffractometer and Scanning Electron Microscopy using Calcium Carbonate and Lithium Chloride as modifiers of each compound, and a Master-Mix which is the mixing between both modifiers at 700°C, 1000°C and 1200°C temperatures to find the stable structure of $BaTiO_3$ that would increase the generation of energy by piezoelectric mechanism for future research. The present research project has significant points detailed below. First, there exist changes in phases when the temperature increases from 700°C, 1000°C and 1200°C. For pure $BaTiO_3$ the structure system is cubic at 700°C, then at 1200°C the crystal structure change to a tetragonal system. However, when the temperature of sinterization increase to 1200°C there are coexisting three characteristics phases of $BaTIO_3$: Cubic, Tetragonal and Orthorhombic. From a structure point of view, for $BaTiO_3$ +(3% w.t and 7% w.t) LiCl the crystal structure is cubic at 700°C, 1000°C and 1200°C. However, only in at 700°C the structure parameters are the same in both system (3% w.t and 7% w.t) independently the concentration of LiCL in the structure. In addition, in both systems are coexisting three phases at 1200°C sinterization temperature. For $BaTiO_3$+ (3% w.t and 7% w.t) $CaCO_3$ the crystal structure, cell parameters and cell volume is the same in $BaTiO_3$+LiCl at 700°C. In the same way, there are coexisting Cubic, Tetragonal and Orthorhombic phases in the structure at 1200°C. For $BaTiO_3$+ (3% w.t and 7% w.t) LiCl + $CaCO_3$ the structure at 1200°C change to Trigonal (rhombohedral axes). Additionally, the cell parameters and cell volume at 700°C keep in a Cubic phase independent if it was a $BaTiO_3$ with LiCl or $CaCO_3$ or a mix of them. Considering porosity measurements, at of $BaTiO_3$ + 7%w.t (LiCl and $CaCO_3$) at 1200°C reduce significantly. It means that sinterization is good which makes the system suitable for future piezoelectric analysis. Nevertheless, considering only $BaTiO_3$ + 5%w.t (LiCl and CaCO3) the structure have less absorption of water, then a structure with minimum porosity and a better option for future piezoelectric analysis. Nowadays, multiples mechanisms for energy conversion had been developed through the last decades and since potentials strategies are implemented to provide a more effective use of Perovskite materials. BaTiO3 particular structure offers unique features such as extensive porous structures, large surface area and strong absorption. The present research, can inspire to create novel designs so that the piezoelectric effect could be utilized as the main source of energy. Future Outlook is realize piezoelectric characterization to obtain a sample with maximum piezoelectric property at low sinterization temperature for future energy-conversion devices.

REFERENCES

[1] Bhalla, A.; Guo, R.; Roy, R. The perovskite structure: a review of its role in ceramic science and technology. *Materials research innovations* 2000, *4*, 3–26.

ACKNOWLEDGMENTS

Thanks to Escuela Politecnica Nacional and Yachay Tech University from Ecuador.

FIGURES

1. X-Ray diffraction

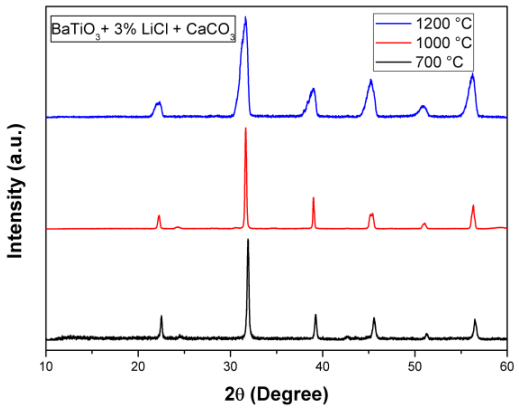

Fig. 1. X-Ray diffraction pattern of BaTiO3 + 3wt.% LiCl + 3wt.% CaCO3 from 10−60 2θ (Degree) at 700°C, 1000°C, and 1200°C

2. Porosity Measurement

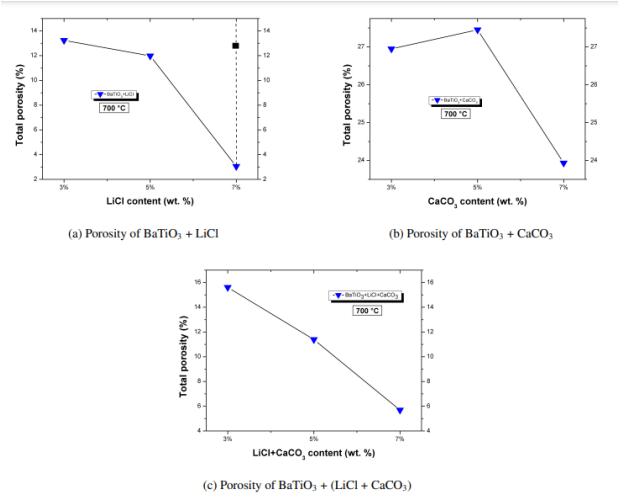

Porosity percentage of BaTiO3 with LiCl, CaCO3 and (LiCl+CaCO3) with 3%w., 5%wt, and 7%wt at 700°C

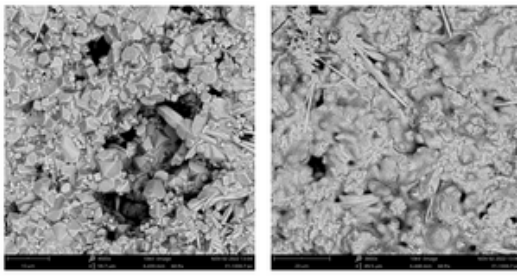

(a) **MAG: 4500x.** $BaTiO_3$ + LiCl (b) **MAG: 3000x.** $BaTiO_3$ + LiCl

Fig 3.1. BaTiO3 + 7%w.t LiCl at 1000°C

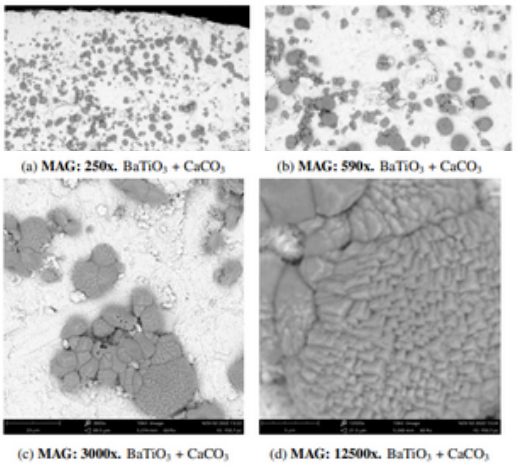

(a) **MAG: 250x.** $BaTiO_3$ + $CaCO_3$ (b) **MAG: 590x.** $BaTiO_3$ + $CaCO_3$

(c) **MAG: 3000x.** $BaTiO_3$ + $CaCO_3$ (d) **MAG: 12500x.** $BaTiO_3$ + $CaCO_3$

Fig.3.2. BaTiO3 + 7%w.t CaCO3 at 700°C

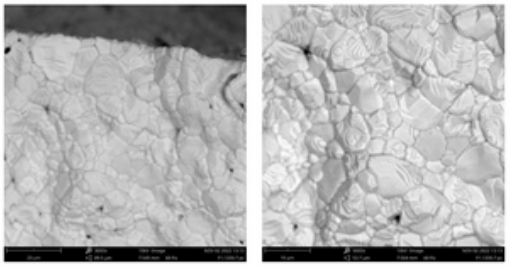

(a) **MAG: 3000x.** $BaTiO_3$ + LiCl (b) **MAG: 5000x.** $BaTiO_3$ + LiCl

Fig 3.3. BaTiO3 + 7%w.t LiCl at 1200°C

Acta Microscopica Vol. 32, Supp. 1, 2023
Abstract Book NSSY 2023- Galapagos 23 -29 April, 2023

USE OF POLY(VINYL ALCOHOL)-MALIC ACID HYDROGEL (CLPHMA) FOR QUANTITATIVE CAPTURE OF CARBOFURAN AND METHOMYL FROM AQUEOUS SOLUTIONS.

Marcelo Guerrero (1,2), Gustavo Carreño (3), Zoraya López Cabaña (1), Esteban F. Durán-Lara (2,4,5), Adolfo Marican (1,2,5).

(1) Instituto de Química de Recursos Naturales, Universidad de Talca, Talca 3460000, Maule, Chile. (2) Bio and NanoMaterials Lab, Drug Delivery and Controlled Release, Universidad de Talca, Talca 3460000, Maule, Chile. (3) Escuela de Pedagogías en Ciencias Naturales y Exactas, Facultad de Ciencias de la Educación, Universidad de Talca, Linares 3580000, Maule, Chile. (4) Departamento de Microbiología, Facultad de Ciencias de la Salud, Universidad de Talca, Talca 3460000, Maule, Chile. (5) Center for Nanomedicine, Diagnostic & Drug Development (ND3), Universidad de Talca, Talca 3460000, Maule, Chile.
amarican@utalca.cl

This study describes through Molecular dynamics simulations the interactions between two carbamate pesticides, Carbofuran (CFN) and Methomyl (MML), with PVA hydrogels cross-linked with malic acid (CLPHMAs) synthesized in our work group, for the quantitative capture of these insecticides and the remediation of aqueous solutions. These simulations correlate with experimental trials based on Design of Experiments (DoE), allowing the capture of CFN and MML in aqueous solutions of 500 mg L^{-1}, using a capture time of 10 min. In conclusion, both tools enhance each other, demonstrating that CLPHMAs can remove these pesticides, constituting a technological alternative for the treatment of contaminated water.

REFERENCES

[1] Ávila-Salas F. et al. *Nanomaterials* (2018) (8(1)) (23).
[2] Ávila-Salas F. et al. *Pharmaceutics* (2019) (11(9)) (447).
[3] Valdés O. et al. *J. Appl. Polym. Sci.* (2018) (135) (45964).

ACKNOWLEDGMENTS

M Guerrero, Z López Cabaña and A Marican thank Proyect FOVI210019 for funding. E Durán-Lara is grateful to Project Nº 1210476, Fondecyt Regular.

FIGURES

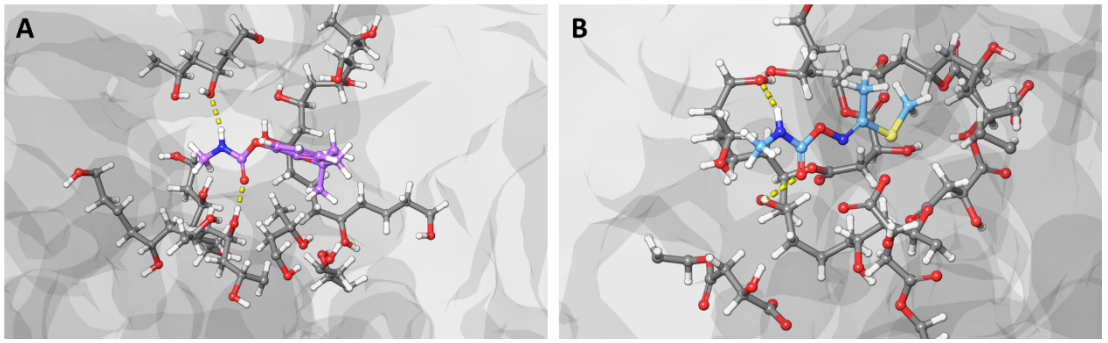

Figure 1. Hydrogen bond interactions between pesticides, CFN (A) and MML (B), and CLPHMA hydrogel. Carbon atoms of CFN are showed in purple and of MML in cyan.

Table 1. Capture of CFN and MML using optimal conditions: CLPHMA-33.1 and 10 min of capture.

Experiment	Remaining CFN in solution [mg/L]	CFN captured/CPLHMA [mg CFN/mg CLPHMA]	Remaining MML in solution [mg/L]	MML captured/CPLHMA [mg MML/mg CLPHMA]
1	0	0.0644	0	0.0644
2	0	0.0636	0	0.0636
3	3.58	0.0640	6.58	0.0636
Mean ± SD	1.19 ± 2.07	0.0640 ± 0.0004	2.19 ± 3.80	0.0639 ± 0.0005

Acta Microscopica Vol. 32, Supp. 1, 2023
Abstract Book NSSY 2023- Galapagos 23 -29 April, 2023

SYNTHESIS OF CARBON NANOTUBES USING A MIX OF IRON AND COBALT AND MAGNETITE AS CATALYST AND DECORATION WITH MAGNETITE.

Jose Pizha (1), Diana Heredia (2), Luis Corredor (1), Werner Bramer (1), Carlos Reinoso (1), Gema González (1).

(1) School of Physical Sciences and Nanotechnology, Yachay Tech University, Urcuquí, Ecuador. (2) School of Chemical Sciences and Engineering, Yachay Tech University, Urcuquí, Ecuador.
diana.heredia@yachatech.edu.ec

Recently Carbon nanotube (CNts) structures have aroused great interest among researchers due to their special features useful in different fields. However, their high stability and hydrophobicity make their use difficult. In order to fully exploit their potential, functionalization and decoration have been studied as methods to improve their physicochemical properties. The most used functionalization method is the acid treatment in which carboxyl and hydroxyl groups are attached to the CNts walls thanks to the formation of defects. Unfortunately, much of the material is lost in the tedious laboratory work that this process requires. Therefore, in the present work, we explored a different procedure to obtain CNts decorated with Magnetite nanoparticles (MagNPs). The proposed protocol does not need previous functionalization steps. Otherwise, this is one step procedure that uses MagNPs as a catalyst promoting the obtention of pristine magnetic CNts. The obtained composites were compared with other CNts also decorated with MagNPs but synthesized with traditional catalysts and under a typical functionalization process. In the experimental process, two samples of CNts were synthesized by the chemical vapor deposition method using MagNPs and a mix of Iron and Cobalt supported on calcium carbonate (FeCo/CaCO3) as catalysts. Both CNts underwent acid treatment to functionalize their walls. Finally, MagNPs were deposited via high-frequency ultrasound on the pristine CNts walls and functionalized CNts walls. In the end, six samples were obtained: pristine CNts, directly decorated CNts (CNts-Dec(Mag)), and functionalized and decorated CNts (CNts-Fun-Dec(Mag)).
These three samples were prepared in a separate way for the two catalysts MagNPs (-CNts) and eCo/CaCO3 (-CNts). The characterization results with XRD shows the diffractograms in which the crystallographic planes (002) and (110) correspond to the graphitic layered structure of CNTs. In the decorated samples the intensity of the (002) peak is noticeably reduced, which comes from an internal change of material. In this case, a loss of crystallinity could be the reason, which is necessary for an adequate decoration process. The star peaks are common for the decorated samples and correspond to the face-centered cubic structure of MagNPs. Raman Spectroscopy showed (see Fig 1) the RBM signal and the G, D, and 2D bands, indicating the presence of single and Multiwalled CNts. The intensity ratio of the D/G bands for both /-CNts increases after the decoration process. This change is attributed to the presence of more defects at the surface of CNts. The XPS analysis (see Fig 3) over /-CNts-Fun-Dec(Mag) samples shows the C1s, O1s, and Fe2p peaks that appear in the Mag/CNts composites. Part b details the decomposition of the Fe2p peak in Fe2p1/2 and Fe2p3/2. The Fe2p3/2 peak after the deconvolution shows signals for Fe2+ and Fe3+ mixed oxide, i.e., Fe3O4. In part C, the C1s peak was deconvoluted obtaining: C–O/C=O, C-OH, C=O, and HO–C=O. These findings reveal the existence of functional groups over the composites. Part d shows the deconvolution of O1s: C-O, C=O, and Fe-O. The latter confirms the decoration of MagNPs on CNts surface. The microanalysis confirms the results obtained in the previous characterization techniques. Moreover, these analyses suggest two types of decorated results, one inside and the other in the walls. The inside decoration is complicated to obtain, though surprisingly -CNts are mostly decorated in this way (see Fig 2). The magnetic properties of the samples are summarized in Table 1. The coercivity value of -CNts is the highest due to the strong influence of Fe and Co elements from the catalyst. For the functionalization samples all magnetic properties low because the acid treatment cleans the catalyst particles. The direct decoration process improves the maximum magnetization and the remanence response which is useful for switching systems (see Fig 4). The final composite material from both /-CNts was successfully decorated with MagNPs through of direct and functionalized decoration processes. Thanks, the final properties of the composites they can be used for several applications such as switching systems, high and soft magnetic response materials, among others.

REFERENCES

[1] Fallah-Shojaei A. et al. RSC Adv. (2014) (4) (19).
[2] Mishra A. and S. Ramaprabhu. J. Phys. Chem. C. (2010) (114) (6).
[3] Zhi-Feng Y. et al. J. Taiwan Inst Chem Eng. (2018) (82).

ACKNOWLEDGMENTS

We acknowledge Zailmar Morales for her help taking the XRD patterns.

FIGURES

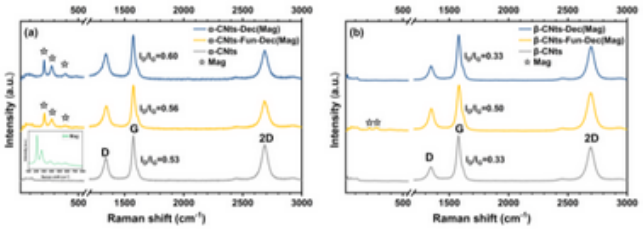

Fig 2: Raman spectra for the samples. The stars show the peaks corresponding to MagNPs. The insert figure in a is the diffractogram for MagNPs.

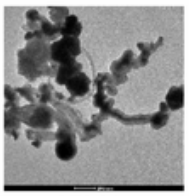

Fig 1: SEM imagen of α-CNts -Dec(Mag)

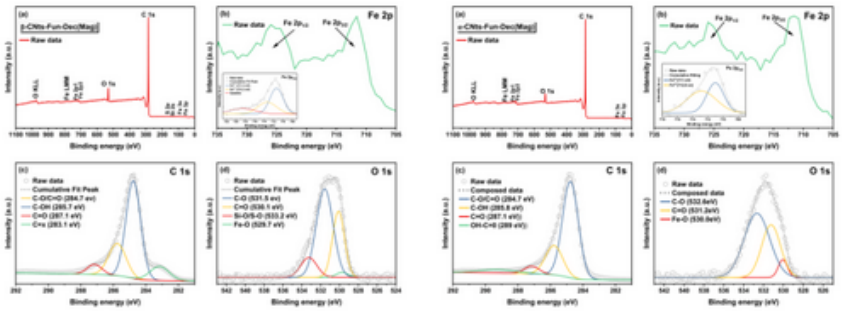

Fig 3: XPS spectra for the α/β-CNts-Fun-Dec(Mag) samples. The raw data is in part a. The deconvolution of Fe 2p peak is in b part. The deconvolution of C 1s peak is in c part. The deconvolution of O 1s peak is in d part.

Table 1: VSM measurements results

Sample	Coercivity (Oe)	Remanence (emu/g)	Mmax (emu/g)
α-CNts	252.3 ± 0.1	2.9 ± 0.1	35.8 ± 0.1
α-CNts-Fun-Dec(Mag)	196.8 ± 0.1	1.5 ± 0.1	8.4 ± 0.1
α-CNts-Dec(Mag)	139.0 ± 0.1	4.2 ± 0.1	41.4 ± 0.1
β-CNts	883.9 ± 0.1	2.1 ± 0.1	6.1 ± 0.1
β-CNts-Fun-Dec(Mag)	170.0 ± 0.1	2.1 ± 0.1	11.6 ± 0.1
β-CNts-Dec(Mag)	173.0 ± 0.1	4.9 ± 0.1	27.0 ± 0.1

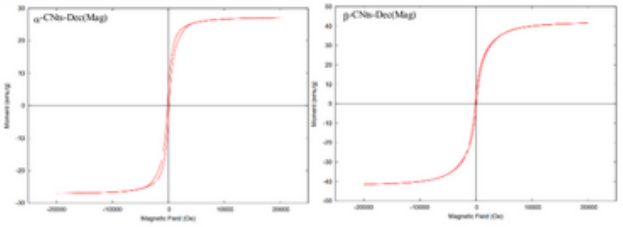

Fig 4: Magnetic hysteresis loop for α/β-CNts-Dec(Mag) samples.

Acta Microscopica Vol. 32, Supp. 1, 2023
Abstract Book NSSY 2023- Galapagos 23 -29 April, 2023

GROWTH OF LMO THIN FILMS ON FLAT SUBSTRATES THROUGH ELECTRON BEAM DEPOSITION

Vinicio Cevallos (1), Cristian Olguín (2), Vicente Díaz (3), Marcos Flores (4).
(1)Department of Physical Sciences and Nanotechnology, Yachay Tech University, Urcuquí, Ecuador
(2) Physics Department, Universidad Santiago de Chile, Santiago, Chile
(3) Laboratory of Surfaces and Nanomaterials, Physics Department, Universidad de Chile, Santiago, Chile.
(4) Laboratory of Surfaces and Nanomaterials, Physics Department, Universidad de Chile, Santiago, Chile.
vinicio.cevallos@yachaytech.edu.ec

Transition metal oxides (TMOs) are a type of inorganic compounds which have received great attention in recent years due to their unique physical and chemical properties. One specific type of transition metal oxide which has garnered significant interest is lithium manganese oxide (LMO). LMO was deeply studied due to its electrochemical properties; these characteristics are relevant for applications in Lithium-Ion Batteries (LIBs). In this work, LMO thin films were deposited on flat substrates through electron beam evaporation technique. Fractal properties of LMO films grown on silicon dioxide (SiO2) wafers were studied using the theory of Dynamic Scaling. First, SiO2 wafers were cleaned using compressed air before being introduced to electron gun equipment. Different thicknesses of LMO thin films were evaporated (0.88 nm, 1.76 nm, 2.63 nm and 3.51 nm) on SiO2 wafers with a voltage of 8.16 kV and a current of 20 mA at high vacuum conditions. The topography of the LMO thin films was captured by Atomic Force Microscopy (AFM) images for analyzing the layer growth on the substrate. At 0.88 nm of thickness, LMO grain growth forms separated islands on the flat surface. Then, at 1.76 nm of thickness; the layer shows a subsequent growth of grains, the islands on the surface grow closer between them and the difference of their heights is lower than 0.88 nm islands. After, at 2.63 nm of thickness, a low difference in heights of grains is shown, it could be due to the LMO evaporation covering all the substrate surface, and at 3.51 nm, a smooth surface is shown with a difference in heights lower in comparison to the previous analyzed thicknesses, this phenomenon is shown in figure 1. Using the Radial autocorrelation function, we obtained the interface width(RMS) and correlation length for analyzing the correlation of surface height separated laterally by a vector r (Fig. 2). The roughness of the layers decreases in function to the thickness: at 0.88 nm and 2.63nm of thickness, the roughness is the highest and lowest respectively, as it is shown in the figure 3, It agrees with the difference in height and softness of the AFM image. In addition, Radial power spectral functions were used to analyze Fourier transform of the surface heights obtaining the roughness exponent α (Fig.4). It shows a α increment when material deposition increases too. Nevertheless, at 2.63 nm the roughness exponent decreased as it is shown in figure 5. In conclusion, the growth behavior of LMO thin films on silicon dioxide by physical evaporation consists in the formation and subsequent growth of grains thateventually cover most of the substrate. The RMS roughness decreases, which indicates that the surface is smoothed as more material is deposited. The roughness exponent allows the characterization of the texture of the surface. In fact, if the exponent α has values over 1 indicates the presence of super-roughness and anomalous dynamic scaling, which is usually found in nonequilibrium growth models. It is suspected that the first layers of LMO cover the silicon dioxide substrate, and then the structures start growing on top (Stranski-Krastanov growth mode). Further analysis is needed to determine the film growth mode at the initial stages of deposition on the substrate.

REFERENCES

[1] Ruffino, F., Grimaldi, M. G., Giannazzo, F., Roccaforte, F., & Raineri, V. (2009). Atomic force microscopy study of the kinetic roughening in nanostructured gold films on SiO2. Nanoscale research letters, 4(3), 262-268.
[2] Pelliccione, M., & Lu, T. M. (2008). Evolution of thin film morphology (Vol. 108). New York: Springer New York.
[3] Barabási, A. L., & Stanley, H. E. (1995). Fractal concepts in surface growth. Cambridge university press.

ACKNOWLEDGMENTS

This work has been supported by Agencia Nacional de Investigación y Desarrollo (ANID) FONDECYT project N° 1191799, Millennium Nucleus MultiMat, and Department of Physics and the Lab of Surface and Nanomaterials, Universidad de Chile.

FIGURES

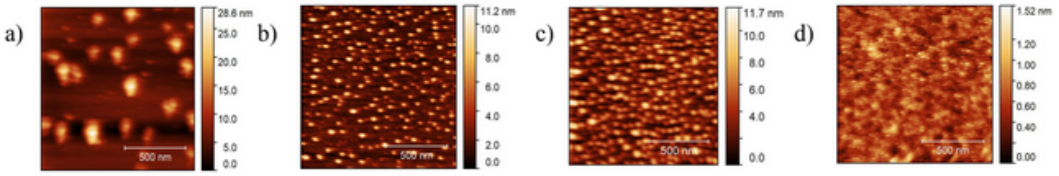

Fig 1. AFM image order by deposition of substrate. The deposition of a) 0.88 nm, b) 1.76 nm, c) 2.63 nm and d) 3.51 nm.

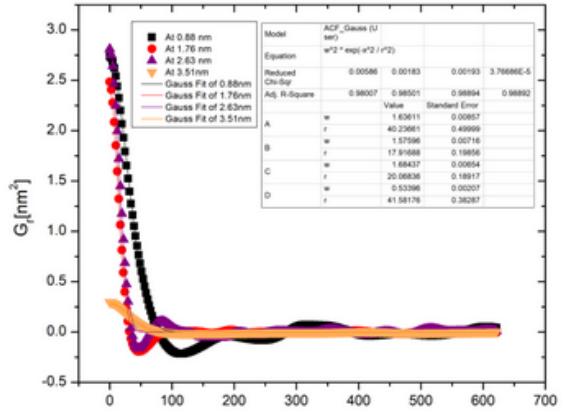

Fig 2. *Radial autocorrelation function. The fitted function allows to obtain interface width and correlation length.*

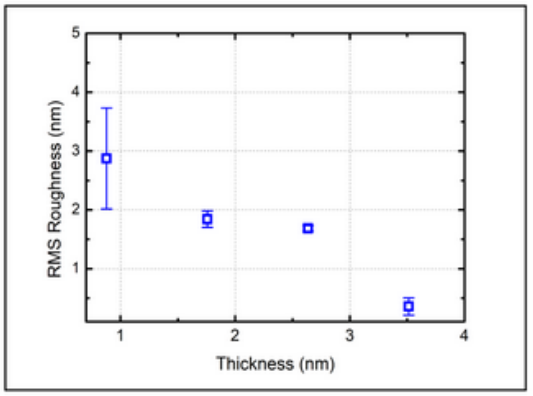

Fig 3. Mean RMS roughness (also known as "interface width") of each deposition thickness..

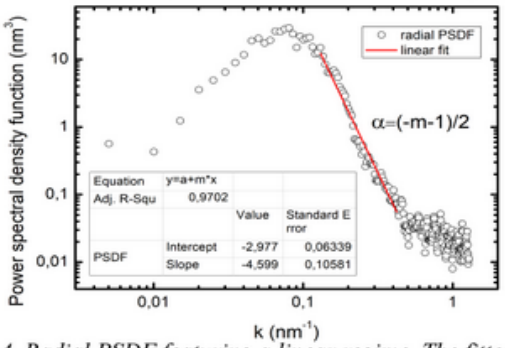

Fig 4. Radial PSDF featuring a linear regime. The fitted function allows us to obtain the roughness exponent.

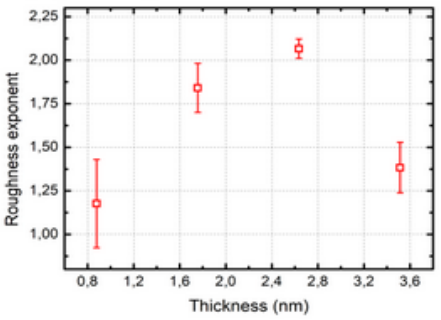

Fig 5. Roughness exponent of each deposition thickness.

Acta Microscopica Vol. 32, Supp. 1, 2023
Abstract Book NSSY 2023- Galapagos 23 -29 April, 2023

COMPUTATIONAL STUDIES OF NOVEL UIO-66-BASED MOF: STABILITY, ELECTRONIC STRUCTURE AND DEFECTS

Nicole P. Guerrero (1), Alicja Mikolajczyk (2), Henry P. Pinto (1)

(1) CompNano Research Group. School of Physical Science and Nanotechnology, YachayTech University. Urcuqui-Ecuador
(2) Faculty of Chemestry, University of Gdansk, Gdansk-Poland
nicole.guerrero@yachaytech.edu.ec

Metal-organic frameworks (MOF) are promising materials that have been widely studied due to their interesting morphological properties, such as high specific surface area and high porosity. Important properties of MOFs are based on various combinations of metal nodes and organic linkers. This feature increases research interest in applications related to solar energy harvesting, absorption, catalysis, separation, and sensing [1]. In a world where technology develops according to society's needs, these materials provide an opportunity for research and development in areas of interest, such as energy resources and the decomposition of greenhouse gasses. In order to study a promising metal-organic framework for photovoltaic applications, some researchers collect information from the reported bandgap and make a comparison with metal ion variation and/or organic/conjugation linker. The UiO66 zirconium-based MOF was one of the promising materials among those reviewed, with an average bandgap of 2.20-3.10eV [1]. Then, we propose a modification of the metallic node to the zirconium-based MOF UiO-66 with Cerium and Titanium to obtain suitable material for photovoltaic and/or photocatalytic applications; in this study, we also investigate the effect of structural defects on the electronic properties. Investigations on MOF report the close dependence between the ligand center and the transfer through the metal-linker interaction when determining the bandgap [1]. This bandgap is the crucial parameter and establishes the light-harvesting window, which according to the Shockley-Queisser limit, E_g must be between 1-2eV [2] to be a material with potential applications in photovoltaics. We performed ab initio density-functional theory calculations with r2SCAN and HSE06 functionals; we analyzed the stability of the structures using machine learning and molecular dynamics. The calculations yield properties of MOFs with volumes of 2054.99 and 2512.27 $Å^3$ and compressibility modulus of 0.3644 and 0.2984 GPa for UiO66-Ti and UiO66-Ce, respectively. Bandgap values were also obtained: 3.72 eV for UiO66-Ti and 2.78 eV for UiO66-Ce. These computed values indicate the high specific surface area and their mechanical softness. In addition, when analyzing the density and partial density of states, the dependence on the metal-linker transfer is evident since, in the valence band, the main contribution comes from carbon and oxygen, elements that make up the linker, while in the conduction band, the main character comes from metal; either Ti or Ce. These studies also consider UiO66 with a mixture of Ce and Ti in the same MOF and structures with defects on the organic linker. The results are discussed in light of the available experimental data.

REFERENCES

[1] B. R. Sutherland, Solar materials find their band gap, Joule 4, 984 (2020).
[2] C.-C. Chueh, C.-I. Chen, Y.-A. Su, H. Konnerth, Y.-J. Gu, C.-W. Kung, and K. C.-W. Wu, Harnessing mof materials in photovoltaic devices: recent advances, challenges, and perspectives, J. Mater. Chem. A 7, 17079 (2019)

ACKNOWLEDGMENTS

We would like to thanks the support of the School of Physical Science and Nanotechnology at Yachaytech University. We also thank the generous computational time from Task Supercomputer Center in Gdańsk, Poland.

FIGURES

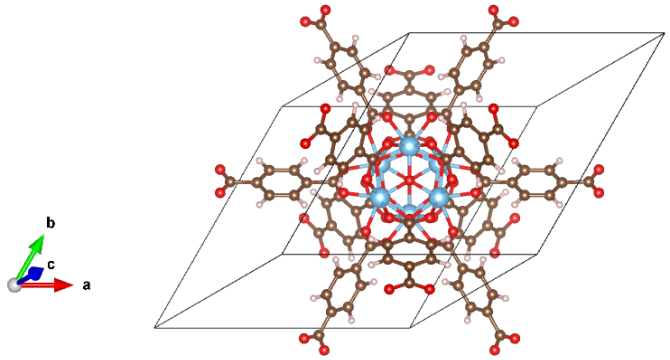

Figure 1: UiO66-Ti structure seeing with VESTA visualizer. In the center of the structure can be seen the metal cluster of titanium (blue spheres) and the linker.

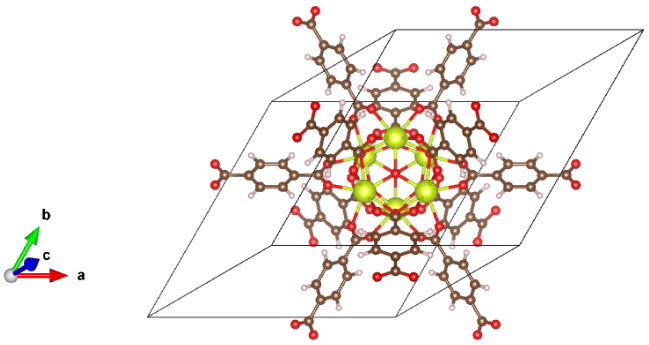

Figure 2: UiO66-Ce structure visualized in VESTA. The metal cluster is located at the center and the yellow spheres indicate the Ce metal.

Acta Microscopica Vol. 32, Supp. 1, 2023
Abstract Book NSSY 2023- Galapagos 23 -29 April, 2023

Computational studies of MOF Cu2(CO2)4 + ditopic carboxylate linker: stability and electronic structure

Eder Vera-Guzmán*1 , Henry P. Pinto1
1 CompNano Research Group, School of Physical Sciences and Nanotechnology,

Yachay Tech University, 100119, Urcuquí, Ecuador *
eder.vera@yachaytech.edu.ec

Metal-organic frameworks (MOFs) are the result of linking metal ions or clusters, also called secondary building units (SBUs), with organic linkers. The flexibility on their geometry, size and functionality has allowed a vast landscape of materials with modular properties, sharing however one similarity: crystalline structures with a typical porosity of greater than 50% of the total volume1. Consequently, MOFs evidence large surface area values which makes them a good candidate for fuel storage, carbon capture and storage (CCS), water harvesting as well as catalysis applications234. The approach to modelling MOFs can either be molecular or as extended periodic solids. A well-known extended solid approach is density functional theory (DFT). When using DFT, we cannot apply local spin density approximations (LSDA) functionals to MOFs since these assume a homogenous distribution of electrons throughout the material. Rather, the meta-generalized gradient approximation (meta-GGA) is a better option to these systems5. Calculations reported here are done using state of the art meta-GGA functionals: r2SCAN + rVV10 and for a more exact calculation of the electronic structure and band gap we would use the hybrid functionals, in this case, HSE06. In this work, we study the electronic band structure of two different crystal structures, shown in figure 3, formed by the secondary building unit (SBU), Cu2(CO4)2 and the organic linker, bis(3,4 dimethylphenyl)diazene. We also report the Birch-Murnaghan isothermal equation of state (EOS, to find out the optimal volume of the MOF) and the density of states (DOS) of the both structures. Moreover, we introduce magnetic order to the crystal structure to analyze variations in stability. Finally, we analyze defects on the structure as well as variations such as interchanging one methyl group with an element from the halogen family. All of this to decide which structure is more stable to synthetize for photocatalysis applications. We first start by constructing the linker and the SBU, after that the crystal structure is built figure 3. Before performing calculations with VASP, a first energy relaxation is done using density functional tight binding DFTB+. Later, an energy cut off convergence is performed using the meta-GGA functional for better precision5. After that, we calculate the total volume energy of the crystal for a given range to obtain the equation of state. We proceeded by calculatin the density of states now with hybrid functionals since they represent the minimum level of theory necessary to describe the electronic structure of systems where correlation and exchange play a major role in the electronic structure. This is particularly pertinent in MOFs containing spin-polarized transition metals6 , where exchange interactions not only play an important role in the energy of the material, but also define the band gap and the nature of the orbitals/bands. Furthermore, the values reported for the vacuum level are obtained using VESTA following the procedure of Keith Butler and its materials science group7. All results presented in this section belong to the second crystal structure shown in figure 3. Figure 2 shows the Birch-Murnaghan isothermal equation of state for the cases of different magnetic orders of the same crystal structure. The convergence in cutoff energy, which is a necessary value for VASP calculations, is shown in figure 1 at ENCUT = 850 eV. The equation of states shown in figure 2 indicate the most stable configuration corresponds to an antiferromagnetic order. The density of states of the four configurations is shown in figure 4.

REFERENCES

[1] Hiroyasu Furukawa, Kyle E Cordova, Michael Oaˆ Keeffe, and Omar M Yaghi. The chemistry and applications of metal-organic frameworks. Science, 341(6149):1230444, 2013.
[2] Jenna L Mancuso, Austin M Mroz, Khoa N Le, and Christopher H Hendon. Electronic structure modeling of metal–organic frameworks. Chemical reviews, 120(16):8641–8715, 2020.
[3] Allison RM Silva, Jeferson YNH Alexandre, Jos e ES Souza, Jose G Lima Neto, Paulo G de Sousa Ju´ nior, Maria VP Rocha, and Jos´ e CS Dos Santos. The chemistry´ and applications of metal–organic frameworks (mofs) as industrial enzyme immobilization systems. Molecules, 27(14):4529, 2022.
[4] Lars O hrstro ¨ m and Francoise M A ¨ mombo Noa. An im- proved water-harvesting cycle. Science, 374(6566):402–402, 2021.
[5] James W Furness, Aaron D Kaplan, Jinliang Ning, John P Perdew, and Jianwei Sun. Construction of meta-gga functionals through restoration of exact constraint adherence to regularized scan functionals. The Journal of Chemical Physics, 156(3):034109, 2022.
[6] Patanachai Janthon, Sijie Luo, Sergey M Kozlov, Francesc Vines, Jumras Limtrakul, Donald G Truhlar, and Francesc Illas. Bulk properties of transition metals: a challenge for the design of universal density functionals. Journal of chemical theory and computation, 10(9):3832–3839, 2014.
[7] Keith T Butler, Christopher H Hendon, and Aron Walsh. Electronic chemical potentials of porous metal–organic frameworks. Journal of the American Chemical Society, 136(7):2703–2706, 2014.

FIGURES

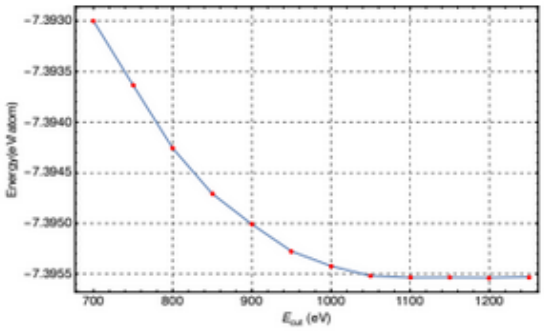

Figure 1 Shows the cut off energy convergence. We conclude using ENCUT = 850 eV.

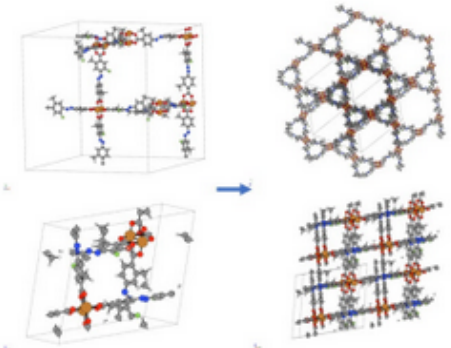

Figure 3 Shows the equation of states for the different magnetic orders.

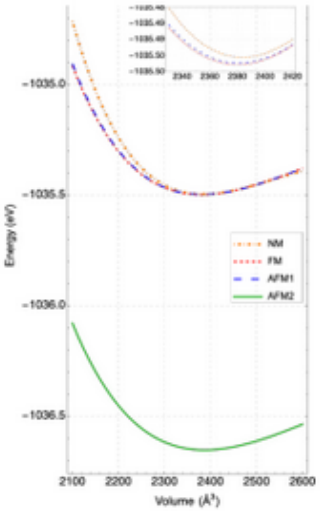

Figure 2 Shows two different crystal structures with the same SBU and organic linker.

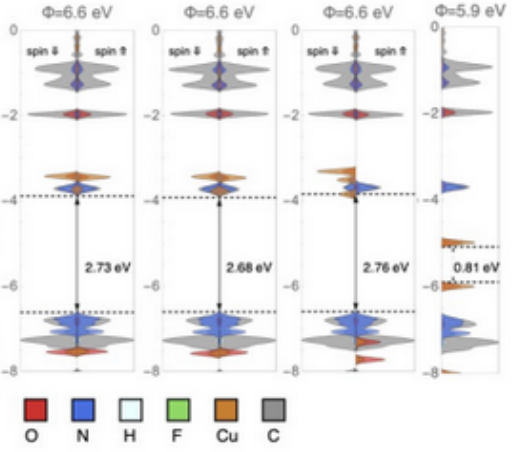

Figure 4 Shows the density of states for the different struc- tures, from left to right: AFM2, AFM1, FM, NM. Bandgaps of the electronic structure is also shown.

Acta Microscopica Vol. 32, Supp. 1, 2023
Abstract Book NSSY 2023- Galapagos 23 -29 April, 2023

FIRST PRINCIPLES STUDIES OF NOBLE METAL (Au, Ag, Pt, Pd) MULTICOMPONENT

Melanie A. Cedeno (1), Alicja Mikołajczyk (2), Henry P. Pinto (3)

(1,3) CompNano Group, School of Physical Sciences and Nanotechnology, Yachay Tech, 100119 Urcuquí, Ecuador. (2) Laboratory of Environmental Chemometrics,University of Gdańsk, Gdańsk 80-308, Poland.

Email: melanie.cedeno@yachaytech.ed.ec

Semiconductor photocatalysts are promising materials for diverse applications ranging from the removal of pollutants to energy conversion. In particular, TiO_2-based Nanomaterials have gained great interest in the field of photocatalytic materials due to their physical and chemical properties; therefore, theoretical and computational studies of the energetic descriptors are crucial to understanding the photocatalytic mechanisms involved. Although some research related to the interaction of single metal clusters with TiO_2 Anatase (101) has been performed[1], computational studies of nanoclusters of heterogeneous nature with this surface are limited. In previous research conducted by Malankowska et al [2], multicomponent noble metal clusters (Au, Ag, Pt, and Pd) of different mol% supported on a TiO2 surface have been experimentally synthesized. In the present work, we analyze the electronic structure and adsorption properties of noble metal multicomponent clusters and their interaction with Anatase TiO2(101) surface by using a cutting-edge combination of ab-initio Density Functional Theory (DFT) and Machine Learning (ML). We aim to simulate systems with single and multicomponent clusters of noble metals (Au, Ag, Pd, Pt) at different mol%(0.1, 0.25, 0.5, 1.25, 1.5, 2.5, 4.5, 6.5), considering oxygen surface vacancies and their influence on the stability of the systems. These calculations employ state-of-the-art functionals like METAGGA r2SCAN combined with a non-local van der Waals density functional rVV10 that accounts for dispersion interactions. Moreover, the known limitation of the band gap underestimation in DFT will be addressed using Hubbard-U corrections (DFT+U, within Dudarev's approach) for Ti-3d electrons. In order to perform ab-initio molecular dynamics simulations and overcome the size limitation and simulation times, ML force fields[3] are also considered. The structure for Anatase (101) TiO_2 was modeled with 3 O-Ti-O layers, using a cut-off energy of 700 eV (with a total energy convergence of <1meV/atom) and a Hubbard-U parameter of 5.15 eV. Several values of the U parameter were tested to find a correction value that allows obtaining a band gap similar to the value reported experimentally (3.2 eV), as seen in Table 1. The resulting supercell c(2x5) consists of 396 atoms and a vacuum space of 20Å. Subsequently, multicomponent clusters were integrated into the TiO_2 surface, and the partial density of states/PDOS, fermi level, conduction band, and valence band were determined. Different configurations consisting of metallic, bi-, tri-, and tetra-metallic clusters are depicted in Figures 1 1.1-1-4 and 2. First principle calculations performed in this study are useful to deepen the existing knowledge on the pathways of photocatalytic and adsorption processes, support experimental available data and provide a practical basis for further simulation-based experimental data multiplication studies for the sustainable design of new multicomponent photocatalysts.

REFERENCES

[1] Mikolajczyk, A.; Pinto, H. P.; Gajewicz, A.; Puzyn, T.; Leszczynski, J. Ab Initio Studies of Anatase TiO2 (101) Surface-Supported Au8 Clusters. *Curr. Top. Med. Chem.*, **2015**, *15* (18), 1859–1867. https://doi.org/10.2174/1568026615666150506151826.

[2] Malankowska, A.; Mikołajczyk, A.; Mędrzycka, J.; Wysocka, I.; Nowaczyk, G.; Jarek, M.; Puzyn, T.; Mulkiewicz, E. The Effect of Ag, Au, Pt, and Pd on the Surface Properties, Photocatalytic Activity and Toxicity of Multicomponent TiO_2 -Based Nanomaterials. *Environ. Sci. Nano*, **2020**, *7* (11), 3557–3574. https://doi.org/10.1039/D0EN00580K.

[3] Botu, V.; Batra, R.; Chapman, J.; Ramprasad, R. Machine Learning Force Fields: Construction, Validation, and Outlook. *J. Phys. Chem. C*, **2017**, *121* (1), 511–522. https://doi.org/10.1021/acs.jpcc.6b10908.

ACKNOWLEDGMENTS

We would like to thank the support of the School of Physical Sciences and Nanotechnology at Yachay Tech University. We also express our gratitude to the Task Supercomputer Center in Gdańsk (Poland) for providing us with the computing facilities necessary to carry out this research.

u	V_0(Å^3)	B_0(GPa)	B_0'	Fermi Level (eV)	Band Gap (eV)
0	68.5609	187.756	2.358	1.759	2.491
1	69.1982	185.331	2.365	1.751	2.589
2	69.8397	183.578	2.471	1.742	2.718
3	70.4947	182.464	2.437	1.725	2.885
4	71.1587	180.919	2.429	1.707	3.053
5	71.8259	179.754	2.404	1.702	3.178
6	72.5017	177.823	2.430	1.692	3.338
7	73.1700	176.649	2.478	1.682	3.528
5.15	71.9247	179.039	2.490	1.704	3.206

Table 1. Optimal Volume (V_0), Bulk Modulus (B_0), Fermi level, and Band Gap for TiO_2 with Hubbard correction U=1-7.

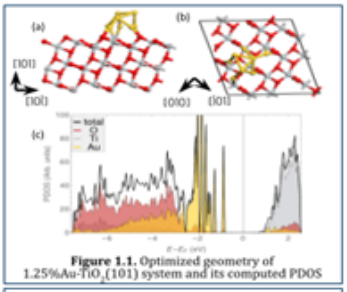

Figure 1.1. Optimized geometry of 1.25%Au-TiO_2(101) system and its computed PDOS

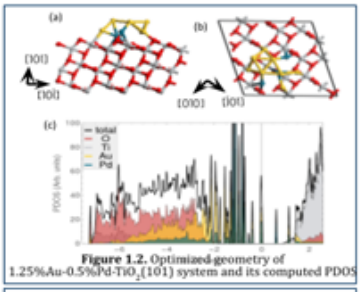

Figure 1.2. Optimized geometry of 1.25%Au-0.5%Pd-TiO_2(101) system and its computed PDOS

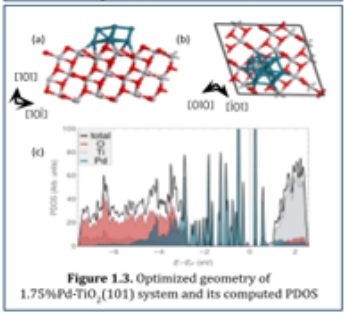

Figure 1.3. Optimized geometry of 1.75%Pd-TiO_2(101) system and its computed PDOS

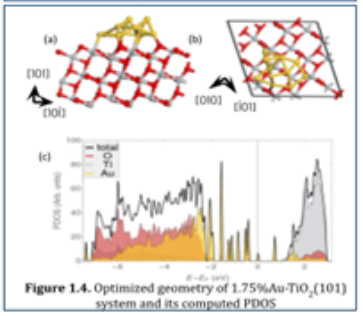

Figure 1.4. Optimized geometry of 1.75%Au-TiO_2(101) system and its computed PDOS

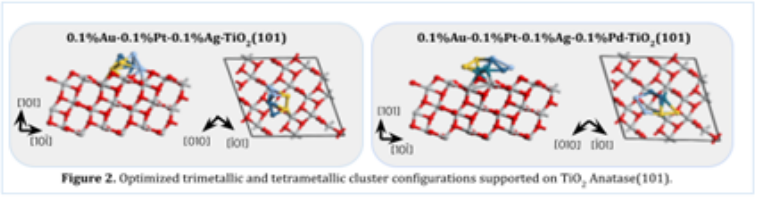

Figure 2. Optimized trimetallic and tetrametallic cluster configurations supported on TiO_2 Anatase(101).

OPTICAL PROPERTIES OF EUROPIUM SUBSTITUTED HYDROXYAPATITE.

María Fernanda Vega-Zerpa (1), Sarah Briceño (1), Luis Borrero (2), Gema González (1).

(1) School of Physical Sciences and Nanotechnology, Yachay Tech University, Urcuquí, Imbabura 100115, Ecuador.
(2) Pontificia Universidad Católica del Ecuador, Quito, Pichincha, Ecuador.
maria.vega@yachaytech.edu.ec

Hydroxyapatite (HA, Ca10(PO4)6(OH)2) is a biomineral nanostructure found in human hard tissues, with excellent properties such as biocompatibility, non-toxicity, luminescence, fluorescence, etc. HA improves its luminescent properties when its calcium atoms are replaced by europium atoms, since europium has a simple electronic energy level scheme, hypersensitive transitions and an ionic radius similar to calcium. Therefore, the synthesis of hydroxyapatite with the substitution of its calcium atoms by europium atoms, which is a biocompatible and luminescent nanomaterial, is proposed. For the synthesis of this nanomaterial, the hydrothermal method was used, and with characterization methods such as FTIR, EDS, XRD, PL and Raman Spectroscopy, it was determined that the synthesis was successfully achieved. Finally, a nanomaterial was obtained that can be applied as labeling material, drug delivery, bioimaging, etc. For the synthesis of hydroxyapatite the hydrothermal method was used with an ideal calcium to phosphate ratio of Ca/P = 1.67 (Figure 1a). This ratio was maintained for europium substitution (Ca+Eu)/P=1.67, for different concentrations of Eu (0-2)%. As the concentration of europium increases, the luminescence changes from a blue-violet color (~400nm) to yellow-reddish colors (~600-700 nm), figure 1b. Demonstrating successful doping, since according to theory the luminescence of europium is known to be red. In addition, in FTIR, the peaks of the (PO4)3- vibrational modes characteristic of HA attenuate as the Eu3+ concentration increases (Fig. 2a). On the other hand, HA:15%Eu has the highest PL intensity, being 15% the optimum concentration (Fig. 2b). EDX shows the presence of europium for both concentrations. Finally, BSE shows that the hydrothermal synthesis generated microparticles with regular morphology (50µm-350µm). The obtained results demonstrate that the hydrothermal method was successful for the synthesis of HA:Eu. Thus, it is possible to obtain a biocompatible and luminescent material for future applications in medicine.

REFERENCES

[1] Yang, P.; Quan, Z.; Li, C.; Kang, X.; Lian, H.; Lin, J. Bioactive, luminescent and mesoporous europium-doped
hydroxyapatite as a drug carrier. Biomaterials 2008, 29, 4341-4347.
[2] Xuan, T. C.; Trung, N. N.; Pham, V. H. Comparative characterization of microstructure and luminescence of europium
doped hydroxyapatite nanoparticles via coprecipitation and hydrothermal method. Optik 2015, 126, 5019-5021.
[3] Ciobanu, C. S.; Iconaru, S. L.; Massuyeau, F.; Constantin, L. V.; Costescu, A.; Predoi, D. Synthesis, structure, and
luminescent properties of europium-doped hydroxyapatite nanocrystalline powders. Journal of Nanomaterials 2012, 2012.

ACKNOWLEDGMENTS

The realization of this experimental work, my thesis to obtain the degree of Physicist, would not have been possible without the support, motivation, and knowledge of my tutors, professors Gema, Sarah, and Luis. I thank them for their patience, willingness, time, and appreciation. Working with them and seeing their passion for what they do has been a beautiful experience, which has inspired me to follow in their footsteps as a future researcher.

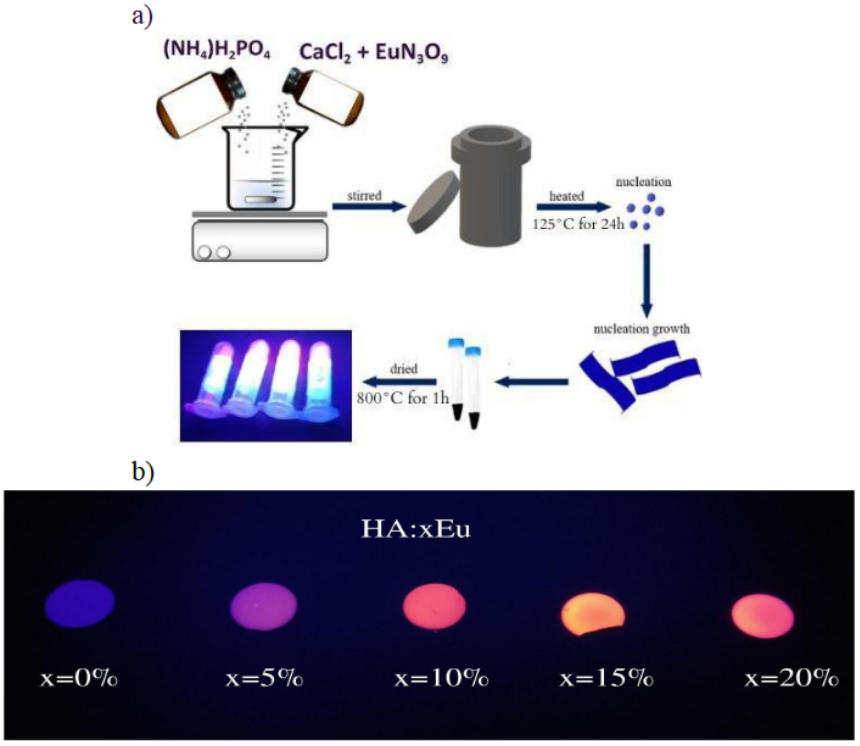

Fig 1. a) Step-by-step diagram of hydrothermal method. b) HA:xEu tablets calcined at 800 °C under a UV lamp.

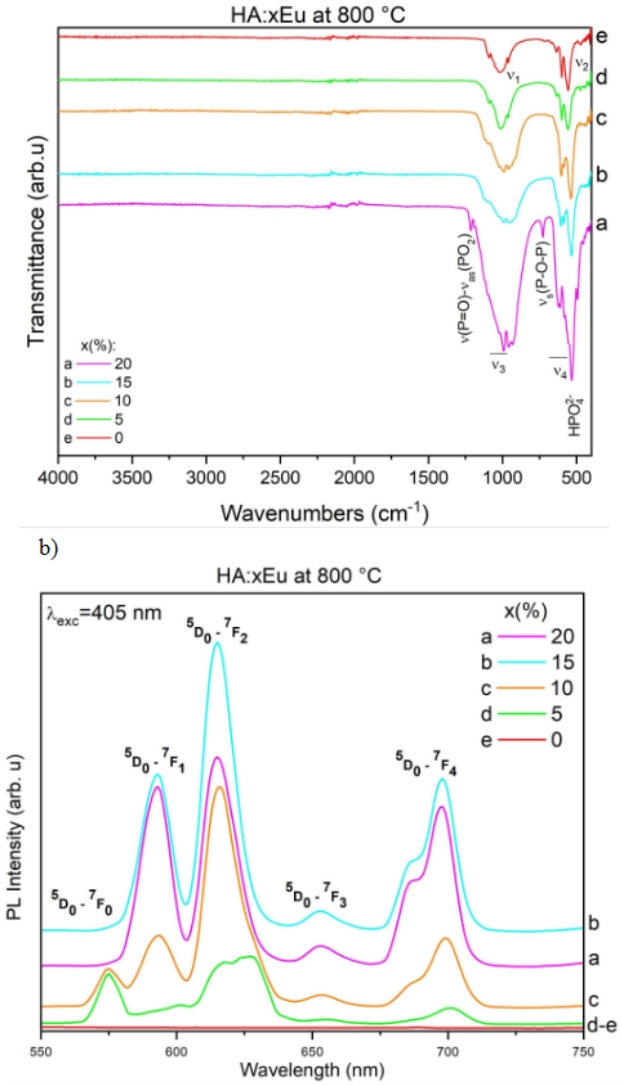

Figure 3. a) FTIR spectrum. b) Photoluminescence spectrum.

BIOPOLYMERS FROM Musa acuminata STEM FIBERS USED FOR SYNTHETIC POLYMERS MODIFICATION.

Rocha-Chauca Gabriela (1), Sallo-Chabla Nardy J. (2), María Terán (1), Líder Andrés Calle (3). Lucero-Borja D. (1)*.

(1) School of Biological Sciences and Engineering, University of Research of Experimental Technology Yachay,
Urcuquí - Imbabura 100115, Ecuador
(2) School of Physics and Nanotechnology, University of Research of Experimental Technology Yachay, Urcuquí -
Imbabura 100115, Ecuador.
(3) School of Chemistry and Engineering, University of Research of Experimental Technology Yachay, Urcuquí -
Imbabura 100115, Ecuador.

*Email: dlucero@yachaytech.edu.ec
Email:deysi.rocha@yachaytech.edu.ec

The rapid depletion of Earth's natural resources is a pressing concern for modern society. In the case of Ecuador, banana plantations produce approximately 2,200,760 tons of waste in just 2.5 months [1]. These significant amounts of waste pose a major environmental problem. Most banana byproducts are dumped as organic waste, further increasing environmental pressure. In addressing the environmental issues associated with banana waste management, it has been identified that banana stem fibers possess relevant characteristics for their use as composite materials [2]. In this regard, the present project aims to capitalize on this potential by producing a composite biopolymer. Additionally, the increasingly widespread use of plastic bottles has generated a concerning environmental problem. Although these bottles are recyclable, the volume of waste is significant. The report published by the United Nations Environment Programme (UNEP) in 2018, entitled "Single-Use Plastics: A Roadmap for Sustainability," mentions that by 2050 there will be more plastic in the ocean than fish by weight and that 80% of marine litter originates from land [3]. Therefore, it is necessary to find new applications that allow using different synthetic polymers, PET, HDPE, PVC, and recycled materials. In this context, the proposal is to reuse these materials in the production chain to create new materials for applications in fields such as 3D printing. A study was conducted on the residual biomass of banana plantations, specifically the stem, as the primary source of composite material. First, the fibers that make up the layers of the stem were manually extracted and dignified in a 12% NaOH solution at a temperature of 105°C for two hours. Then it was dried and subjected to a bleaching process with Ca $(O Cl)_2$ at 70%. Subsequently, it was ground in a ball mill, obtaining sizes of (38-45) um and (46-75) um. Additionally, dry fibers of equal sizes were ground for comparison of compaction. As for the synthetic polymers that will form the composite, the following grinding sizes were obtained: PET and PVC with a grinding size >75 um. On the other hand, the HDPE process is being optimized to achieve a grinding size similar to that of its study peers. In the current project, the properties of the biomaterial are being evaluated, and the microparticles of the synthetic polymers are being characterized to determine the best method of fusing the natural microfiber samples with and without treatment in conjunction with the different synthetic polymers mentioned. These composite materials are characterized using Thermogravimetric Analysis (TGA) and Differential Scanning Calorimetry (DSC) to identify the thermal properties of the different materials and their composites. In addition, the mechanical properties of the composites will be evaluated to determine their tensile strength, flexibility, Young's modulus, and rheological measurements. Currently, the individual characterization of samples is underway, as illustrated in the figures below. The subsequent step will be the characterization of the respective blends. The samples exhibiting superior thermal behavior will be employed for mechanical characterization. According to this study, the samples Demonstrate excellent thermal stability, and the microfibers begin to degrade at a temperature of 250°C. The examined polymers exhibit different

levels of thermal stability: PVC gradually varies up to 300°C, and its complete decomposition occurs at 700°C, while PET maintains its stability up to 380°C. The composites' melting temperature is projected to be within the range of 200-250°C. Previous research has been carried out using Musa paradisiaca and PET. In contrast, the present study employs fibers derived from Musa acuminatastems and polymers such as HDPE or PVC to create the proposed composites. As mentioned, the impact of the ground fibers' particle size on the recycled polymers' characteristics will be examined.

REFERENCES

[1] Padam, B. S. et.al. Journal of food science and technology (2014) (51) 3527-3545.
[2] Ramesh, M. (2018). Handbook of Properties of Textile and Technical Fibres, Elsevier Ltd, pp. 301–325.
[3] Mayta Rosas, A. M. (2021). Diagnosis of the impact of recycling of polyethylene terephthalate (PET) plastic bottles in
the district of Yanahuara.

ACKNOWLEDGMENTS

We thank the support of the laboratory technician at Yachay Tech's Laboratories from the School of Biological Sciences and Engineering and from School of Chemistry and Engineering.

FIGURES

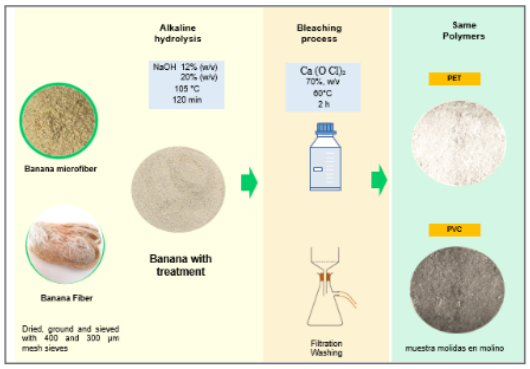

Figure. 1. Methodology

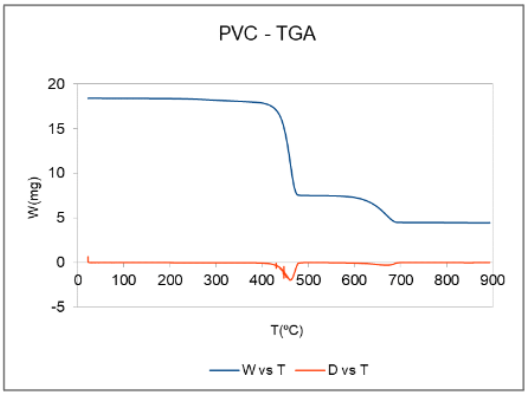

Figure. 2. TGA of the samples of TGA

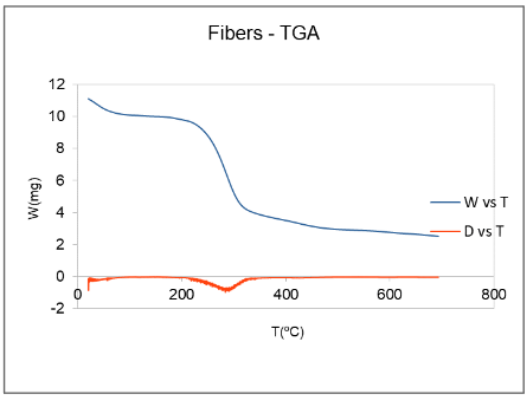

Figure. 3. TGA of the samples of natural fiber obtained without treatment.

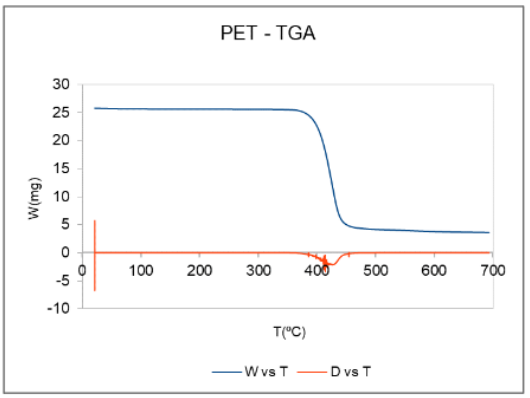

Figure. 4. TGA of the samples of PVC.

SOLID NANOPARTICLES STABILIZED EMULSIONS WITH BIOACTIVE COMPOUNDS FOR SUN PROTECTION

César Uriel Rodríguez Fuentes (1), Ana Guadalupe Castillo Olmos (2), Cynthia Cano Sarmiento (3)

(1, 2) Unidad de Investigación y Desarrollo en Alimentos, Tecnológico Nacional de México Campus Veracruz, Veracruz,
México. (3) CONACYT— Tecnológico Nacional de México Campus Veracruz, Unidad de Investigación y Desarrollo en
Alimentos, Veracruz, México.
Email: cesarrodriguef@hotmail.com

Exposure to UV radiation is a determinant factor in development of skin cancer, thus the use of sunscreen is essential for its prevention and the reduction of damage such as sun burns, photoaging and pigmentation. By their mechanisms of action, it exists two types of sunscreens: chemical barrier sunscreens, which are composed of molecules with the ability to absorb certain wavelengths, and physical barrier sunscreens, which reflect and/or disperse the incident light. Current formulations for sun protection are mostly composed of synthetic components associated to negative effects such as photo-irritation, photo-sensibilization and dermatitis. Therefore, is necessary to develop systems that increase protective properties, searching to decrease the amount of synthetic compounds and opting for those with similar characteristics from natural sources like olive, coconut, and green coffee oil. Within the range of products for sun protection we can find creams, aerosol sprays, lotions, gels and emulsions. The last ones being more commonly used because of their facility for incorporating components with photoprotective activity. Particularly, in emulsions exists a classification denominated Pickering, colloidal dispersions of two immiscible liquids that achieve stabilization by incorporating solid particles in the interfacial region, forming a shell around the droplet, providing higher rigidity, and lowering the contact surface, where the emulsification process regulates particle size, stability, and rheological behavior [1,2]. Solid particles serve with double purpose, as an emulsifier and physical barrier, which allows to reduce the use of synthetic compounds. However, they show the disadvantage of leaving a white cast when being applied. This can be solved decreasing the particle size to micro or nanometric scales. Moreover, bioflavonoids, such as quercetin, are chemical compounds present in low quantities in plants and food, that have been studied for their addition in sun protection systems, showing an increase in sun protection factor (SPF) and antioxidant activity, also having anti-inflammatory and anticarcinogenic properties, nevertheless, due to their easy degradation and low bioavailability, the usage of distribution systems are required to allow a higher exploitation of the components and their protection against degradation or oxidation effects [3]. Due to the impact of the emulsification process in the encapsulation of bioactive compounds, the aim of this study was to evaluate the effect of operating conditions in physicochemical properties of sunscreens composed of Pickering emulsions stabilized with zinc oxide nanoparticles loaded with quercetin. The systems were elaborated using rotor-stator homogenizer at 13,000 and 15,000 rpm for 2 and 4 min (Q1-Q4) with the following formulation: green coffee oil, zinc oxide thrietoxycaprililsilane (emulsifier) and a mixture of water, ethanol, and stabilizers. Emulsions loaded with 5 mg of quercetin per g of emulsion were analyzed by optical microscopy and digital image analysis software to determinate mean particle size and percentile D90 (Figure 2); Turbiscan stability index (TSI) was obtained and its rheological properties of flow and, creep and recovery. The lower particle size was achieved on Q2 and Q3 systems where size increase through time shown no significative statistic difference (Figure 1). Treatment Q3 showed lower increase of TSI value, which is associated to minimal destabilization (Figure 5). Regarding the rheological properties of treatments (Figure 3,4), they present variation according to mean particle size. In the creep and recovery curve, lower sizes are associated to minor deformations in structure and higher stability during skin dispersion, being resistant against rupture. Conditions for treatment Q3 (15,000 rpm and 2 min) provided the system with the lowest mean particle size and lower difference with D90 value, associated to more efficient encapsulations and a better zinc oxide nanoparticles distribution in the interfacial region, also presenting higher stability through time and against rupture phenomena in topical application, making it, the optimal conditions for the formulation of sunscreens stabilized by solid particles.

REFERENCES

[1] Guzmán, E. et al. Cosmetics (2022) (9) (68)
[2] Bordes, C. et al. Int. J. Cosmet. Sci. (2021) (43) (432)
[3] Hatahet, T. et al. Eur J Pharm Biopharm (2016) (108) (41)

ACKNOWLEDGEMENTS

Acknowledge to the Unidad de Investigación y Desarrollo en Alimentos (UNIDA) of the Tecnológico Nacional de México Campus Veracruz.

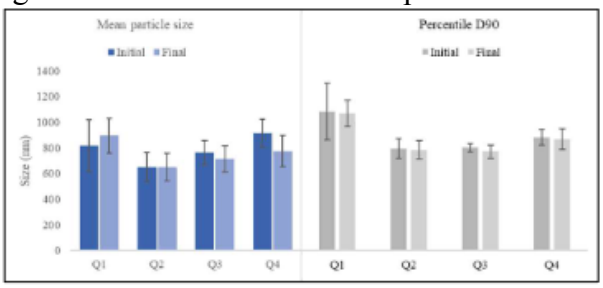

Figure 1. Mean particle size and percentile D90 of Pickering emulsions made by different treatments.

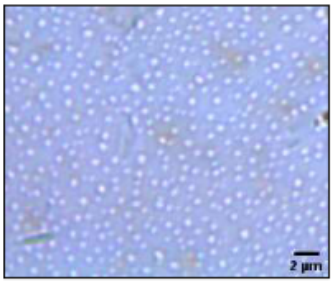

Figure 2. Micrograph of diluted sample for digital image software analysis of Pickering.

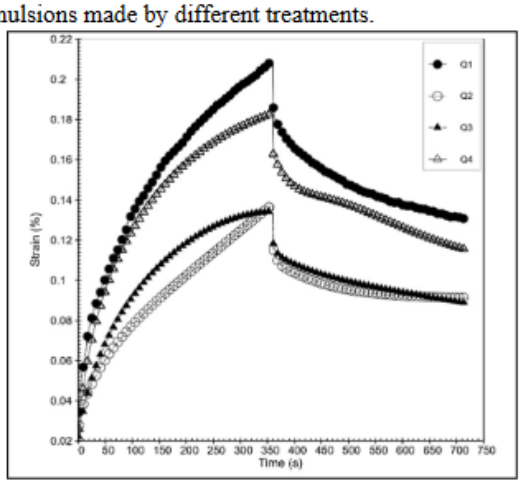

Figure 3. Creep and recovery curves of Pickering emulsions made by different treatments.

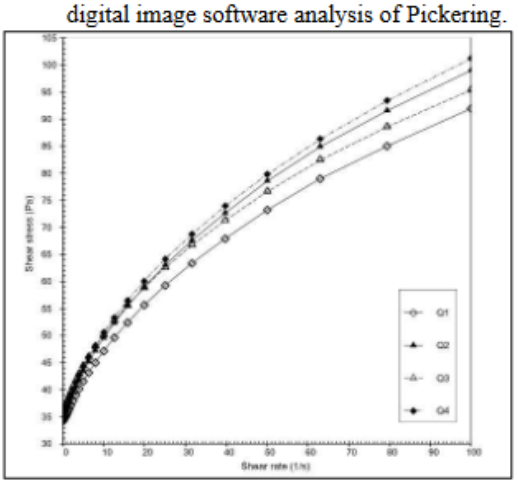

Figure 4. Flow curves of Pickering emulsions made by different treatments.

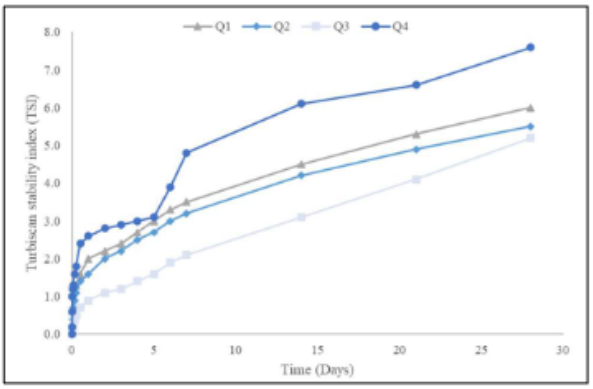

Figure 5. Turbiscan stability index (TSI) of Pickering emulsions through storage.

Acta Microscopica Vol. 32, Supp. 1, 2023
Abstract Book NSSY 2023- Galapagos 23 -29 April, 2023

DISCLOSING THE OPTICAL PROPERTIES OF SINGLE CHIRALITY SORTED SINGLE-WALLED CARBON NANOTUBES

Joselyn Benalcázar [1], Dido Denier van der Gon [1], Yohei Yomogida [2], Kazuhiro Yanagi [2], and Paola Ayala[1]

1 University of Vienna, Faculty of Physics, Boltzmanngasse 5, 1090 Vienna, Austria
2 Tokyo Metropolitan University, Department of Physics, Minami-Osawa 1-1, 1920397, Tokyo, Japan
joselyn.benalcazar@univie.ac.at

Understanding the optical properties of single-walled carbon nanotubes (SWCNTs) is of major interest to bring their applicability in optoelectronics, photonic and bioimaging to reality. From the theoretical point of view, several predictions have shown that the physical properties of SWCNTs depend on the geometrical configuration of the carbon atoms that construct their walls. This implies a definition for the chiral vector, chiral angle and consequently the chiral indexes (n,m). However, from the experimental point of view, observing those predicted properties imposes challenges that still embrace the production of the nanotube-material. For each specific chirality, defined and unique optical transitions are expected. These can be nicely identified with methods like optical absorption and Raman spectroscopy, and this has been done even in chirality mixed samples given that a reasonable debundling is achieved. Nevertheless, every foreign chirality in a batch represents an impurity. For that reason, it is extremely important to produce chirality sorted samples. For many years now, various methods have been developed. Among these, gel chromatography has been very successful to produce high yield and high purity samples at large scale quantities. This method is based on the selective adsorption of surfactants with different hydrophobicity on the nanotube´s surface at given adsorption sites, while leaving others free to stick in the gel for further gradient elution. Therefore, a careful load of surfactants and a controlled flow of the nanotubes through the gel are key parameters to explore how to increase the purity of single chirality sorting experiments. Chirality species are otherwise obtained after second purification processes in which most of them use surfactants to separate nanotubes by electronic character, diameter or chirality. In this work, we show a full optical characterization of single-chirality sorted SWCNTs processed by a modified gel chromatography process where the temperature dependence plays a crucial role. The preferential adsorption mechanism of the surfactants with different hydrophobicities onto the nanotubes' surface is shown. We focus on how their diameter and chirality can be correlated with a controlled-flow that involves a careful monitoring of the temperature.. The (10,0) zig-zag chirality will be used as an example of how a single chirality sample can be obtained in a 2 step process. Additionally, first results of high purity (11,0) chirality sorting are shown.